Theses and Dissertations

1-1-2013

Emulation of An Aeroderivative Twin-Shaft Gas Turbine Engine Using An AC Electric Motor Drive

Blanca A. Correa
University of South Carolina

Follow this and additional works at: https://scholarcommons.sc.edu/etd

Part of the Electrical and Electronics Commons

EMULATION OF AN AERODERIVATIVE TWIN-SHAFT GAS TURBINE ENGINE USING AN
AC ELECTRIC MOTOR DRIVE

by

Blanca Alicia Correa

Bachelor of Science
Universidad Pontificia Bolivariana, Colombia, 2006

Master of Science
Universidad de Antioquia, Colombia, 2008

_____

Submitted in Partial Fulfillment of the Requirements

For the Degree of Doctor of Philosophy in

Electrical Engineering

College of Engineering and Computing

University of South Carolina

2013

Accepted by:

Roger A. Dougal, Major Professor

Charles Brice, Committee Member

Herbert L. Ginn, Committee Member

Jamil Khan, Committee Member

Lacy Ford, Dean of the Graduate School

DEDICATION

In honor of my lovely Mom, Consuelo Montes,

To my dear husband, Michael Simcock,

&

To my dear Dad, Luis Fernando Correa, my brother, Luis Correa,

and granny, Aura Ramirez

ACKNOWLEDGEMENTS

Tim Chiocchio, your help during my time at CAPS was incredibly valuable. Thank you so much for your guidance. Special thanks also to Karl, Matt, James for collaborating with me. Thank you, Lukas and Passi, and all friends that I met at CAPS for your nice company during my stay.

My deepest gratitude goes to my Mom, Dr. Consuelo Montes. Her devotion for research and constant hard work were my inspiration to always carry on forward with my studies. She set the best role model for me as outstanding professor and researcher, and at the same time was always a loving, caring, supportive and sweet Mom. My work is the result of her immense love for me, and her desire for me to succeed and do well.

I am very thankful with my dear husband for his deep love and care, and offering me so much support and encouragement during my doctoral studies. Thanks dear Dad, for being always so loving and supporting, and always giving me motivation to succeed. Thanks dear brother and granny, for your sweetness, love and support. Special thanks to all family and friends.

ABSTRACT

This dissertation presents a method to use an electric motor to emulate the steady-state and transient shaft power characteristics of an aeroderivative twin-shaft turbine engine. Model-based control provides the framework for developing an aeroderivative twin-shaft engine emulation system. Criteria are developed to appropriately specify the motor and variable-speed drive, based on torque, power, and inertia. This method accounts for the difference in inertia between the engine and the emulating motor; it establishes for the first time the nominal and peak torque requirements of the machine and the peak power and current requirements of the electronic motor drive (inverter).

Our results show that the required peak torque and power, and maximum inverter drive line current increases as the ratio between motor and engine inertia constant is larger. For instance, when the inertia ratio between the motor and engine is 100, the motor requires a power rating up to 3.25 times that of the engine in order to match speed accelerations that are likely to happen during small transient loading conditions.

Several other considerations are key to successful emulation of turbine engines, such as stability and inertia coupling. Our work defines the stability of the emulation system in terms of the transfer function associated with the torque load low-pass filter, motor drive speed control, and motor and load machine shaft dynamics in relation to the engine inertia constant. When the inertia of the motor is much larger than the engine it is emulating, the system can become unstable if the bandwidth of the torque load low-pass

filter is much larger than the bandwidth of the engine. We also show that the speed tracking accuracy can be as good as 1% at accelerations typical of low amplitude transient loading and unloading conditions. But inertia coupling considerations have a significant effect on the transient speed response of the engine and the ability of the emulation system to track the performance of the engine. A model-based analysis of the engine emulation system reveals that when the inertia of the motor is much larger than the engine, the speed response of the open-loop system is faster than the closed-loop system (emulation mode) because the engine can accelerate at a faster rate since the generator shaft torque is not coupled to the inertia of the engine. However, in emulation mode the generator shaft torque is coupled to the speed of the engine and this causes the speed response of the engine to accelerate at a slower rate.

The main challenge of this study deals with the fact that unlike other prime movers, such as wind turbines or diesel engines, aeroderivative engines have a high power density compared to a motor of the same power rating. Therefore, when emulating an aeroderivative engine using an AC electric motor drive, torque and current limitations, as well as accuracy and stability issues can arise as a consequence of the larger motor inertia.

We have developed a design procedure to facilitate the development of an aeroderivative engine emulation system. In the first stage an appropriate AC electric motor and variable-speed drive are identified. In the second stage, a stability and inertia coupling analysis defines the testing conditions and limits. Our results have been verified at reduced scale by using a low power hardware-in-the-loop experiment.

TABLE OF CONTENTS

LIST OF TABLES

LIST OF FIGURES

LIST OF ABBREVIATIONS

AC .... Alternating Current

A/D .... Analog to Digital

ADC .... Analog-to-Digital Converter

CHIL .... ControllerHardware-in-the-Loop

D/A .... Digital to Analog

DC .... Direct Current

DQ .... Direct-Quadrature

FT .... Free Turbine

HFAC .... High-Frequency AC

HIL .... Hardware-in-the-Loop

IPS .... Integrated Power System

MVDC .... Medium-Voltage DC

NGIPS .... Next Generation Integrated Power System

PHIL .... Power Hardware-in-the-Loop

PI .... Proportional-Integral

PID .... Proportional-Integral-Derivative

PWM .... Pulse Width Modulation

RMS .... Root Mean Square

CHAPTER 1: INTRODUCTION

1.1 Contributions of Dissertation

The main contributions presented in this dissertation are listed as follows:

1. Definition of a method to use an electric motor to emulate the steady-state and transient shaft power characteristics of an aeroderivative twin-shaft turbine engine.

   - A model-based control provides the framework for developing an aeroderivative twin-shaft engine emulation system.

2. Development of criteria to appropriately specify the motor and drive, based on torque, power, and inertia:

   - The method accounts for the difference in inertia between the engine and the emulating motor.

   - The method establishes for the first time the nominal and peak torque requirements of the machine, and the peak power and current requirements of the electronic motor drive (inverter).

3. Development of a model-based analysis of an engine emulation system that enables the examination of system stability and the effect of inertia coupling.

4. Definition of a design procedure to facilitate the development of an aeroderivative engine emulation system:

   - In the first stage, an appropriate AC electric motor and variable-speed drive are identified.

- In the second stage, a stability and inertia coupling analysis defines the testing conditions and limits.

It is important to clarify that the aeroderivative twin-shaft gas turbine engine models used in this study restrict the emulation system to evaluate only certain operating conditions. In this work, the engine models are only suitable for transient power system analysis, and allow operation above and below nominal speed. These engine models are not suitable for analyzing large transient conditions or engine surge.

1.2 Motivation

When testing an experimental machine such as a new generator it may be necessary to substitute a surrogate power source for a prime mover that is not yet available. For instance, one could test a new generator by spinning it with an electric motor drive system instead of with a gas turbine engine. This can be useful when it is of interest to study how the generator will function when connected to a prime mover over a subset of operating conditions such as steady-state operation, transient loading and unloading, short-circuit and open-circuit faults, and stall characteristics. The focus of this dissertation is to develop an engine emulation system capable of emulating the steady-state and dynamic loading and unloading behavior of an aeroderivative gas turbine engine.

The increase use of turbogenerators using aeroderivative engines can benefit from an engine emulation system because it can provide an in-door test platform for generators. This allows system analysis in a more immediate, robust and safe manner, and testing without risk of damaging an expensive engine.

An engine emulation system can be particularly useful for the development of future power generation technologies as described by the Next Generation Integrated Power (NGIPS)

master plan [1]. In order to meet the power-dense requirements of future ship designs, the Navy is evolving its current medium voltage, 60 Hz Integrated Power System (IPS) by the definition of the NGIPS master plan. Figure 1.1 shows the NGIPS roadmap which includes a plan for the development high-frequency AC (HFAC) and medium voltage DC (MVDC) technologies.
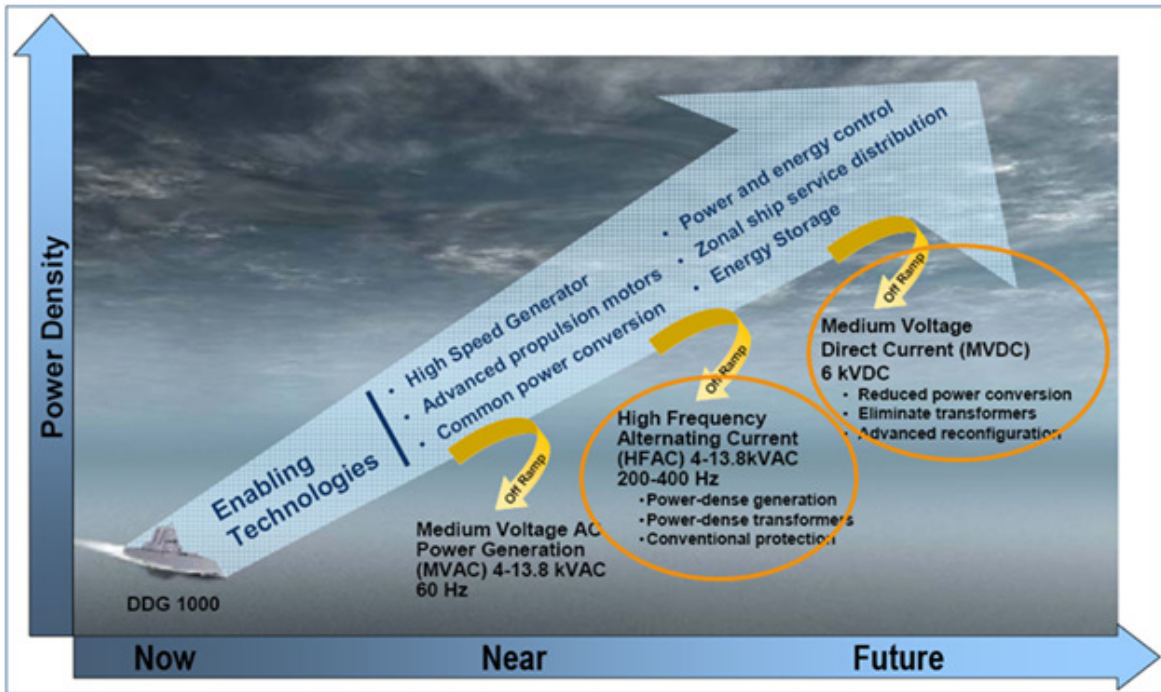
Figure 1.1: NGIPS master plan

HFAC refers to power distribution systems that deliver power at fixed frequencies greater than 60 Hz, but below 400 Hz, and it is proposed as an interim solution until MVDC is developed. The benefits of operating at high speed include avoiding gearing between the turbine and generator parts and high power density. MVDC consists of a power distribution of medium voltage DC power in the range of ±3,000 VDC to ±10,000 VDC. The main benefit of both HFAC and MVDC is the availability of higher power density power generation systems. The

NGIPS master plan emphasizes the need for HFAC power generation modules at three power levels [2]:

- Low power level (2–5 MW) using a fuel-efficient diesel as prime mover

- Medium power level (10–15 MW) using a gas turbine engine as prime mover

- Main propulsion power level (20–40 MW) using a gas turbine engine as prime mover

The current challenges in the implementation of HFAC turbogenerator systems at the mega-watt power level motivate the need for developing an aeroderivative twin-shaft gas turbine engine emulation system, so that the generator part of a HFAC turbogenerator system can be tested even before the engine part of the system is actually built. Reference [1] describes several challenges regarding the implementation of HFAC systems operating at the mega-watt power level. Some of these are:

- Limited higher frequency power test capabilities and infrastructure: Normally, manufacturers only have test equipment or facilities that operate at 60 Hz. Therefore, at HFAC there is a need to build dedicated test facilities or make test equipment available to manufacturers. There is also need to develop methods for testing equipment without using power sources at the design frequency.

- Lack of design standards and practices: The NGIPS roadmap emphasizes the need for design infrastructure to successfully integrate HFAC systems into the ship design process.

- Determination of the appropriate prime mover to spin a high-speed generator: One main concern when operating at HFAC at mega-watt power levels is interfacing high-speed generators that require a high number of poles with prime movers that are slower, or interfacing high-speed engines with round rotor synchronous generators.

- High ground fault currents: At HFAC the ground fault current can be higher than in a conventional 60 Hz system.

- Paralleling of generators: When operating at high frequencies the window of time that a generator breaker can close to parallel a generator reduces and the ability of existing breakers to operate at a reduced time window is unknown.

1.3 Challenges

In studies reported on electric motor drives that are used to emulate a reciprocating piston engine or a wind turbine [3]–[13] the surrogate prime mover has low inertia compared to the intended prime mover, and the surrogate is capable of accurately emulating the torque and speed characteristics of the planned prime mover. However, aeroderivative engines are characterized by having a very high power-to-inertia ratio – much higher than that of available electric motors. This means that the electric motor emulating an aeroderivative engine will have a larger inertia compared to the engine, especially at the mega-watt power level. As an example, reference [14] includes information on gas and power turbine inertia of the AGT1500 Honeywell twin-shaft engine. The power-to-inertia ratio of this engine is very high, since its operating power is 1,120 kW and the power and gas turbine inertia are 0.141 kg·m^2 and 0.074 kg·m^2, respectively. In Table 1.1, the specifications of this engine are compared to the specifications of an AC motor with a similar power rating (1.5 MW) [15]. The inertia of this motor is 80 kg·m^2, which is considerably larger than the inertia of the AGT1500 power turbine.

The very low inertia of an aeroderivative engine relative to a motor of the same power rating poses a major challenge in the emulation system, since the emulating motor will likely require a large torque demand in order to track the speed performance of the engine during acceleration and deceleration phases. Therefore, when emulating an aeroderivative engine by

5

using an AC electric motor drive, power and accuracy limitations, as well as stability issues are expected to arise.

An additional challenge in developing an aeroderivative twin-shaft engine emulation system has to do with the reference engine model. The accuracy of the engine model determines the types of steady-state and dynamic tests that can be evaluated in the engine emulation system. When implementing the engine emulation system in a HIL experimental setup a representation of the engine model that runs in real-time is necessary. Therefore, there can be a trade-off in achieving high computational speed and high accuracy when using the real-time engine model.

Table 1.1 Comparison of inertia between a twin-shaft engine and an induction motor with similar power rating

Prime Mover	Rated Power (MW)	Inertia (kg·m^2)
Honeywell AGT 1500 twin-shaft engine [14]	1.12	0.141 (power turbine rotor) 0.074 (gas turbine rotor)
Squirrel-cage induction motor [15]	1.5	80

1.4 Literature Review

1.4.1 Test-Bed Development

The development of technologies such as turbogenerators, combustion engines for the automotive industry and wind turbines, can usually require approaching the boundaries of technical feasibility. In this context, test-stands present a means for testing system components in a laboratory environment providing safety, flexibility, robustness and decrease in costs.

In the automotive industry, the use of test rigs for the design of the engine and its electronic control unit is a commonly accepted practice [16], [17]. The idea is to simulate the dynamics of the car body and apply the simulated engine load to the engine using an electric

motor dynamometer. There is vast literature on this topic and some studies focus on improving the dynamical torque control performance of the dynamometer [16], model based inertia compensation [17], and power measurement and loading control [18].

In industrial processes, there is also need to test electrical motor drives that are connected to mechanical loads, which can present a nonlinear behavior. This can be achieved by using a dynamometer used as a programmable load emulator [19].

In these previous applications, test stands are used to test the actual engine or motor drive for different types of loading conditions. Therefore, in the context of a prime mover load system the actual prime mover is tested using an experimental load. The focus of this dissertation deals with testing the actual load part of a prime mover load system. Particularly, the load part is a generator and the prime mover is an emulated aeroderivative twin-shaft gas turbine engine.

The development of a gas turbine engine emulation system has been previously reported in [20]. In this study, a two-spool engine emulation system is used for studying the start-up sequence of an uninhabited autonomous vehicle (UAV) system that is powered by a two-spool gas engine with embedded electrical generators on both spools. Two vector controlled variable-speed drives are used to emulate the engine spools and a real-time platform simulator that contains the model of the engine outputs the speed commands to the spool motor drives. However, this study suggests the need for a more accurate engine model and details of the engine emulation system are not fully described. Additionally, the purpose of this study is for power levels of the order of 100 kW and not the mega-watt power level, which is of interest in this dissertation.

Alternatively, the approach of using an electric motor drive system to emulate a combustion engine or a wind turbine has been realized in the past. In the case of wind turbine

7

emulation, studies have been conducted in order to improve testing and evaluation of technologies for wind energy conversion systems without costly construction of the actual wind turbine blades [3]–[12]. In most of the studies, the main focus is to feed the power-speed characteristic of a wind turbine to the motor drive controller and emulate steady-state and dynamic characteristics. Some approaches also include methods for compensating the dynamic effects in wind turbines such as large inertia [5], [10] and torque oscillations caused by wind shear, tower shadow and variable wind speed [11].

In the case of combustion engine emulation, reference [13] describes a dynamometer test stand for an automotive application in which a gasoline/diesel engine power source is emulated by an electric motor in order to test drive-shaft components such as transmissions and/or differentials. Normally, the process of testing transmissions can involve using multiple engines, so the use of a dynamometer test stand eliminates the need to perform a mechanical change of the engine when a different one is required. The gasoline/diesel engine power source emulator is designed so that the drive train under test experiences the same shaft torque dynamics that it encounters using an actual engine.

It can be concluded from these studies that there are three important aspects when emulating a prime mover: the reference prime mover model, the emulating motor inertia relative to that of the prime mover, and the electric motor drive controls. The following subsections provide more insight into these three aspects.

1.4.2 Prime Mover Reference Model

Table 1.2 shows as summary of the reference models used in the different prime mover emulation studies. Most of these studies use simplified models in order to run the prime mover models in real-time simulation. Since this dissertation concerns the emulation of twin-shaft engines, Subsection 1.4.2.1 presents a literature review on twin-shaft engine models.

Table 1.2 Reference models used in different prime mover emulation studies

Type of prime mover emulator	Reference model
Gas turbine engine emulator [20]	The reference speeds for the drive controllers are programmed to follow pre-determined speed profiles (authors express the need for a more accurate gas turbine engine model as future work).
Wind turbine emulator [5]	• Represented by the wind turbine power-speed characteristic. • Input wind speed data in the form of a lookup table is fed into a Wind Speed Pattern Generator to obtain a realistic wind speed signal.
Combustion engine emulator [13]	• The torque reference is a function of the speed of the engine and a reference accelerator pedal position. • The engine model computes the fuel rate for a given speed and pedal position. • The fuel rate algorithm is limited by a look-up table that computes maximum fuel-rate for a given speed.

1.4.2.1 Twin-Shaft Gas Turbine Engine Simulation Models

Several aeroderivative twin-shaft engine simulation models available in the research literature focus on steady-state and transient loading and unloading operation. This is the case in references [21]–[23], which present the design and validation of dynamic twin-shaft engine models. Reference [21] presents the design of single and twin-shaft engine models using modular code based on an object-oriented approach. Results include simulation tests of the transients after load rejection for a twin-shaft aeroderivative industrial engine connected to a varying load. First, starting from the design point condition, a load rejection of 50 % at full-load is simulated. Then, a load rising ramp is applied bringing back the power to full load. Reference [22] presents a simplified mathematical model of a twin-shaft engine, which is claimed to be suitable for use in dynamic studies for both electric power generation plants and variable speed mechanical drive

applications. The mathematical model consists of a set of slightly nonlinear algebraic equations and simplified transfer functions in the Laplace domain linking the main system variables. Simulation is used to evaluate the performance of the twin-shaft engine model powering a water-jet propulsion system. Results show the performance of the engine model during acceleration and deceleration phases following changes in the fuel flow. Reference [23] presents the design of a twin-shaft engine model based on thermodynamic relationships, which is validated against manufacturer factory test data. The engine model is incorporated in a single machine infinite bus system. The large disturbance behavior of the engine is validated using a self-clearing 80 ms three-phase fault at bus and the small disturbance behavior is validated by a 2.5 % decrease in the reference voltage of the generator.

Two different twin-shaft turbine engine models are used in this dissertation. Engine Model 1 refers to a physics-based engine model implemented in the Virtual Test Bed (VTB) software [24]. This model is described in [25] and it consists of a dynamic non-linear system model of a simple-cycle, two-shaft engine with intercooler based on mechanical and thermodynamic equations. Physical parameters that describe the thermodynamic behavior of an engine such as mass flow, heat ratio, and temperature are included. A speed controller modulates the fuel input so as to maintain the rotational speed constant under varying loads. Engine Model 1 is validated against another engine model available in the GasTurb [26] software. The operating range of this engine simulation model is between 10-14 MW and 700-900 rad/s. Therefore, the model is capable of steady-state and transient loading and unloading operation within these ranges. However, is not suitable for running in a real-time simulation environment, which is a requirement for the development of a HIL simulation of the engine emulation system. A common solution for the implementation of models in real-time, is the use of simplified

models that are based on signal-flow representations or transfer functions. Therefore, Engine Model 2, which is based on a signal-flow representation of a twin-shaft engine, is used in Chapters 5 and 6 for the development of HIL simulations of an engine emulation system. The speed range of Engine Model 2 is 0.95 p.u.-1.07 p.u. Therefore, steady-state and transient loading and unloading tests can be performed within this range of operation.

1.4.3 Effect of the Emulating Motor Inertia

This dissertation, concerns the difficulty in emulating a high-power density prime mover such as an aeroderivative engine by using an AC electric motor drive. As previously mentioned, some studies on wind turbine simulators include the effects of large wind turbine inertia. For instance, a 3 MW wind turbine has an inertia of the order of $12.6 \cdot 10^6$ kg·m^2 [27]. Therefore, the power-to-inertia ratio of a wind turbine is very low. A motor that can emulate the performance of a wind turbine can be found for the same output power range with a much lower inertia. For instance, in the low-power wind turbine emulator setup presented in [12], the power and inertia of the reference wind turbine is 2.5 kW and 7 kg·m^2, respectively, while the power and inertia of the DC emulating motor is 3 kW and 0.25 kg·m^2, respectively. Moreover, in the case of the gasoline/diesel engine dynamometer test stand presented by [13] the control algorithm has proven to be successful for a maximum ratio of electric motor inertia to emulated engine inertia of 10:1.

Reference [9] reports the development of a wind turbine simulator, which analyzes the the case of having a real turbine-generator system with smaller inertia than the wind turbine simulator. In order to include the effect of smaller inertia of the actual turbine, the configuration of the wind turbine simulator is designed to allow bi-directional power flow. Therefore, the wind turbine simulator consists of a DC motor supplied by a four quadrant chopper that is connected

to the DC link fed by a three-phase PWM rectifier. Two important conclusions are derived from this study:

1. The power capacity of the wind turbine simulator should be larger than that of the actual turbine system when the actual turbine system has smaller inertia than that of the wind turbine simulator.

2. In order to force a system with large inertia to behave the same as a system with smaller inertia, larger torque needs to be produced for the inertia compensation. This study tackles this issue by choosing a lower mean value of speed in case the required torque exceeds the capacity of the wind turbine simulator.

1.4.4 Emulating Motor Drive Controls

There are two main control modes in the emulation research literature: torque or speed control modes. In reference [19], the principle of inverse mechanical dynamics is referred to as the approach of using the measured motor shaft speed to derive the desired torque for the emulating motor. For instance, Figure 1.2 shows the block diagram of the wind turbine simulator described in [9], which uses the principle of inverse mechanical dynamics. It can be seen that the DC emulating motor position, θ, is measured to derive the speed, ω, and acceleration, $d\omega/dt$, of the shaft by using a rotor speed and acceleration observer. Then, a generator torque estimator is used to derive the generator torque, T_{Gen}. The turbine model uses T_{Gen}, and ω, to derive the motor torque, T_M, which is used as tracking variable in a current controller loop.
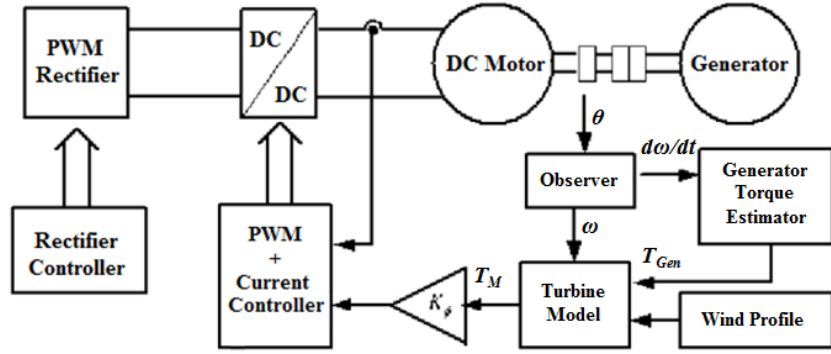
Figure 1.2: Emulation scheme in [15]

However, reference [19] concludes that discretization effects can severely affect the performance of emulation schemes based on the principle of inverse mechanical dynamics. In order to avoid inverse dynamics, [19] uses the shaft speed as tracking variable for the implementation of a dynamic load emulator. The open loop sampled data system of the proposed emulation method of [19] is presented in Figure 1.3. In this diagram, $G(s)$ is the transfer function describing the motor and load machine rotor dynamics, and $G_{em}(z)$ is the emulated load transfer function. The desired shaft speed, $\omega_{em}(z)$, is computed based on the motor drive torque, $T_e(z)$.
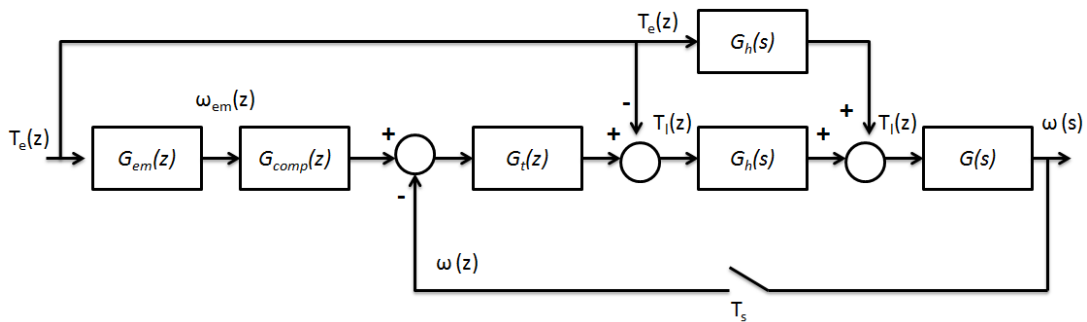
Figure 1.3: Emulation scheme in [19]

In this dissertation, the method for emulating an aeroderivative engine by using an AC motor drive is based on a speed control approach. Therefore, the performance of the engine is

13

emulated by dynamically setting the speed reference of a vector controlled AC motor drive according to the performance predicted by a model of the engine.

1.5 Outline

This dissertation is organized as follows. Chapters 2 and 3 introduce basic background on gas turbine engines and electric motor drives, respectively. Chapter 4 presents the development of an aeroderivative engine emulation system for testing a HFAC generator in simulation. Chapter 5 describes the development of a benchtop-scale HIL engine emulation system. Chapter 6 presents the development of an engine emulation system at a low power level that is used to validate methods described in Chapters 7 and 8. Chapter 7 describes a method for selecting an appropriate AC electric motor and variable-speed drive for emulating an aeroderivative engine based on torque and power criteria. Chapter 8 presents a model-based analysis of the engine emulation system that allows predicting the stability and inertia loading effects of the system. Chapter 9 presents conclusions, recommendations and future work.

CHAPTER 2: BACKGROUND ON GAS TURBINE ENGINES

This chapter presents basic background on gas turbine engines for electric power generation. The two main engine configurations, single and twin shaft, are presented followed by a description of the working principles of the twin-shaft engine. Finally, the main control loops included in typical gas turbine engine models for power generation studies are described.

2.1 Gas Turbine Engines for Electric Power Generation

Turbogenerators have been in use for more than 100 years for steam and gas turbine engine applications of any size. The invention of the cylindrical rotor for a high-speed generator back in 1901 by Charles Brown has allowed the turbogenerator to be used for converting steam and gas turbine engine power into electrical power [28]. In the 1970s, gas turbine engines for electric power generation were primarily used for peaking and emergency applications. Currently, the use of gas turbine engines for electric power generation also includes provision of baseload power for off-shore platforms, large combined cycle plants for thermal power generation, cogeneration plants and marine applications [29].

The gas turbine engine is an extremely versatile prime mover and can be used in a wide variety of applications other than electric power generation such as in mechanical drive systems and jet propulsion. However, the scope of this dissertation is on the use of gas turbine engines, particularly aeroderivative twin-shaft engines, as prime movers for turbogenerator systems.

2.2 Types of Gas Turbine Engines

Two common configurations of gas turbine engines are the single- and the twin-shaft types as shown in Figures 2.1 and 2.2. The main difference between these two configurations is the linkage of the gas generator turbine to the power turbine. In the single-shaft engine, the gas generator turbine runs at the same speed as the power turbine and output shaft, whereas in the twin-shaft engine the gas generator turbine and the power turbine (also known as free turbine in this configuration) can operate at different speeds since they are physically separated. In this case, the gas generator turbine and power turbine are coupled thermodynamically by the hot gas flow. In the single-shaft engine, the compressor and turbine are connected on a single shaft, which generally makes the overall inertia of this type of engine larger than the two-shaft engine [30].

Single-shaft engines can be of heavy-duty type operating between 10 to 100 MW or they can also operate at low powers, such as in the case of a small turbo jet engine. Heavy-duty engines can be single-, twin- or even triple-shaft.

Twin-shaft engines can be of aeroderivative or frame type. For land power generation, most heavy-duty engines are of frame-type. Heavy frame engines are characterized by lower compression ratios (typically below 15) and tend to be physically large, whereas aeroderivative engines operate at very high compression ratios (typically in excess of 30) and are characterized by being compact and having a high power-to-weight ratio. Aeroderivative engines are derived from jet engines with the exhaust expanded through a free turbine rather than the original exhaust nozzle so that they can drive a rotating load such as a generator [29]. These engines are widely used for simple-cycle power generation, cyclic applications such as peaking power, and

they are also ideal for emergency power applications of any sort because their start times are very fast [31].
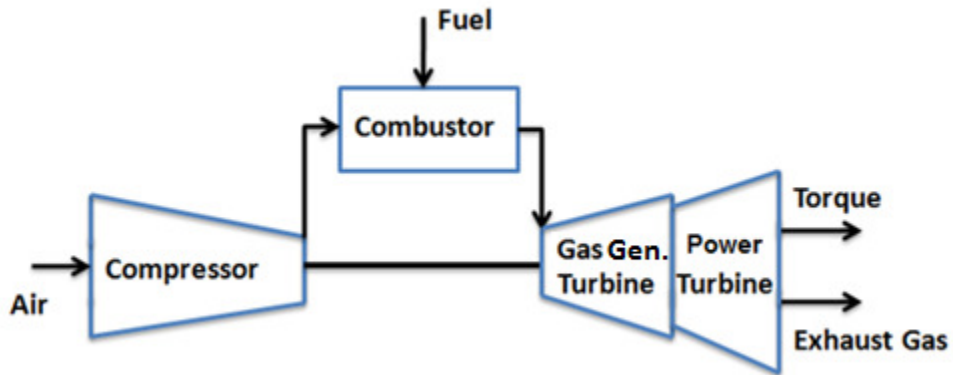
Figure 2.1: Schematic of a single-shaft engine
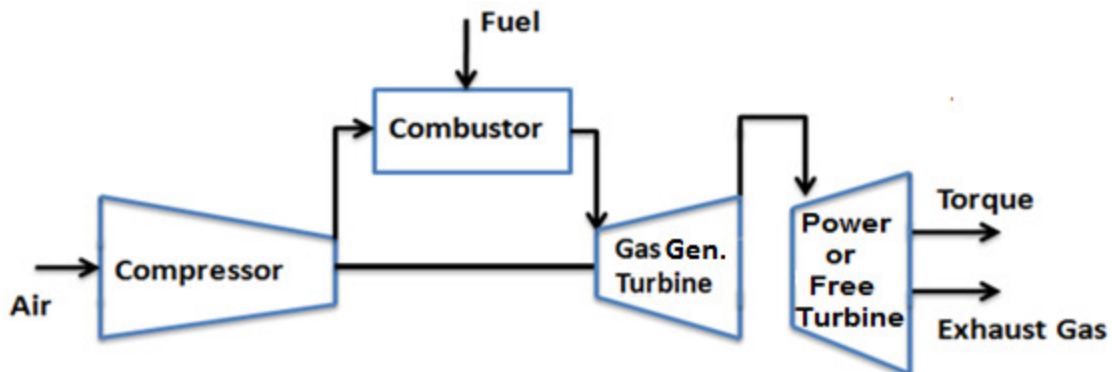
Figure 2.2: Schematic of a twin-shaft engine

2.3 Working Principles of the Twin-Shaft Gas Turbine Engine

Gas turbine engines operate under the Brayton thermodynamic cycle. The classical temperature versus entropy (T-S) diagram of this cycle is shown in Figure 2.3. Four main processes take place in a twin-shaft engine as shown in Figure 2.3: 1. (Process 1-2) Air entering the compressor is compressed to some higher pressure, 2. (Process 2-3) Air enters the combustion system, where fuel is injected and combustion occurs, 3. (Process 3-4) High pressure

and temperature gases expand in the gas generator turbine creating torque to drive the compressor and gases exhausted from the gas generator turbine further expand in the free turbine creating the mechanical torque to drive a generator, 4. (Process 4-1) Hot gases are exhausted to the atmosphere in the exhaust section.

In a turbine engine, the relationship between the mass flow through the compressor and the pressure ratio across the compressor is represented in a compressor map, as shown in Figure 2.4. The separate parallel lines in Figure 2.4 represent the compressor behavior at various constant speeds. The lines of constant adiabatic efficiency are also plotted on the compressor map. The surge line indicates where the operation of the compressor becomes unstable and it joins the different speed lines. Surge occurs when the main flow through the compressor reverses its direction and flows from the exit to the inlet during short time intervals. If this effect is allowed to persist it can irreparably damage an engine. The operating line of the compressor is also indicated in Figure 2.4 [32].

The relationship between turbine shaft power and gas flow is represented in a turbine performance map as shown in Figure 2.5. This performance map includes turbine inlet temperature and pressure lines, which are two variables that fluctuate most in a turbine. The power of a turbine depends on the efficiency of the turbine unit, the flow rate and the turbine inlet temperature [32].
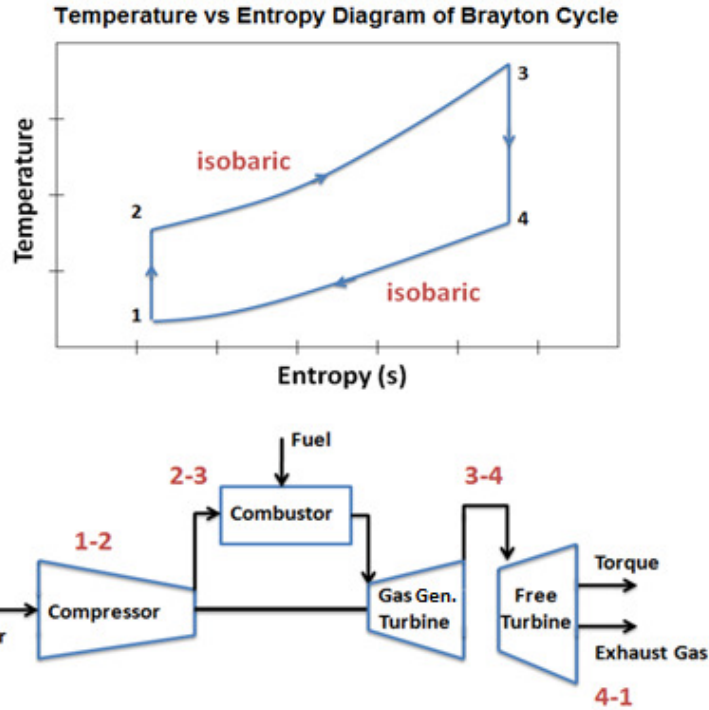
Figure 2.3: Twin-shaft engine processes
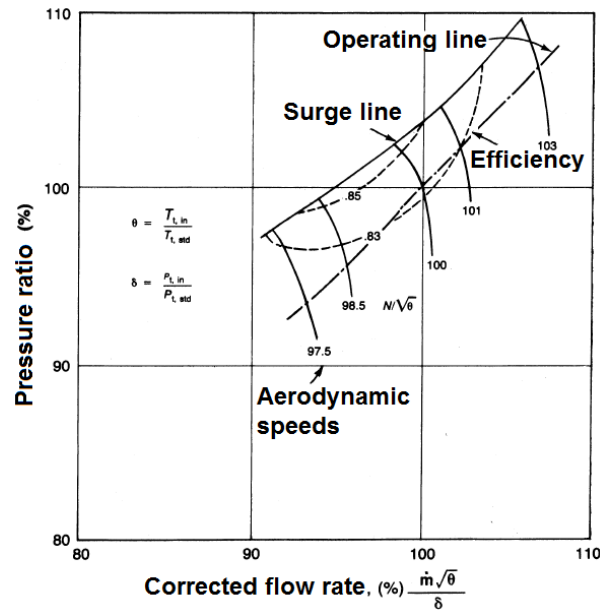
Figure 2.4: Compressor performance map
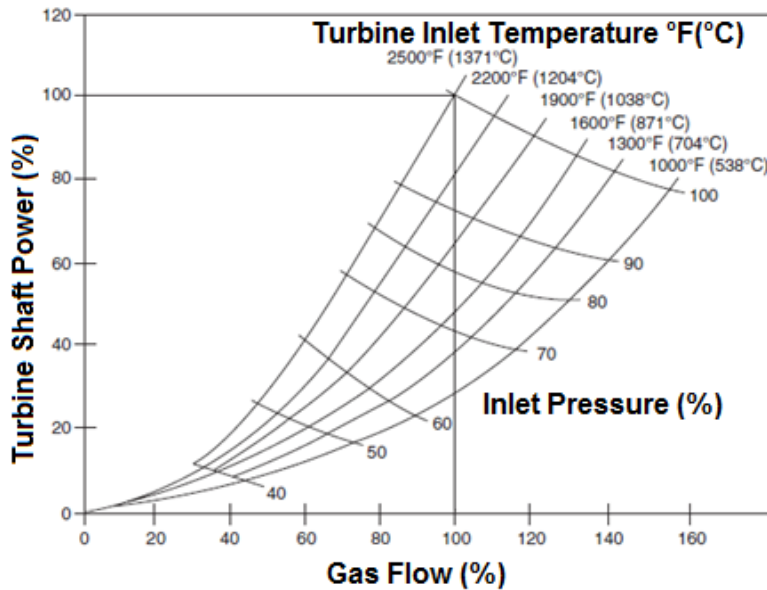
Figure 2.5: Turbine performance map

2.4 Gas Turbine Engine Controls

Typical models of gas turbine engines for power system stability studies usually include three control loops:

• Speed or governor control

• Temperature control

• Acceleration control

During normal operating conditions the speed control loop is the main control loop dictating the response of the engine. If either the temperature or acceleration controller reaches its set point the appropriate limit controller overrides the speed controller to protect the engine from high temperatures or overspeed. Therefore, in an engine these different controllers are always in operation but the output signal to the fuel system is only determined by the controller output signal that requires the minimum fuel flow. The different control signals are fed to a low

20

value selector. The fuel system controls the mechanical power delivered by the engine [33]. The three main control loops are further described as follows:

- **Speed control:** The speed control loop is the main control loop during normal operating conditions and can be based on a conventional PID controller. The input to this control is the speed deviation. In the case of a twin-shaft engine, [34] presents an engine model that includes two speed signals going into the low value selector instead of a single one as in the case of a single shaft engine. One of the speed signals is the output of the gas generator turbine speed controller and the other one is the output of the free turbine speed controller [33].

- **Temperature control**: Due to the action of the speed controller, when the engine load demand increases under normal operating conditions the output power of the engine increases. The increase in power causes the exhaust temperature to rise. If this temperature reaches a maximum temperature limit, the temperature controller overrides the speed controller in order to reduce the output power of the engine so that the exhaust temperature remains within the appropriate limits [33].

- **Acceleration control:** The acceleration control reduces the fuel flow in order to reduce the output power of the engine which in turn limits the acceleration. The acceleration control uses the engine speed as input signal and computes the engine acceleration using a differential block. The acceleration is compared to an acceleration limit to obtain an error signal and provide an appropriate control action that is fed to the low value selector [33].

    The acceleration loop comes into play when the generator experiences high positive acceleration. This condition can occur during startup and load rejection processes. The acceleration control facilitates loading the engine as quickly as possible by opening the fuel

valve and initiating loading. When loading approaches its target set point the speed control starts to override the acceleration controller and the fuel valve approaches its final running position. During this process the temperature is monitored by the temperature controller to avoid exceeding the appropriate operating levels [35].

CHAPTER 3: BACKGROUND ON ELECTRIC MOTOR DRIVES

This chapter presents basic background on AC electric motor drives. Initially, the general concept of electric motor drives is explained followed by a brief review of different control schemes. Next, vector control schemes for synchronous and induction motor drives are explained. Finally, the concept of hardware-in-the-loop simulations is presented.

3.1 Electric Motor Drives

A variable speed drive is composed of a power electronic converter, a motor, a control algorithm and sensors for signal acquisition. Nowadays, the majority of variable-speed drive applications use AC drives since AC motors are simple, less expensive, and have more robust structures [36] than DC motors. In general, AC motors are classified as either induction or synchronous motors.
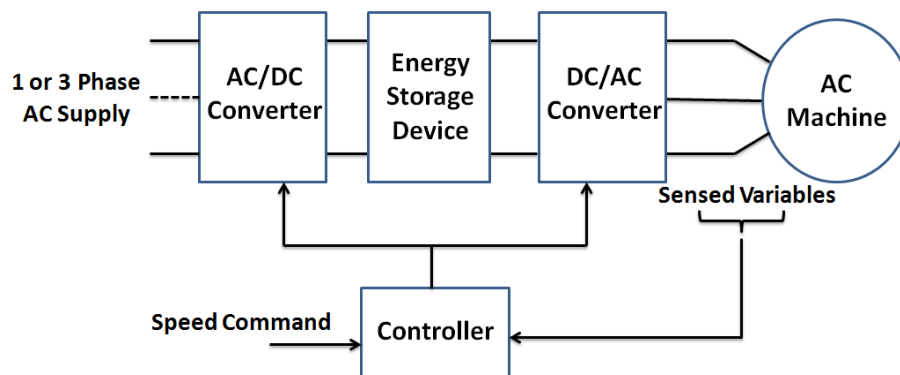
Figure 3.1: Schematic of an AC motor drive [37]

Figure 3.1 shows the basic layout of an AC drive using a converter with a DC link [37]. The first AC/DC converter stage converts voltages and currents to DC quantities and then the second DC/AC converter stage converts these quantities to AC voltages and currents of variable frequency.

3.1.1 Three-Phase Inverter

The process of converting DC to AC power is called inversion [37]. The input to an inverter is a DC voltage source or DC rectified voltage and the output is an alternating voltage of variable frequency across its load [38]. There are two general types of inverters: voltage source inverter (VSI) and current source inverter (CSI). In a VSI, the DC link voltage is supported by a DC capacitor and in a CSI the DC bus is maintained by use of a large inductor in the DC link [37]. The output of a VSI is a constrained voltage signal and the current depends on the motor load and speed. The output of a CSI is a constrained current signal and the voltage depends on the motor load and speed.

Figure 3.2 shows a schematic of a three-phase VSI inverter. Basically, it consists of six IGBT semiconductor switches. There are three legs a, b, and c and each has two such switches. If the six semiconductors are considered as ideal switches when they are conducting, the voltage across them is zero. Therefore, only one switch per leg can be conducting at the same time. The square-wave voltages v_{a0}, v_{b0} and v_{c0}, represent the phase voltages with respect to the fictitious DC center tap. These voltages can be expressed by Fourier series as presented in Equation 3-1 [36], in which V_d is the DC bus voltage.

$$v_{a0} = \frac{2V_d}{\pi}\left[\cos\omega t - \frac{1}{3}\cos 3\omega t + \frac{1}{5}\cos 5\omega t - ...\right]$$

$$v_{b0} = \frac{2V_d}{\pi}\left[\cos(\omega t - \frac{2\pi}{3}) - \frac{1}{3}\cos 3(\omega t - \frac{2\pi}{3}) + \frac{1}{5}\cos 5(\omega t - \frac{2\pi}{3}) - \ldots\right]$$

$$v_{c0} = \frac{2V_d}{\pi}\left[\cos(\omega t + \frac{2\pi}{3}) - \frac{1}{3}\cos 3(\omega t + \frac{2\pi}{3}) + \frac{1}{5}\cos 5(\omega t + \frac{2\pi}{3}) - \ldots\right]$$ **Equation 3-1**
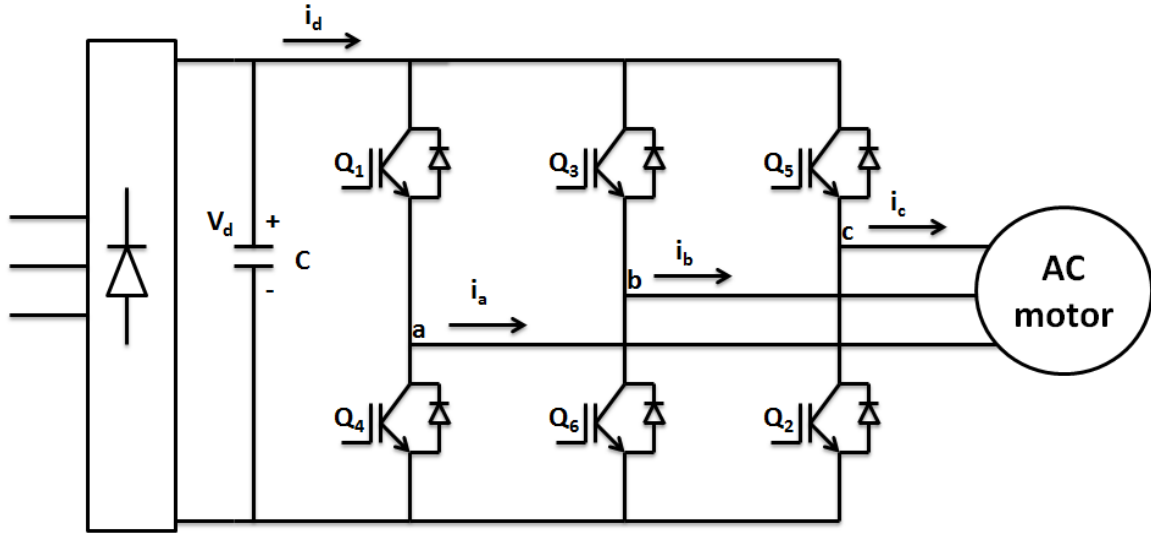
Figure 3.2: Schematic of a three-phase VSI inverter

The VSI inverter output voltage is controlled by pulse-width modulation (PWM) techniques, which generate appropriate switching commands. The most common PWM techniques are: sinusoidal PWM (SPWM), hysteresis and space vector PWM. In Chapters 4 and 5, SPWM is used as modulation technique. In SPWM, a triangle carrier wave is compared with a sinusoidal modulating wave generated at the output of the motor controller. The points of intersection between these two signals define the switching points of the inverter switches.

3.2 Control Schemes for AC Drives

There are three main control approaches for AC motor drives: scalar, vector and direct torque control. A brief explanation of each control scheme is provided. In this dissertation,

vector control is used as control scheme to drive the motor emulating the performance of an aeroderivative engine.

3.2.1 Scalar Control

In scalar control, only the magnitude variation of the control variables is considered and the coupling effect in the machine is disregarded. Scalar control is in contrast to vector control, where both the magnitude and phase alignment of vector variables are controlled. Since the implementation of scalar control is easy, this scheme is used in simple industrial applications when there is no need for a high performance drive. However, scalar controlled drives give somewhat inferior performance compared to vector-controlled drives. Volts/Hz control is an example of a scalar control scheme. In Volts/Hz control, the controlled variables are the motor voltage and frequency and the control objective is to drive the motor with a constant voltage/frequency ratio in order to maintain the motor stator flux constant. This type of control operates in open-loop mode [38].

3.2.2 Vector Control

Currently, vector control is considered as a very powerful technique for AC motor drives. Vector control methods allow AC motors to emulate the control features of DC motors by decoupling the control of flux and torque [39]. A conceptual description of vector control was proposed by [40] who introduced the concept of "field orientation", in which the motor armature currents are resolved into d- and q-axes and the d-component of the stator flux is forced to zero. Vector control operates in closed-loop mode and consists of a two-loop control structure: The outer loop contains the speed controller, the output of which is the reference value of the motor electromagnetic torque, and the inner loop contains the current controller, which indirectly controls the motor electromagnetic torque by controlling the motor currents. This control scheme requires a modulation technique to control the inverter output voltage signals.

26

3.2.3 Direct Torque Control

In direct torque control the controlling variables are the motor magnetizing flux and the torque. No speed or position feedback is required since field orientation is achieved by using theoretical calculations to compute the motor torque. Also, there is no need for a modulation technique. This type of control scheme achieves a faster torque response compared to vector control. Direct torque control has two fundamental control loops: the torque control loop and the speed control loop. Control of the power switches is obtained from a torque and flux comparator based on a two level hysteresis control method [41]. However, the use of a hysteresis method gives rise to larger torque values and flux ripple.

3.3 Control of a Synchronous Motor Drive

In this dissertation a synchronous motor is used as emulating motor for the systems described in Chapters 4 and 5. A synchronous machine rotates at synchronous speed which means that the speed is uniquely related to the supply frequency. The machine consists of a stator winding and a rotor winding that carries DC current. The production of air gap flux allows the stator induced rotating magnetic field to drag the rotor along with it. A synchronous machine can operate with a leading, lagging or unity power factor [36].

The synchronous motor is often the choice for large drives because of its high efficiency and special ability to provide a system power factor improvement. The large air gap of synchronous motors relative to that in an induction motor allows the use of larger stator slots, which is an important advantage for high voltage, high power applications [42]. Hence, synchronous motors are more efficient than induction motors at high power levels. Vector-controlled induction motor drives have been used mostly in the industry for medium power ranges, while vector-controlled synchronous motor drives are either in the very high power

ranges (1-10 MW) with wound-field machines or in the few kilowatt range with permanent

magnet synchronous motors (PMSM) or synchronous reluctance motors for servo drives [36].

3.3.1 Synchronous Motor Vector Control

Figure 3.3 shows a vector control scheme for a synchronous motor that is based on [36],

[43] and [44]. The main components of the vector control scheme are described as follows:

1. **Flux controller:** The monitored rotor speed serves as input to the flux reference

   determination block, the output of which is either a constant value of the stator flux

   reference, $\left| \Psi_s^* \right|$, when the motor is operated below base speed, or a reduced value of the

   stator flux when the motor is operated above base speed. The stator flux reference is

   compared with the actual value of the stator flux, $\left| \Psi_s \right|$, obtained from the flux observer

   and their difference is fed into the flux controller, which is a PI controller. The output of

   the flux controller is the reference value of the magnetizing current, i_m^*, required to

   establish the desired $\left| \Psi_s^* \right|$.

2. **Field current controller:** At steady-state, the field current, i_f, is related to the

   magnetizing current, i_m, by Equation 3-2.

$$i_f = \frac{i_m}{\cos \delta} \qquad\qquad \textbf{Equation 3-2}$$

, where δ is the angle between the i_m and i_f phasors. This equation establishes the field

current command, i_f^*, which is then compared to the actual value of the field current, i_f.

The field current controller generates the field voltage command, v_f, through a PI

controller.

3. **Flux observer:** An observer is usually implemented to reconstruct the inaccessible states in a system. The flux observer allows the calculation of the stator flux, $\left| \Psi_s \right|$, by using the machine parameters and currents. The flux observer is defined in Equation 3-3, which defines the d- and q-axis stator flux components, Ψ_{ds} and Ψ_{qs}, respectively, in terms of machine parameters and currents. The flux observer as defined in [44] only applies for a synchronous machine with one d- and one q-axis damper winding. In this dissertation, the machine model that is used in the emulation studies in Chapter 4 describes a round rotor synchronous machine, which has one d-axis and two q-axis damper windings. Therefore, the mathematical expression for Ψ_{ds} remains the same as defined in [44], but the expression for Ψ_{qs} is recalculated as presented in Equation 3-3.

$$\psi_{ds} = L_{md}(i_f + i_{ds}) \frac{1 + p\left(\dfrac{L_{lkd}}{R_{kd}}\right)}{1 + p\left(\dfrac{L_{md} + L_{lkd}}{R_{kd}}\right)}$$

$$\psi_{qs} = i_{qs} \frac{\left(L_{mq}L_{lk1q}L_{lk2q}\right)s^2 + L_{mq}(R_{k1q}L_{lk2q} + R_{k2q}L_{lk1q})s + L_{mq}R_{k2q}R_{k1q}}{(L_{mq}(L_{lk1q} + L_{lk2q}) + L_{lk1q}L_{lk2q})s^2 + (L_{lk2q}R_{k1q} + L_{lk1q}R_{k2q} + L_{mq}(R_{k1q} + R_{k2q}))s + R_{k1q}R_{k2q}}$$

Equation 3-3

The output of the flux observer yields $\left| \Psi_s \right|$, $sin(\alpha)$ and $cos(\alpha)$, which are calculated using Equation 3-4. The flux components, $\Psi_{ds}{}^s$ and $\Psi_{qs}{}^s$, are obtained by applying the d-q/d^s-q^s transformation to the flux components obtained in Equation 3-3.

$$|\psi_s| = \sqrt{(\psi_{ds}^s)^2 + (\psi_{qs}^s)^2}$$

$$\cos(\alpha) = \frac{\psi_{ds}^s}{|\psi_s|}$$

$$\sin(\alpha) = \frac{\psi_{qs}^s}{|\psi_s|}$$

Equation 3-4

The reference torque current component, i_T^*, is calculated using Equation 3-5.

$$i_T^* = \frac{T_e}{\frac{3}{2}P|\psi_s|}$$

Equation 3-5

4. **Speed and current controllers:** In the speed controller, the reference and monitored rotor speeds are compared and their difference is fed into a PI controller, which yields the reference value of the motor electromagnetic torque, T_e. In the current controllers, the flux component of the stator current, i_M^*, is given by Equation 3-6.

$$i_M^* = i_m^* - i_f \cos\delta$$

Equation 3-6

At steady state it is expected that $i_M^*=0$ since the required magnetizing current is produced only by the field winding. The command currents i_T^* and i_M^* are compared with the respective feedback currents and the errors generate the reference voltage signals, v_T^* and v_M^*, through the PI controllers. These voltage signals are then transformed to the

three-phase stationary reference frame to generate the phase voltage inverter command signals.

5. **Transformation blocks:** The *a-b-c*/d^s-q^s block transforms the three-phase stationary reference frame, *a-b-c*, variables into two-phase stationary reference frame variables, d^s-q^s, by using Equation 3-7. The d^s-q^s/*d-q* block transforms these variables to a synchronously rotating reference frame, *d-q*, by using Equation 3-8. The *d-q*/d^s-q^s and d^s-q^s/*a-b-c* blocks perform the inverse transformations.

$$\begin{bmatrix} i_{qs}^s \\ i_{ds}^s \end{bmatrix} = \frac{2}{3} \begin{bmatrix} 1 & -\dfrac{1}{2} & -\dfrac{1}{2} \\ 0 & -\dfrac{\sqrt{3}}{2} & \dfrac{\sqrt{3}}{2} \end{bmatrix} \begin{bmatrix} i_{as} \\ i_{bs} \\ i_{cs} \end{bmatrix} \qquad \textbf{Equation 3-7}$$

$$\begin{bmatrix} i_{qs} \\ i_{ds} \end{bmatrix} = \begin{bmatrix} \cos\theta_e & -\sin\theta_e \\ \sin\theta_e & \cos\theta_e \end{bmatrix} \begin{bmatrix} i_{qs}^s \\ i_{ds}^s \end{bmatrix} \qquad \textbf{Equation 3-8}$$

The equations relating $i_{ds}{}^s$ and $i_{qs}{}^s$ to i_M and i_T are given by Equation 3-9. The equations relating $v_M{}^*$ and $v_T{}^*$ to $v_{ds}{}^{s*}$ and $v_{ds}{}^{s*}$ are given by Equation 3-10.

$$i_M = i_{ds}^s \cos\alpha + i_{qs}^s \sin\alpha$$

$$i_T = -i_{ds}^s \sin\alpha + i_{qs}^s \cos\alpha \qquad \textbf{Equation 3-9}$$

$$v_{ds}^{s\ *} = v_M^* \cos\alpha - v_T^* \sin\alpha$$

$$v_{qs}^{s\,*} = v_M^* \sin\alpha + v_T^* \cos\alpha \qquad\qquad \textbf{Equation 3-10}$$
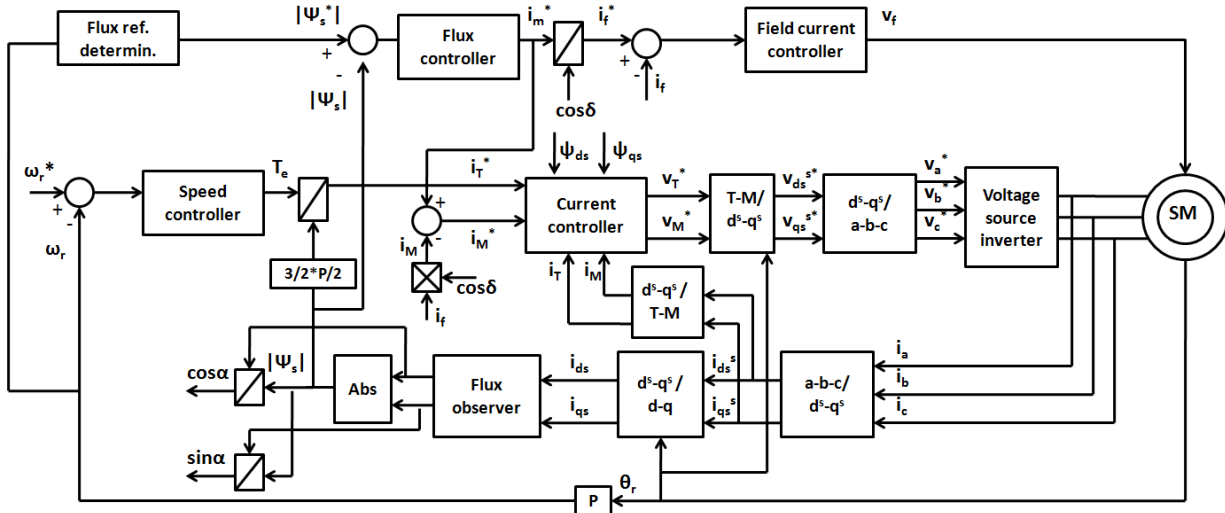
Figure 3.3: Synchronous motor vector control scheme

3.4 Control of an Induction Motor Drive

In this dissertation an induction motor is used as emulating motor for the system described in Chapter 6. In an induction machine, a three-phase supply in the stator winding creates a synchronously rotating magnetic field. This field induces electromagnetic forces in the rotor windings. The rotor windings are short-circuited, and hence currents begin circulating in them and producing a reaction to counter induced emfs in the rotor and the rotating magnetic field, in turn. The induced emfs can be countered if the difference in the speed of the rotating magnetic field and rotor becomes zero. However, in this case the emf becomes zero, and hence the rotor currents also become zero resulting in zero torque production. Therefore, the rotor speed, ω_r, is determined by the load on the shaft and is always less than the speed of the rotating magnetic field, called the synchronous speed of the machine, ω_e. The speed differential is the slip speed, ω_{sl} [38]. In an induction machine the power factor is always lagging since the rotor

excitation is supplied by the stator. Induction machines are the most common type of AC machines used in the industry. They are available in the ranges of fractional horse to multi-megawatt power [36].

3.4.1 Induction Motor Vector Control

There are two general vector control methods for induction motors: the direct or feedback method, and the indirect or feedforward method. This subsection focuses on the latter method. The difference between the direct and indirect methods is how the unit vectors ($cos(\theta_e)$ and $sin(\theta_e)$) are calculated [36]. In the direct method, the unit vectors are generated from flux vector signals $\psi_{dr}{}^s$ and $\psi_{qr}{}^s$, which are calculated by using the motor terminal voltages and currents.

In the indirect control method, the unit vectors are generated from the synchronous speed, ω_e, which depends on the rotor speed, ω_r, and the slip speed, ω_{sl}. The speed, ω_r, can be measured by using an encoder but ω_{sl} needs to be derived by using Equation 3-11. In this equation, K_s refers to the slip gain.

$$K_s = \frac{\omega_{sl}^*}{i_{qs}^*} = \frac{L_m R_r}{L_r \psi_r}$$

Equation 3-11

Once ω_{sl}^* is calculated then the electrical position, θ_e, can be computed from Equation 3-12.

$$\omega_e = \omega_r + \omega_{sl}$$

$$\theta_e = \int \omega_e \, dt$$

Equation 3-12

Figure 3.4 shows the indirect vector control scheme for an induction motor. The speed and current controllers are usually implemented by using PI controllers. For decoupling control of flux and torque it is desirable that

$$\psi_{qr} = 0$$

$$\frac{d\psi_{qr}}{dt} = 0 \qquad \text{Equation 3-13}$$

In this way, Ψ_r can be directed on the d axis. When Equation 3-13 is used in the machine flux linkage equations, which are expressed in terms of flux and inductance terms, then Equations 3-11 and 3-14 can be obtained.

$$\frac{L_r}{R_r}\frac{d\psi_r}{dt} + \psi_r = L_m i_{ds} \qquad \text{Equation 3-14}$$

Usually, Ψ_r is constant in steady-state, so Equation 3-14 becomes,

$$\psi_r = L_m i_{ds} \qquad \text{Equation 3-15}$$

It also follows that,

$$T_e = \frac{3}{2}\frac{P}{2}\frac{L_m}{L_r}\psi_r i_{qs} \qquad \text{Equation 3-16}$$

In this way, the electromagnetic torque only depends on the q component of the armature current and the rotor flux only depends on d component. This results in decoupling of flux and torque. The parameter K in Figure 3.4 corresponds to

$$K = \frac{3}{2} \frac{P}{2} \frac{L_m}{L_r}$$

Equation 3-17

In Figure 3.4 the rotor flux, Ψ_r, is estimated using Equation 3-18, which is derived from Equation 3-14.

$$\psi_r = \frac{i_{ds} L_m}{1 + T_r s}$$

Equation 3-18

, where $T_r = L_r/R_r$.

The reference flux, Ψ_r^*, corresponds to the rated machine flux. Flux weakening can be added to this control scheme by adding a closed-loop flux controller.

The transformation block a-b-c/d-q in Figure 3.4 is also described by Equations 3-7 and 3-8. The d-q/a-b-c block performs the inverse transformation.
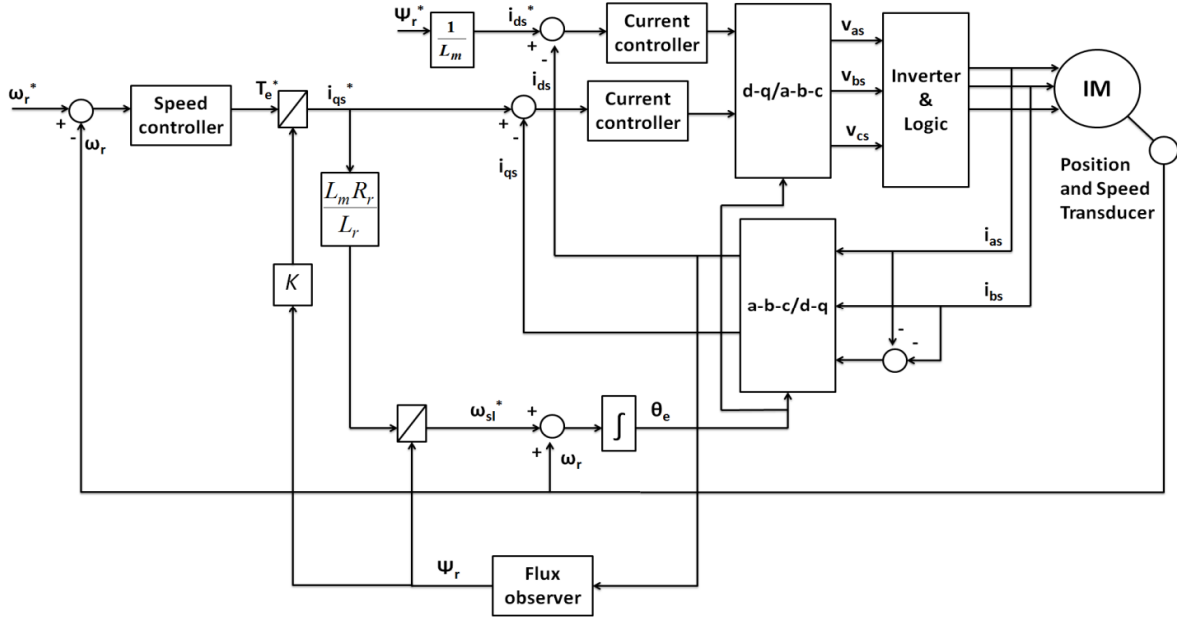
Figure 3.4: Induction motor indirect vector control scheme [36]

3.5 Hardware-in-the-Loop Simulations

HIL simulations are frequently used to assess the performance of AC electric motor drives. HIL is an idea of simultaneous use of simulation and real equipment. Generally, a HIL simulator is composed of a digital simulator, one or more hardware pieces under test, and their analog and digital signal interfaces [45]. HIL testing requires the model and the simulator to perform in real-time. The preciseness of the simulation model depends on the application and computer processing limitations.

There are two main types of HIL simulations: controller hardware-in-the-loop (CHIL) and power hardware-in-the-loop (PHIL) simulations. CHIL simulations are used to test controllers in power systems. Therefore, the interface signals only involve analog-to-digital or digital-to-analog converters, and operate at low power and voltage levels (+/- 15 V, mA) [46]. In PHIL, the piece of hardware under test is a power device like a motor or engine. In this case, the interface includes devices for power amplification and converters. This implies that real power is

36

virtually exchanged between the simulation and the hardware under test [47]. In this dissertation, a PHIL simulation is used to test the engine emulation system. Figure 3.5 shows a schematic representation of a PHIL simulation.
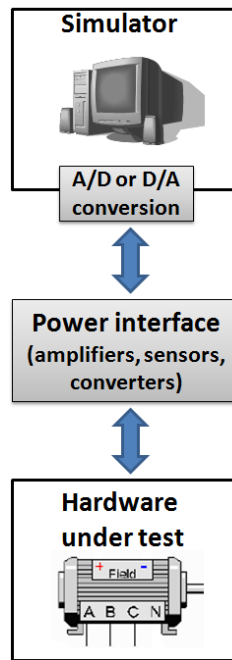
Figure 3.5: Schematic of PHIL simulation

CHAPTER 4: AERODERIVATIVE TWIN-SHAFT ENGINE EMULATION SYSTEM FOR TESTING A HFAC GENERATOR IN SIMULATION

This chapter presents the development of an aeroderivative twin-shaft engine emulation system for testing a HFAC generator in simulation. Two main system models are described: the engine-generator and engine emulation system models. The engine-generator system model consists of an aeroderivative twin-shaft engine driving a HFAC synchronous generator. In the engine emulation system model, a synchronous motor drive is used instead of the engine to drive the HFAC generator. The synchronous motor drive tracks the speed performance of the aeroderivative engine used in the engine-generator system model. Simulation results show the speed tracking performance of the engine emulation system.

4.1 Overview of the Engine Emulation System

The developed engine emulation system model is shown in simplified form in Figure 4.1. As can be seen, an aeroderivative twin-shaft engine reference model provides the appropriate speed reference for a synchronous motor drive so that the motor tracks the speed performance of the engine model [48]. The synchronous motor drives a HFAC six-phase synchronous generator in simulation. The generator runs at 754 rad/s, 233 Hz and operates at 6.6 kV and 14 MW. This is the same operating power level of the engine model. Since the actual synchronous motor that will be used is capable of running up to only half of the speed of the engine, that is 377 rad/s, it is connected to the synchronous generator by a gear box with a ratio of 1:2. It is to note that the synchronous motor has a higher power rating than the aerederivative engine since it is rated for

26.25 MW. It is also important to note that the inertia of the free turbine in the engine model is 1 kg·m^2, while the inertia of the synchronous motor is 551 kg·m^2. As mentioned in Chapter 1, this huge difference in inertia can impose a major challenge in the emulation studies because the synchronous motor needs to develop a larger torque to track the speed of the engine model. By setting the power of the emulating motor larger than the engine model the motor can develop a larger torque than if it was rated for the same power of the engine.
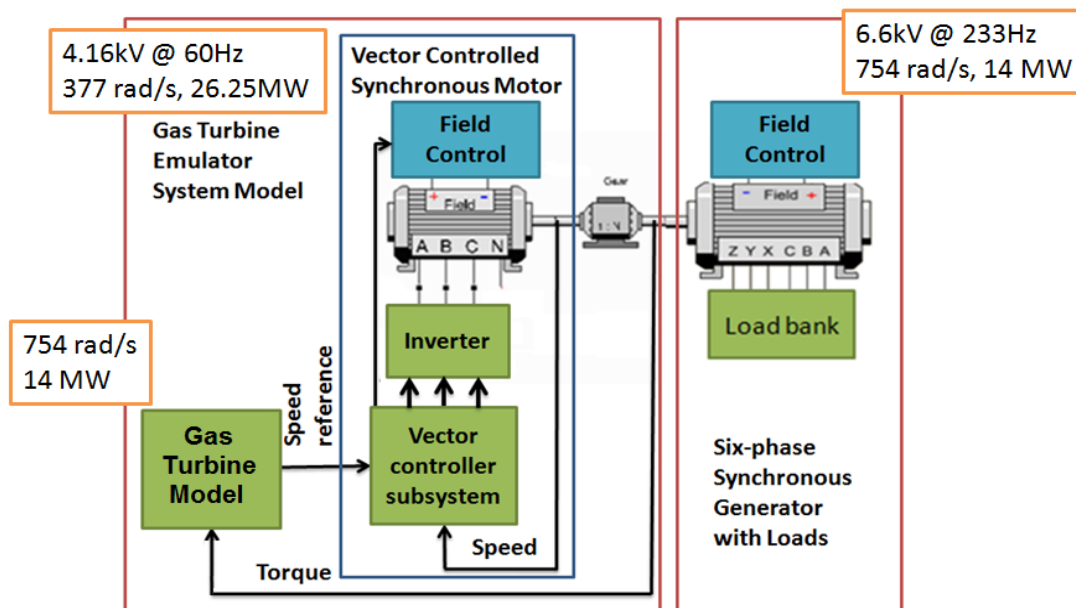
Figure 4.1: Schematic of engine emulation system model

In this study, two system models are developed and implemented in the Virtual Test Bed (VTB) software. The engine-generator system model consists of an aeroderivative twin-shaft engine driving a HFAC generator, and the engine emulation system model consists of a vector controlled synchronous motor drive that emulates the aeroderivative twin-shaft engine in order to drive the HFAC generator. The engine-generator and engine emulation system models are described in the next sections.

4.2 Engine-Generator System Model

Figure 4.2 shows the implementation of the engine-generator system model in VTB. A physics-based engine model (Engine Model 1) operating at 754 rad/s and 14MW is used in this study. This engine model is described in Subsection 4.2.1. Engine Model 1 is connected directly to a 14 MW HFAC synchronous generator. The field of the HFAC generator is controlled by a simple PI controller to maintain an output voltage of 6.6 kV. The generator load consists of a six-phase resistor bank. The model of the six-phase synchronous generator and its excitation controller are described in Appendix B.
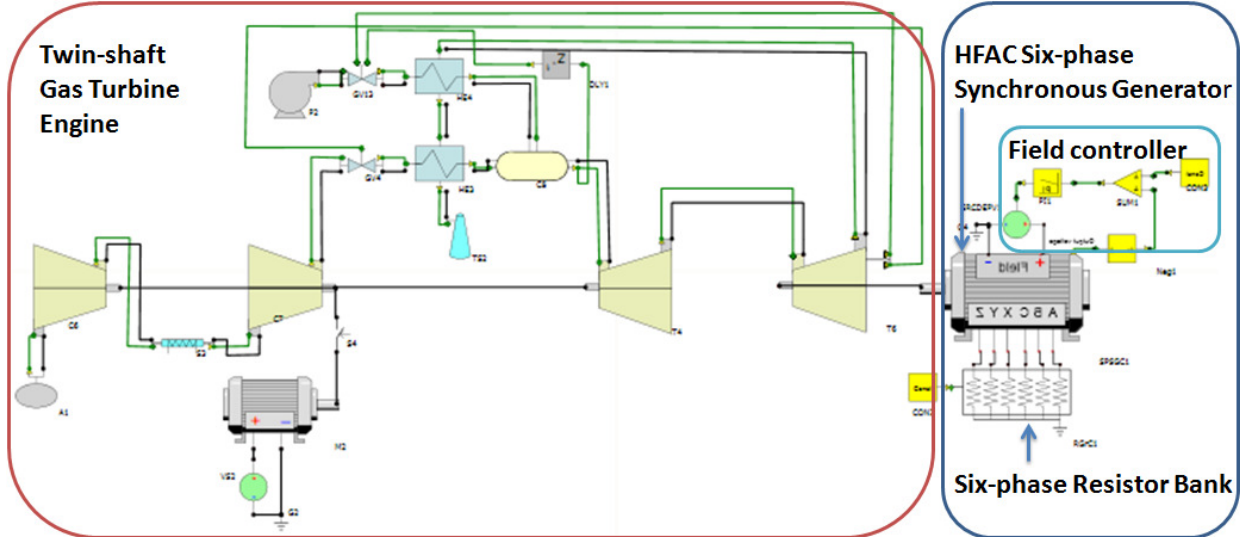
Figure 4.2: VTB simulation of an aeroderivative twin-shaft engine driving a HFAC synchronous generator
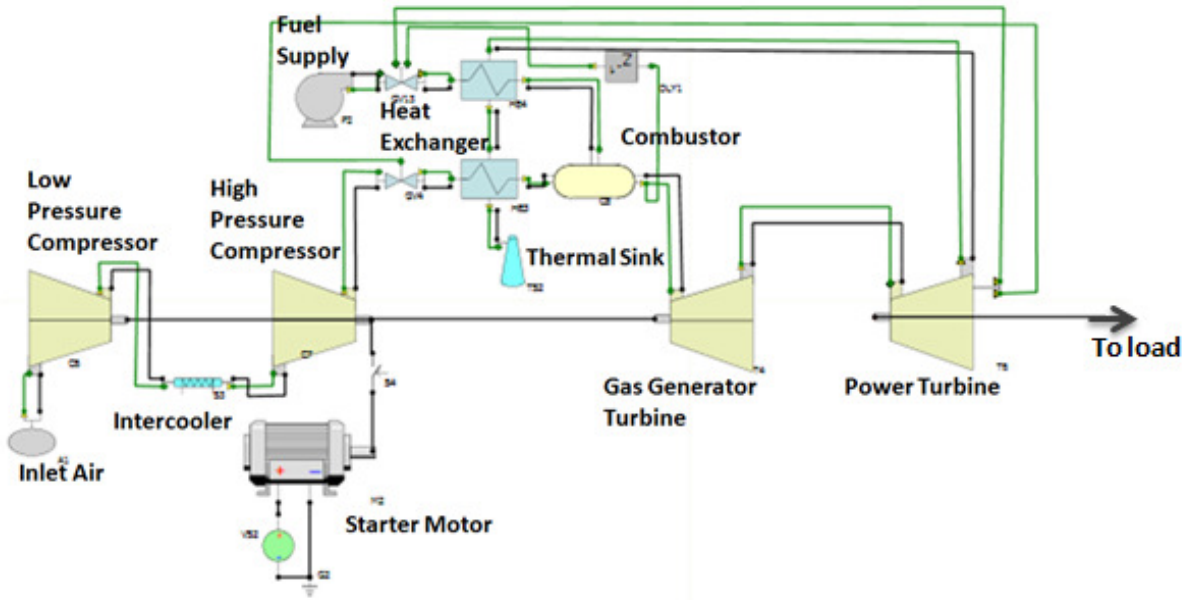
Figure 4.3: VTB implementation of physics-based aeroderivative twin-shaft engine model

(Engine Model 1)

4.2.1 Physics-based Aeroderivative Twin-Shaft Engine Model (Engine Model 1)

Engine Model 1 is based on the mechanical and thermodynamic equations that describe the working principles of an aeroderivatibve, simple-cycle, two-shaft gas turbine engine with intercooler [49], [50]. The different components of Engine Model 1 are emphasized in Figure 4.3. This model is based on [25]. To obtain 1-15 bar air pressure, a two-stage compressor design is implemented. An intercooler is applied to cool the inlet air temperature of the second compressor to achieve higher compression efficiency. The compressed air and fuel are channeled to the combustor. After combustion occurs, the high temperature exhaust gas expands through the two turbines, whereby mechanical power is generated. The power generated by the first gas turbine is fully consumed by the compressors. Subsequent gas expansion through the power or free turbine produces additional mechanical power for electrical power generation. A

motor is used for system start-up and it is cut off automatically after reaching a specific rotational speed. The specific component models are described as follows.

1. **Gas turbine:** Thermodynamic relations and energy transfer are mainly considered for accurate prediction of the turbine characteristics. From the Euler's pump equation, the specific enthalpy coming from the fluid should be equal to the power delivered to the outer device, i.e. compressor or generator as expressed in Equation 4-1.

$$\tau_T \cdot \omega = \dot{m} \cdot Cp \cdot \eta_c \cdot T_{ci}\left(1 - \left(\frac{p_{out}}{p_{in}}\right)^{\frac{k-1}{k}}\right) \qquad\qquad \textbf{Equation 4-1}$$

2. **Compressor:** A compressor is modeled to provide pressurized air for the gas turbine. Mass and energy conservation are included in the model development. The air enters the compressor rotor at the inlet with a uniform velocity and leaves at another radius with a uniform velocity. The change in momentum of the fluid is derived from the work done by the rotating rotor. The compressor characteristic equations are described by Equation 4-2.

$$\frac{d\omega}{dt} = \frac{1}{J_c} \cdot (\tau_t - \tau_c)$$

$$\omega \cdot \tau_c = W_c = \dot{m} \cdot \Delta h_{ideal}$$

$$\Delta p = am^2 + bm + c\omega \qquad\qquad \textbf{Equation 4-2}$$

3. **Combustor:** The fuel and air are fed to the combustor, where the combustion reaction defined in Equation 4-3 takes place. It is assumed that fuel ($C_{12}H_{23}$) completely reacts with the excess air.

$$C_{12}H_{23} + 17.75O_2(\dot{x}) \rightarrow 12CO_2 + 11.5H_2O$$
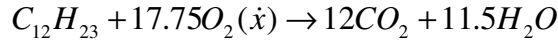
Equation 4-3

$$(\Delta h_{298}^o = -8035.6kJ \,/\, mol)$$

4. **Heat Exchanger:** This model represents a counter flow shell and tube heat exchanger, where phase change of the fluid is not considered. Under the assumption of adiabatic procedure, the total energy transfer can be defined by Equation 4-4.

$$q = \dot{m}_h \cdot c_{p,h} \cdot (T_{h,i} - T_{h,o}) = \dot{m}_c \cdot c_{p,c} \cdot (T_{c,o} - T_{c,i})$$ **Equation 4-4**

, where ε is the overall heat transfer coefficient. For the counter flow shell and tube heat exchanger ε can be defined by Equation 4-5.

$$\varepsilon = 2\left\{1 + Cr + (1 + Cr^2)^{1/2} \cdot \frac{1 + \exp(-NTU \cdot (1 + Cr^2)^{1/2})}{1 - \exp(-NTU \cdot (1 + Cr^2)^{1/2})}\right\}^{-1}$$ **Equation 4-5**

Additional components necessary to operate the engine model include the intercooler, pump, valve, thermal sink and air source. The maximum fuel limit of the engine is a user defined parameter of the fuel valve component model.

4.2.2 Steady-State Performance of the Engine-Generator System Model

The line voltage (phases *a* and *x*) of the HFAC six-phase synchronous generator driven by the aeroderivative engine is shown in Figure 4.4. It can be seen that these two phases are displaced by 60° and the frequency is 240 Hz since the engine speed is 754 rad/s. Figure 4.5 shows that the stator output voltage is controlled at 5388.88 V, the operating speed is 754 rad/s and the mechanical power is 14 MW.

The speed-torque characteristic of the HFAC synchronous generator driven by the twin-shaft engine at three different operating speeds is shown in Figure 4.6. It can be seen that the aeroderivative engine speed controller is able to maintain constant speed but only up to a certain torque value. This is because the fuel reaches its maximum level and beyond this point, the speed controller can no longer maintain the reference speed value and the speed begins to drop. This is considered an overload condition.
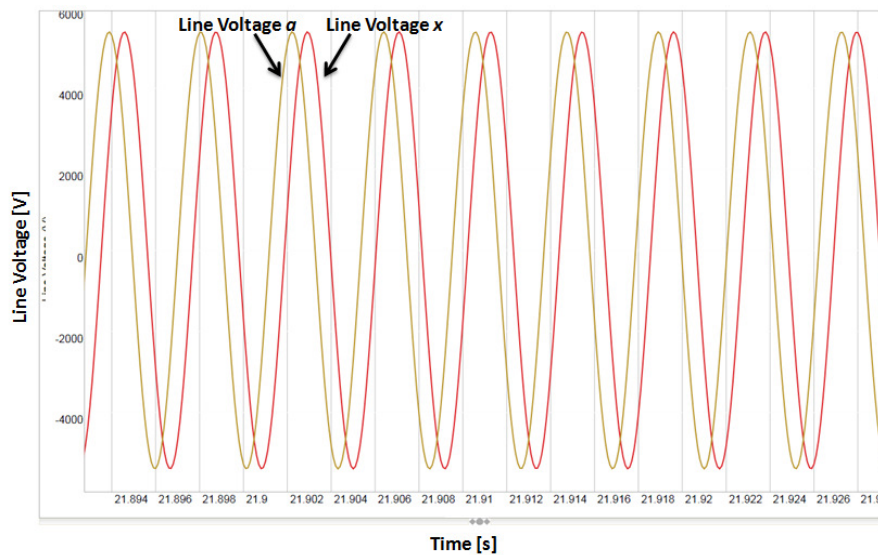
Figure 4.4: Line voltages *a* and *x* of HFAC synchronous generator

44
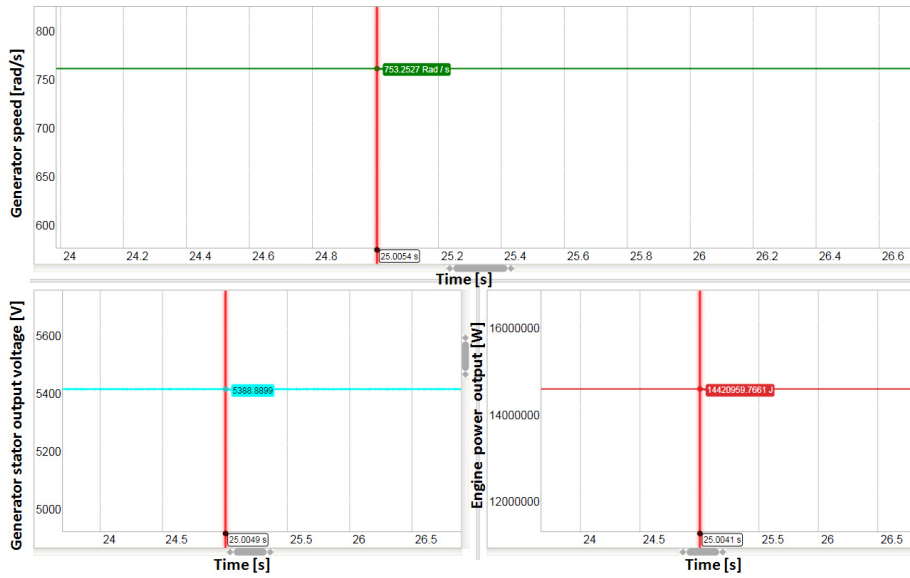
Figure 4.5: HFAC generator speed, and output voltage and power
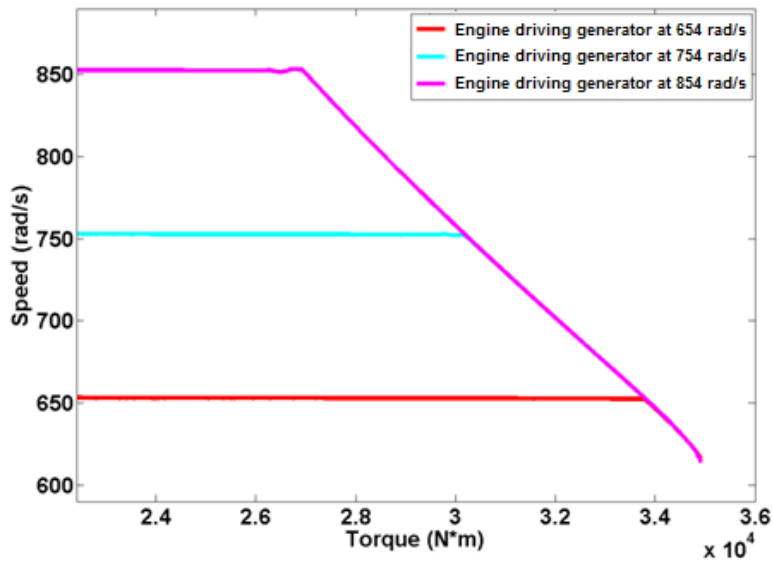
Figure 4.6: Speed vs torque characteristic of engine- generator system

4.2.3 Transient Performance of the Engine-Generator System Model

The transient response of the engine-generator system model is examined in terms of:

- Speed Deviation: Maximum variation of shaft speed from the nominal shaft speed after a perturbation of the electrical load.

45

- Settling Time: Time from application of a load perturbation to the time when the shaft speed is 36 % of the maximum peak excursion.

The upper plot in Figure 4.7 shows the generator shaft speed as a function of time following application of a 20 % step load decrease to the generator. The settling time remains almost invariable (0.53 s) between different sizes of load step changes applied.

The lower plots in Figure 4.7 show the speed deviation (left) and the settling time (right) as a function of the size of the load step-down. It is observed that the maximum speed deviation increases as the load step increases. The settling time is relatively constant for load decreases between 10 % and 50 % of rated power showing the invariability in this system characteristic.
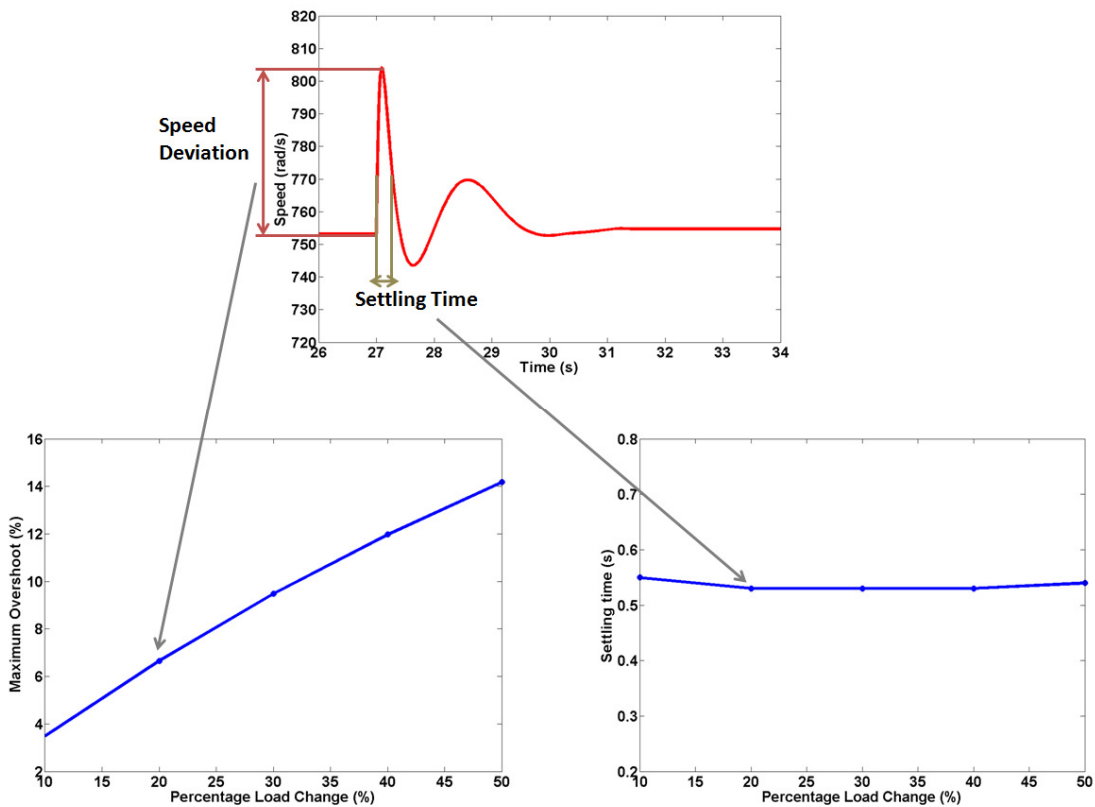
Figure 4.7: Response of engine-generator to a load perturbation

Figure 4.8 shows the maximum speed deviation and the settling time as a function of magnitude of the load decrease when operating the engine-generator system model at 70 % of nominal load. In this case, the maximum speed deviation and the settling time present slightly larger values compared to the nominal case shown in Figure 4.7. Similar to the previous case, the settling time is relatively constant (0.58 s) for load decreases between 10 % and 50 %.
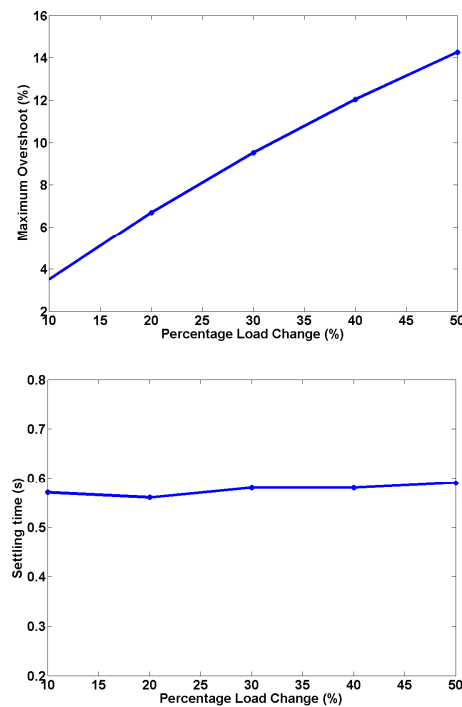
Figure 4.8: Engine-generator system model response to a load perturbation when operating at 70% of nominal load

4.3 Engine Emulation System Model

The implementation of the engine emulation system in simulation is shown in Figures 4.9 - 4.12. The shaft torque of the HFAC is measured by using a current sensor model and is feedback to the output shaft of the aeroderivative twin-shaft engine model. The synchronous

motor vector controller consists of three subsystems: The flux observer subsystem, the speed and current loop controller subsystem, and the flux and field controller subsystem.

The synchronous motor model in this system is described in Appendix A. The synchronous motor standard parameter values are shown in Table 4.1.
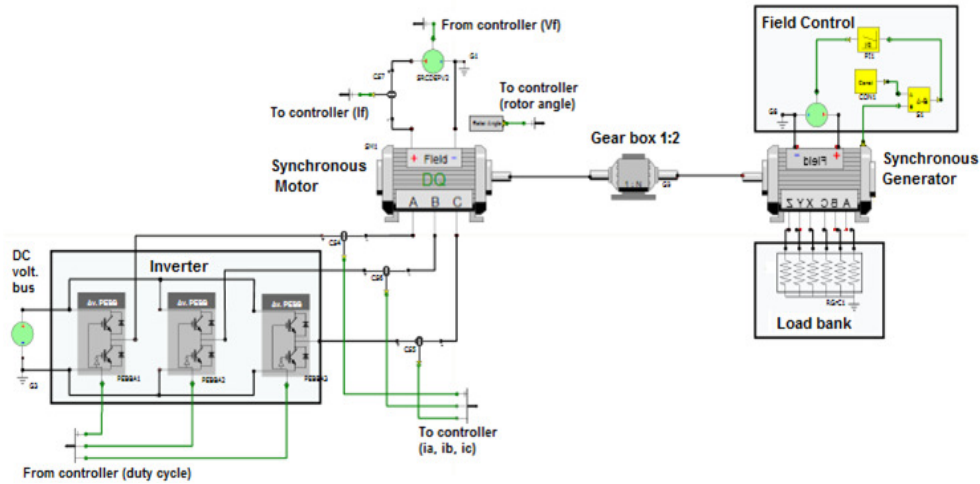
Figure 4.9: Implementation of the engine emulation system in simulation
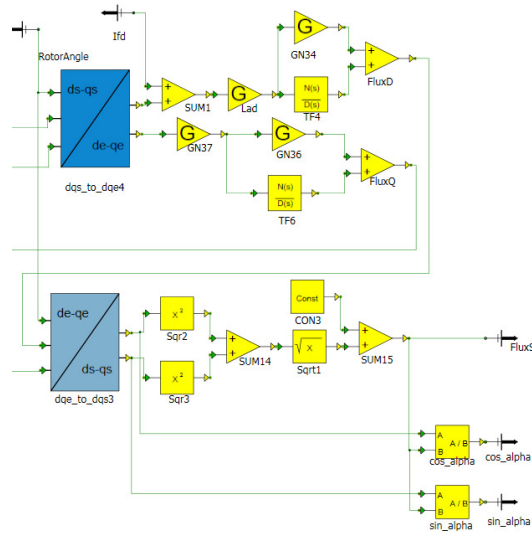
Figure 4.10: Flux observer subsystem
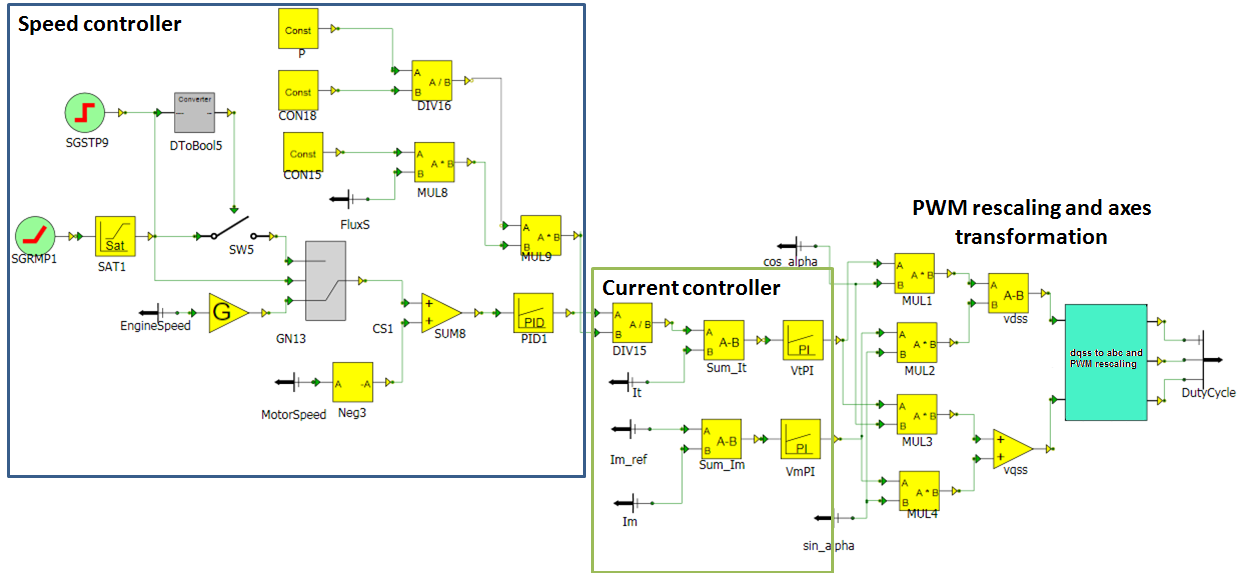
Figure 4.11: Speed and current loop controller subsystem
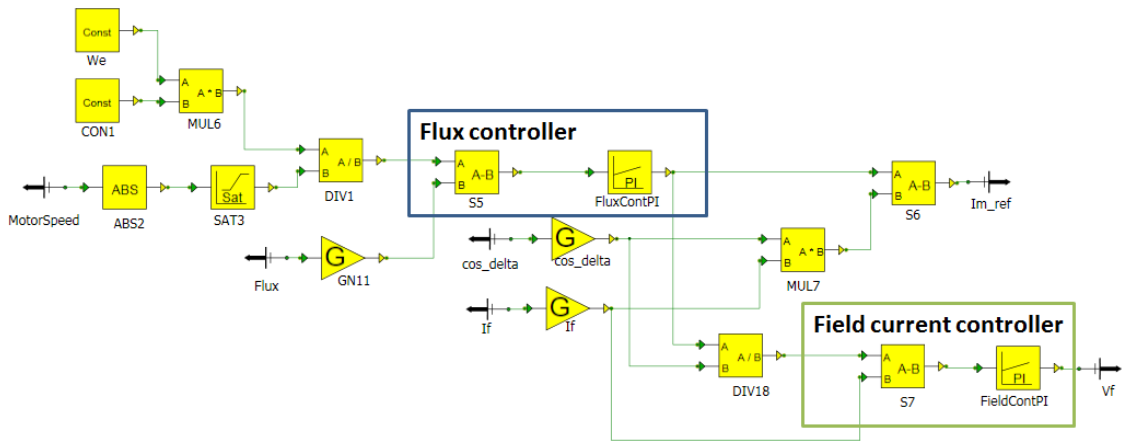
Figure 4.12: Flux and field controller subsystem

Table 4.1: Synchronous motor standard parameters

Line voltage (rms)	4.16 kV
Frequency	60 Hz
Rated Speed	3600 rpm
Power	26.25 MVA
Inertia	551 kg·m^2
Synchronous reactance	2.08 pu
Saturated transient reactance	0.324 pu
Saturated subtransient reactance	0.25 pu
Unsaturated negative sequence reactance	0.268 pu
Unsaturated zero sequence reactance	0.125 pu
Transient O.C. time constant	7.2 s
Transient S.C. time constant	0.85 s
Subtransient O.C. time constant	0.05 s
Subtransient S.C. time constant	0.04 s
R$_s$	0.0129 Ω

4.3.1 Design of Speed Controller

The speed controller of the synchronous motor drive is based on a classical PID controller. The parameters of this controller are calculated according to the frequency tuning technique presented in reference [51]. The following method is based on the general control loop shown in Figure 4.13. The transfer functions $G_c(s)$ and $G_p(s)$ represent the controller and plant transfer functions in the Laplace domain, respectively, and the variables r, u and y represent the reference input, the control input and the output of the system, respectively.
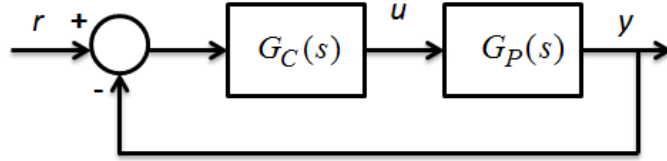
Figure 4.13: Generalized closed-loop control scheme

The open-loop system can be expressed in the frequency domain as shown in Equation 4-6. The transfer functions $G_c(jw)$ and $G_p(jw)$ represent the controller and plant transfer functions in the frequency domain, respectively.

$$G_O(j\omega) = G_C(j\omega)G_P(j\omega)$$
<div align="right">**Equation 4-6**</div>

In order to ensure stability, the open-loop gain at the desired control bandwidth, ω_{bw}, should be unity and the phase should correspond to -180 degrees plus the phase margin, φ_m, as expressed in Equation 4-7.

$$\left| G_O(j\omega) \right|_{\omega_{bw}} = 1$$

$$\left\langle G_O(j\omega) \right|_{\omega_{bw}} = -\pi + \varphi_m$$
<div align="right">**Equation 4-7**</div>

The controller is designed by specifying ω_{bw} and φ_m of the closed-loop system. By using Equations 4-6 and 4-7, the gains K_p and K_i are derived as expressed in Equation 4-8.

$$K_p = \frac{\cos(-\pi + \varphi_m - \varphi_{bm})}{\left| G_O(j\omega) \right|}$$

51

$$K_i = \frac{-\omega_{bw}\sin(-\pi + \varphi_m - \varphi_{bm})}{|G_O(j\omega)|}$$

Equation 4-8

When tuning the speed PID controller it is assumed that the dynamics of the current controllers are sufficiently fast, and the effect of the load torque T_L and the viscous friction coefficient B are neglected. The speed loop of the synchronous motor vector controller is shown in Figure 4.14. The parameter J accounts for the motor inertia as well as the reflected load inertia, P is the number of poles of the machine, T_e is the machine electromagnetic torque, and ω_r is the machine rotor speed. The speed controller is designed to have $\omega_{bw}=5$ *rad/s*, $\varphi_m=60°$, so that $K_p=2463.6$ and $K_i=7111.9$. The value of K_d is set to 30.
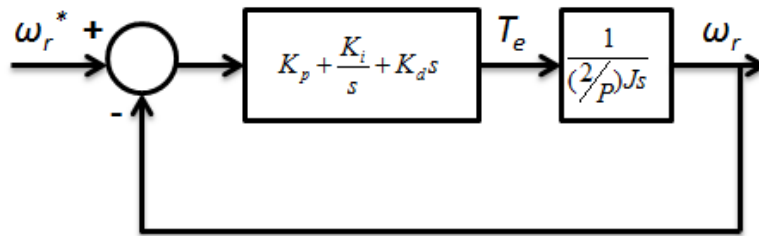
Figure 4.14: Synchronous motor drive speed control loop

4.3.2 Performance of the Vector Controlled Synchronous Motor when using a Constant Speed Reference

The performance of the vector controlled synchronous motor driving the HFAC generator is initially tested by using a constant speed reference. Subsections 4.3.2.1 and 4.3.2.2 include the steady-state and transient performance in this case. Then, Section 4.4 presents the simulations results when the speed reference of the vector controlled synchronous motor drive is provided by the engine model so that the motor operates in emulation mode.

4.3.2.1 Steady-State Performance

Figure 4.15 shows the steady-state performance of the vector-controlled synchronous motor. The motor operates at 377 rad/s and is capable of operating at 26.25 MW. Thus, it can provide a mechanical torque of $69.5 \cdot 10^3$ N·m. As is expected in vector control, the magnetizing current reference, $i_M{}^*$, is zero at steady-state.
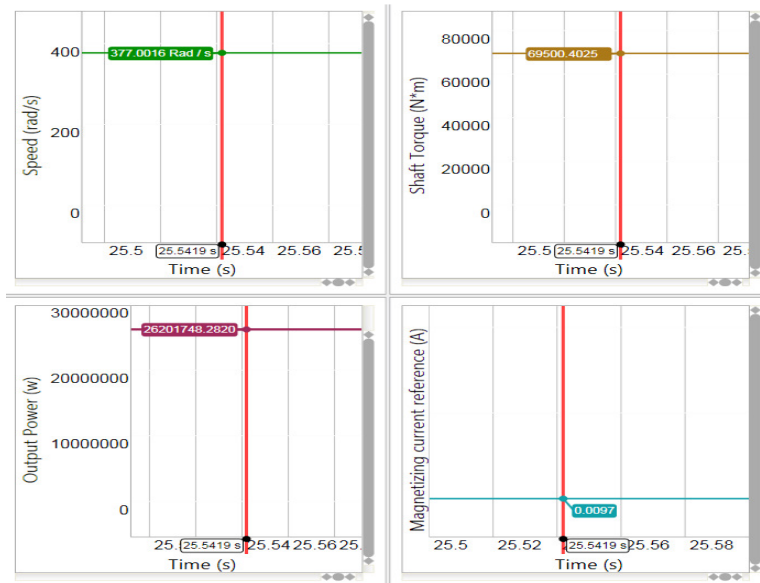
Figure 4.15: Vector-controlled synchronous motor simulation showing steady state motor speed, shaft torque, output power and magnetizing current reference

4.3.2.2 Transient response of the vector controlled synchronous motor when using a constant speed reference

As with the engine-generator system model, the response of the motor-generator system is examined to transient loads when the reference of the synchronous motor speed controller is a constant speed reference. The upper plot in Figure 4.16 shows the generator shaft speed as a function of time when the electrical load is abruptly decreased by 20 %. The settling time remains almost invariable (0.29 s) between different sizes of applied load step changes. The lower plots in Figure 4.16 show the maximum speed deviation (left) and the settling time (right)

as a function of magnitude of the load decrease. As was the case for the engine-generator system model, the maximum speed deviation increases as the load step is increased. The settling time is relatively constant for load decreases between 10 % and 50 % of rated power.

Figure 4.17 shows the maximum speed deviation and the settling time as a function of magnitude of the load decrease when operating the motor-generator system at 70 % of nominal load. In this case, the maximum speed deviation presents slightly lower values compared to the nominal case shown in Figure 4.16. The settling time (0.3 s) is relatively constant for load decreases between 10 % and 50 % of rated power.
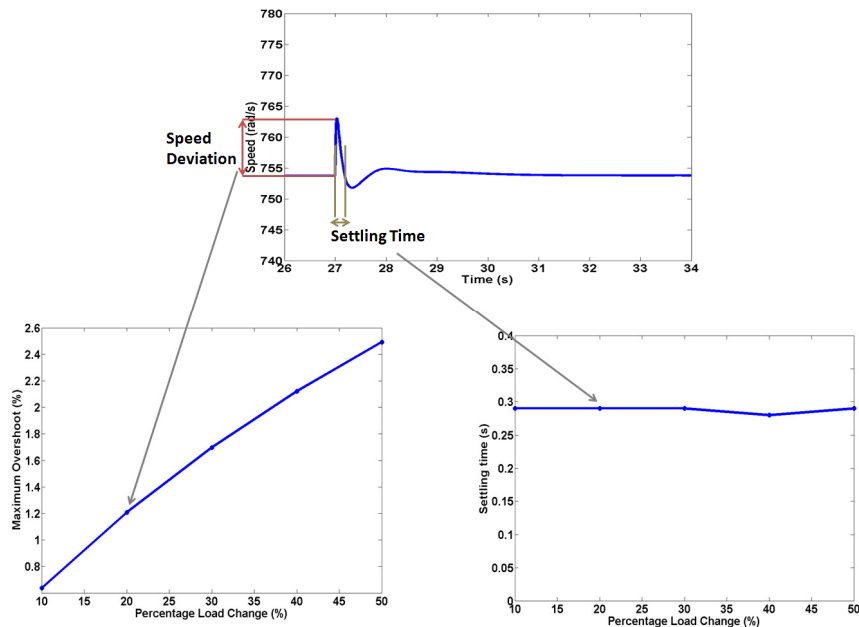
Figure 4.16: Motor-generator system model response to a load perturbation
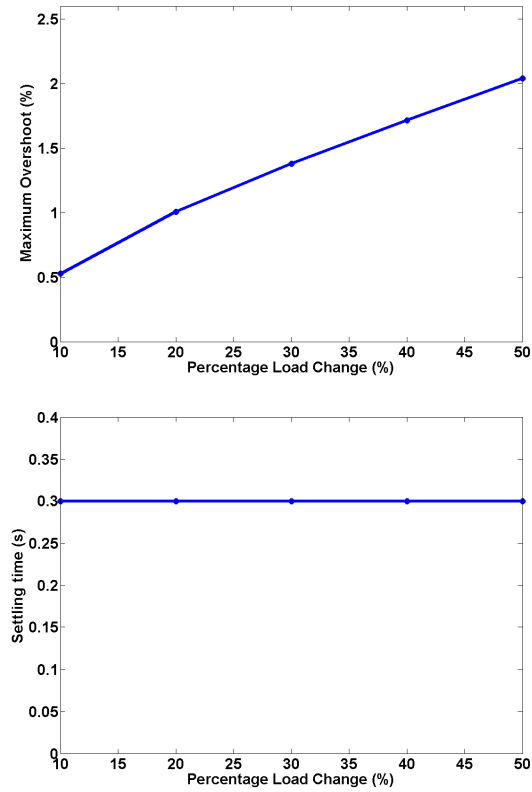
Figure 4.17: Motor-generator system model response to a load perturbation when operating

at 70% of nominal load
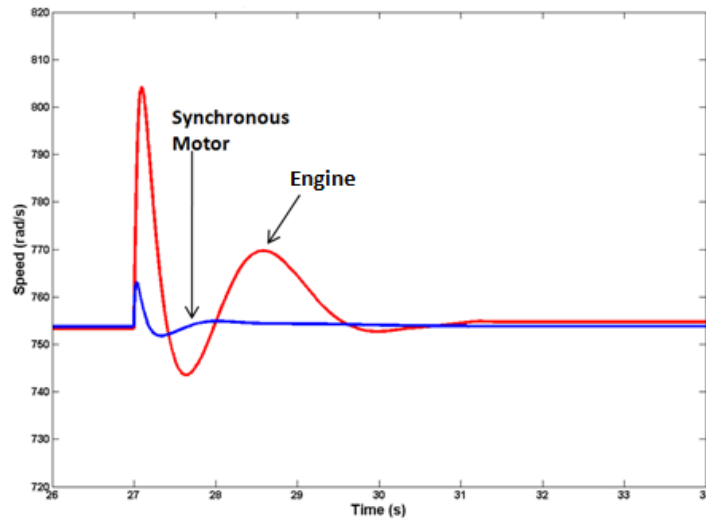
Figure 4.18: Comparison of response to a 20% step load decrease for the engine-generator

and the motor-generator system models

4.3.3 Comparison of Transient Response between Engine-Generator and Motor-Generator System Models

Figure 4.18 compares the responses of the engine-generator system model to that of the motor-generator system model when subjected to a 20 % step load decrease. We see that the deviation of the generator speed when driven by the motor is significantly less than when driven by the engine. There are several reasons for this. First, the larger inertia of the motor inhibits speed-up. Second, the motor controls can react nearly instantaneously to restrict power input to the motor, whereas the fuel control of the engine responds slightly more slowly. This behavior is consistent for other magnitudes of load changes (see Figure 4.7 and Figure 4.16). The more controllable response of the motor compared to the engine is encouraging because it indicates that the addition of appropriate controls can affect a motor speed response that is consistent with the speed response of the engine.

4.4 Engine Emulation Simulation Results

When the engine model provides the speed reference for the emulating motor, the engine-generator system and the engine emulation system should, ideally, exhibit identical behaviors in steady-state operation and in response to system disturbances. This is tested in simulation in order to establish a proof of concept. As previously stated, the synchronous motor inertia is 551 kg·m^2 and the free turbine inertia in the engine model is 1 kg·m^2. According to the available documentation on the Honeywell AGT1500 twin-shaft engine [14], the free turbine rotor has an inertia value of 0.141 kg·m^2. However, it should be noted that the rated power level of the AGT1500 is only 1.12 MW. For this simulation, the rated power of the engine is between 10-14 MW. Since the inertia of the rotor is somewhat proportional to the rated power level it is

estimated that the inertia value of the free turbine can be somewhere in the range of 0.6-1.5 kg·m^2.

Figure 4.19 compares the speed-torque characteristic of the engine-generator system with that of the engine emulation system for constant speed references of 654 rad/s, 754 rad/s and 854 rad/s. At all test points, the two control loops maintain identical speeds, including in the overload range where the engine speed decreases when it reaches the fuel supply limit.

Figures 4.20 and 4.21 compare the generator speed of the engine emulation system, ω_{ge}, to the generator speed of the engine-generator system, ω_g, in response to a step load increase. In the simulation, a 20 % step load increase is applied at t=22 s. The figures show that the emulation system tracks the oscillations of the engine model very accurately. The amplitude of the oscillations is slightly higher for the emulation system than for the engine-generator system. The maximum speed tracking error is 2.975 %, with speed tracking error defined by Equation 4-9.

$$Error = \frac{\omega_{ge} - \omega_g}{\omega_g}$$

Equation 4-9

Figure 4.22 shows the line voltage, phase current and duty cycle of the synchronous motor during the 20 % step load increase. As can be seen, the peak voltage of the synchronous motor is 5.88 kV which corresponds to an rms line voltage of 4.16 kV. At the moment the load is increased the line voltage decreases while the phase current increases. This is because more torque is applied to the motor shaft.
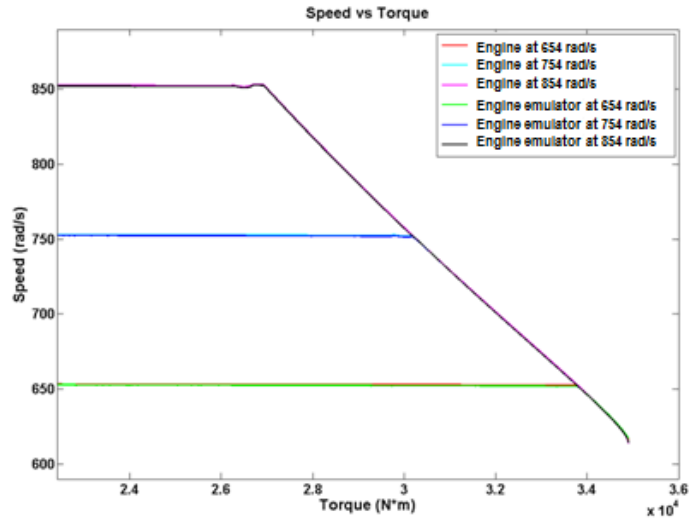
Figure 4.19: Comparison of steady state speed-torque characteristics of engine-generator and engine emulation system models
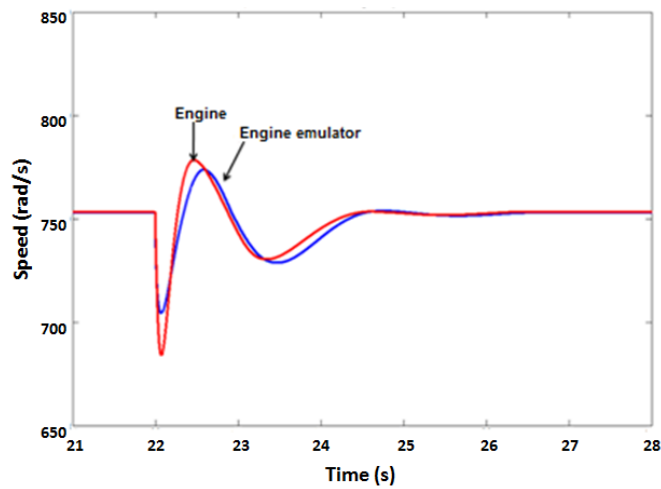
Figure 4.20: Comparison between generator speeds for the engine-generator and engine emulation system models during a step load increase
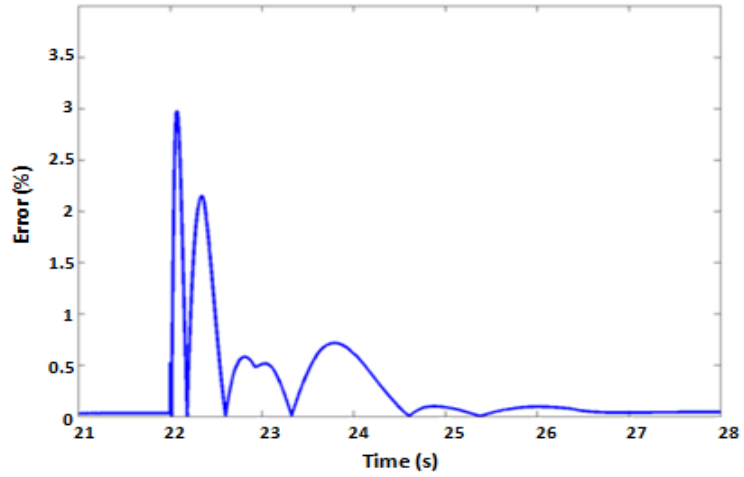
Figure 4.21: Speed tracking error of the engine emulation system model following a 20 %

increase of electric load
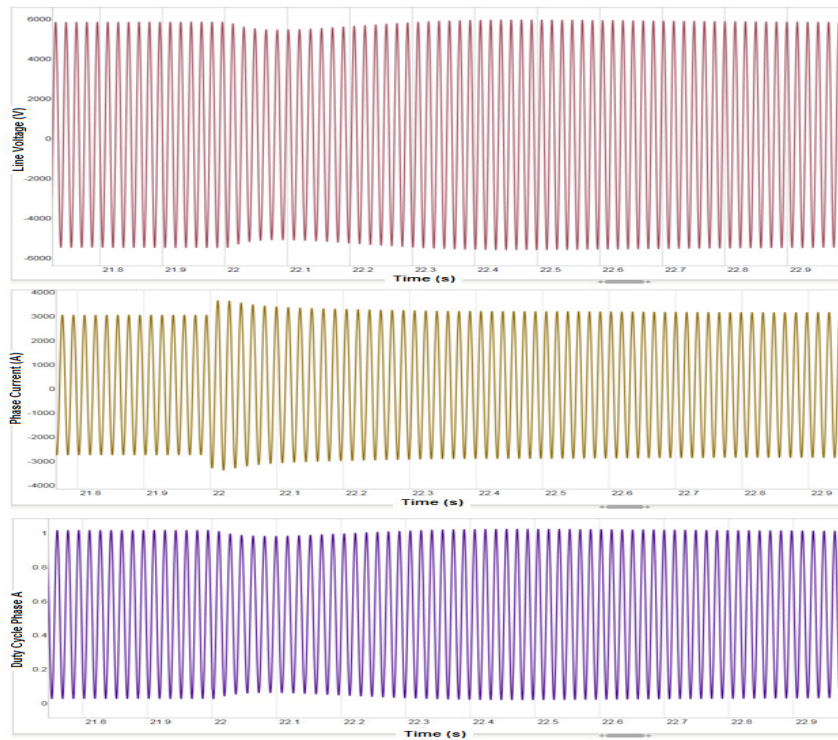
Figure 4.22: Line voltage, phase current and duty cycle of synchronous motor during a 20 %

step load increase

Figures 4.23 and 4.20 compare the generator speeds of the emulation system and the engine-generator system models in response to a step load decrease. In simulation, a 20 % step load decrease is applied at t=22 s. For this case the maximum error is 1.066 %, which is less than in the 20 % step load increase case. This is because the synchronous motor has a larger inertia than the engine's free turbine, and more power must be extracted from the motor (regeneration mode) in order to bring the speed back to steady-state during a step load increase.

Figure 4.25 shows the line voltage, phase current and duty cycle of the synchronous motor during the 20 % step load decrease. At the moment the load is increased the line voltage slightly increases while the phase current decreases. This is because less torque is applied to the motor shaft.
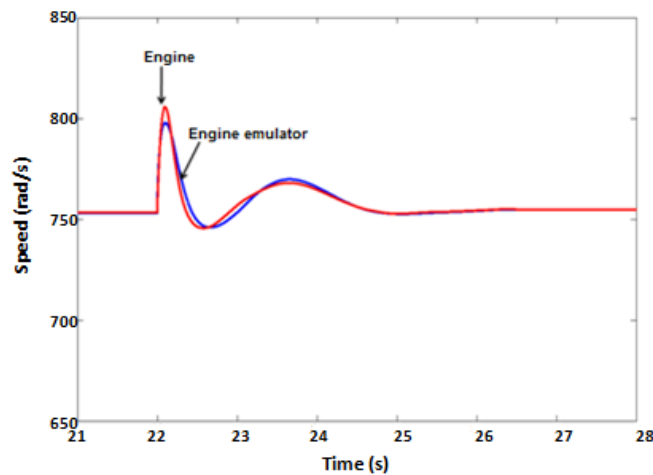
Figure 4.23: Comparison between generator speeds for the engine-generator and engine emulation system models during a step load decrease
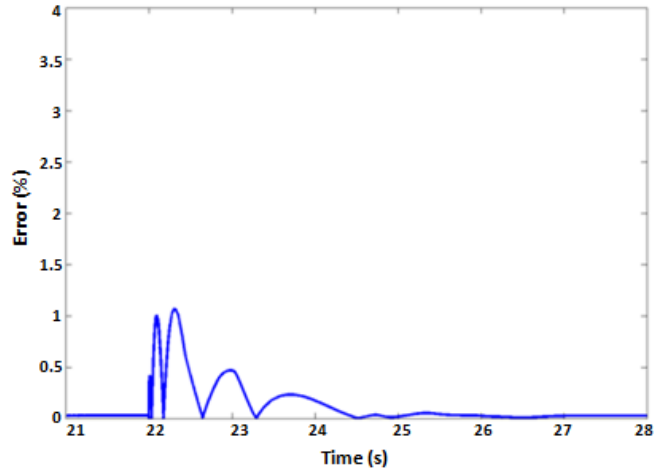
Figure 4.24: Speed tracking error of the engine emulation system model following a 20 %

decrease of electric load
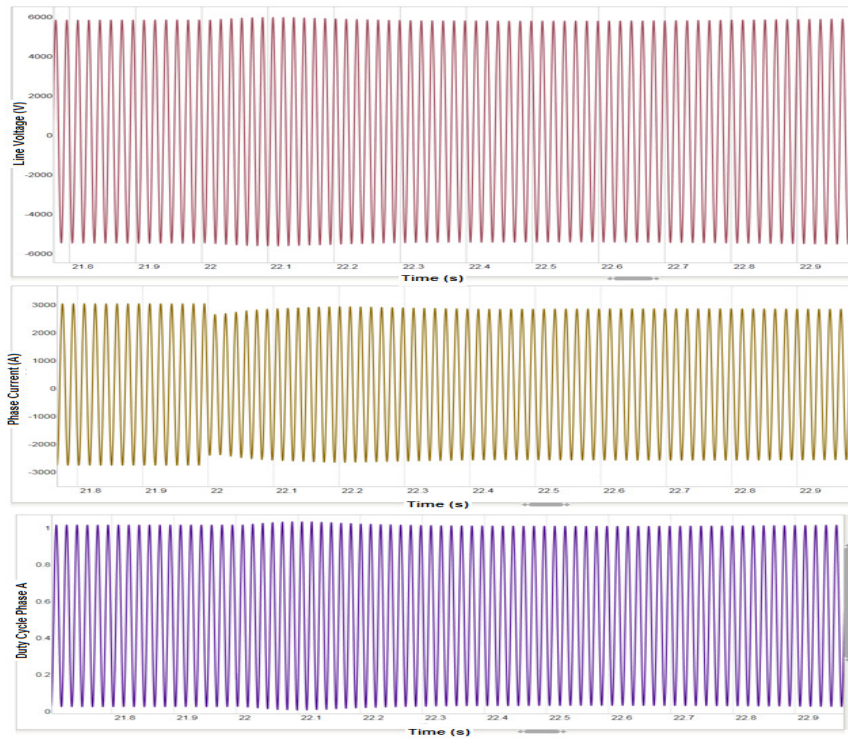
Figure 4.25: Line voltage, phase current and duty cycle of synchronous motor during a 20 %

step load decrease

4.5 Discussion and Chapter Summary

This chapter has demonstrated a method by which a synchronous motor can be controlled so as to emulate the steady-state and dynamic characteristics of an aeroderivative twin-shaft engine in simulation. The emulation system model consists of a 26.25 MW vector controlled synchronous motor that tracks the speed of a 14 MW engine model. The whole system model is tested in simulation with the emulating motor coupled to a 14 MW HFAC synchronous generator. Simulation results have shown that the vector controlled synchronous motor is able to track the steady-state and transient speed behavior of the engine during a 20 % step load increase and decrease, with a tracking error that is below 3 %.

CHAPTER 5: BENCHTOP-SCALE HIL SIMULATION OF AN AERODERIVATIVE TWIN-SHAFT GAS TURBINE ENGINE EMULATION SYSTEM

This chapter presents a model-based control method for using a vector controlled synchronous motor to emulate the behavior of an aeroderivative twin-shaft gas turbine engine as it drives an electric generator supplying power to steady-state and dynamic loads. The method is validated on a benchtop-scale hardware-in-the-loop (HIL) implementation of the engine emulation system. The motor speed controller tracks the output speed of a simulated real-time engine model in order to generate appropriate voltage and frequency demands for the variable speed inverter that drives the motor. The inertia of the synchronous motor is varied by adding inertial loading to its shaft in order to study the effect of emulating a prime mover with a higher inertia than the emulating motor. Experimental results present the tracking performance of the engine emulation system following step changes in the fuel input and electrical loading and unloading of the generator.

5.1 Benchtop-Scale Aeroderivative Engine Emulation System

Figure 5.1 shows the general concept of the developed aeroderivative twin-shaft gas turbine engine emulation system. It can be seen from Figure 5.1, that when the generator is driven by the engine its speed can be affected by variations in the speed reference of the free turbine governor, ω_{ft}^*, which determines the engine fuel demand, and the generator torque, T_{Gen}, which varies according to the armature current, I_a, when a change in electrical load is applied. Therefore, the motor drive includes a speed tracking controller in order to minimize the error

63

between the free turbine speed, ω_{ft}, and the motor rotor speed, ω_r, when variations in ω_{ft}^* and T_{Gen} occur.
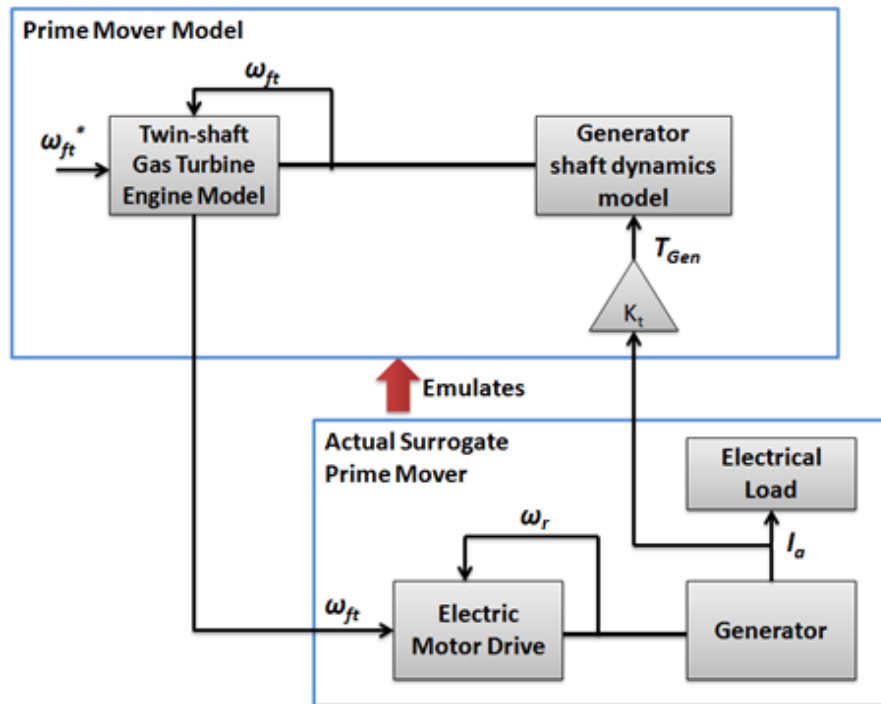
Figure 5.1: Concept of the benchtop-scale aeroderivative engine emulation system

The engine emulation system is implemented in a HIL simulation by using the dSPACE 1104 R&D controller board which includes real-time hardware capability based on PowerPC technology and I/O interfaces [52]. The real-time interface includes Simulink blocks that allow I/O configuration. A Simulink system model can be converted to real-time C code, cross compiled and downloaded to the real-time hardware of the dSPACE simulator. The ControlDesk environment is used as a graphical front-end tool in order to visualize and interact with the I/O signals in real-time.
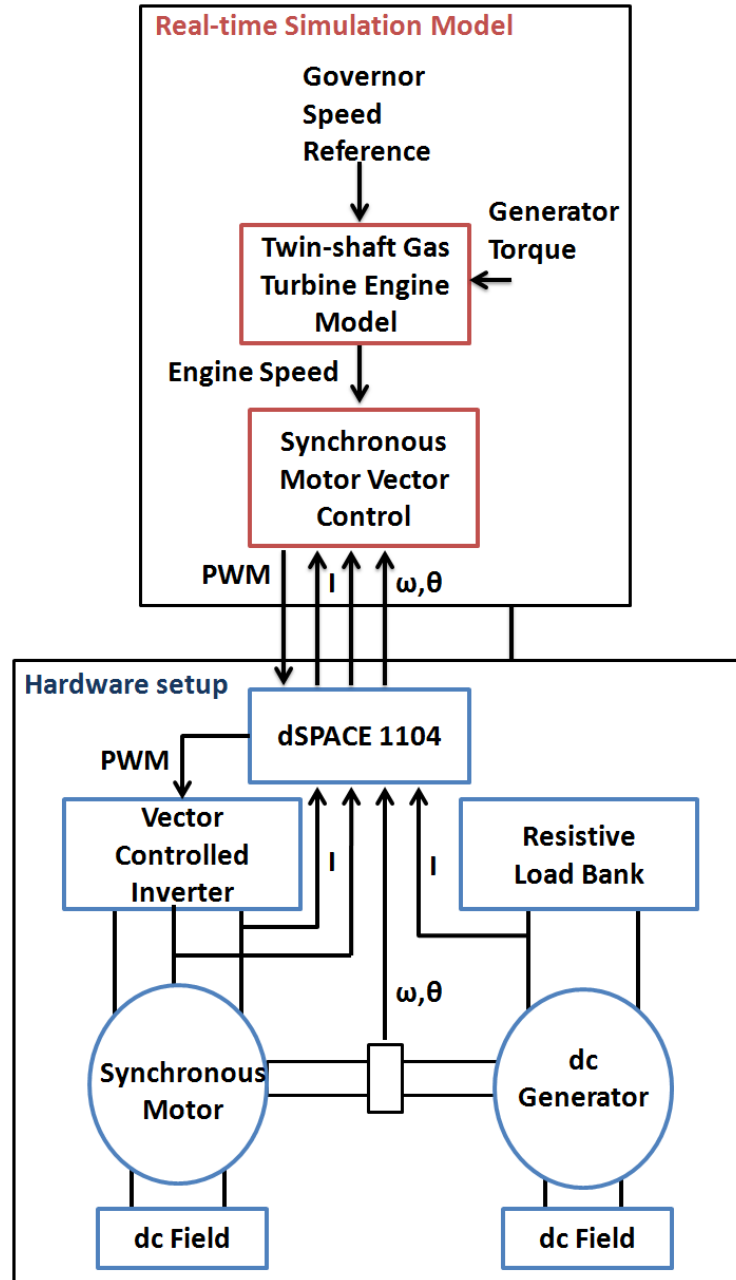
Figure 5.2: Schematic of the benchtop-scale HIL simulation of the aeroderivative engine emulation system

The schematic of the benchtop-scale HIL simulation of the aeroderivative engine emulation system is shown in Figure 5.2. A 0.25 kW synchronous motor driven by a variable speed three-phase inverter is connected to a 0.25 kW DC generator on the same shaft. The real-

time simulation model includes a model of the twin-shaft engine and the vector controller which includes a speed tracking controller. The time step of the real-time simulation model is 0.2 ms and the inverter operates at a switching frequency of 5 kHz. The dSPACE 1104 includes A/D and D/A channels, and encoder signal acquisition ports. The motor vector controller requires measurement of the motor mechanical speed, ω_m, and position, θ, which are provided by an incremental rotary encoder with 2048 cycles per revolution, and two phase armature currents which are measured by using two current sensors and obtained through the A/D interface. A current sensor is also used to measure the armature current of the DC generator in order to obtain the generator torque that is input to the real-time engine model. The D/A interface outputs the appropriate PWM commands for the three-phase inverter. The inverter control system is implemented by an IRAMX16UP60A power module. Figure 5.3 shows the experimental setup of the aeroderivative engine emulation system.
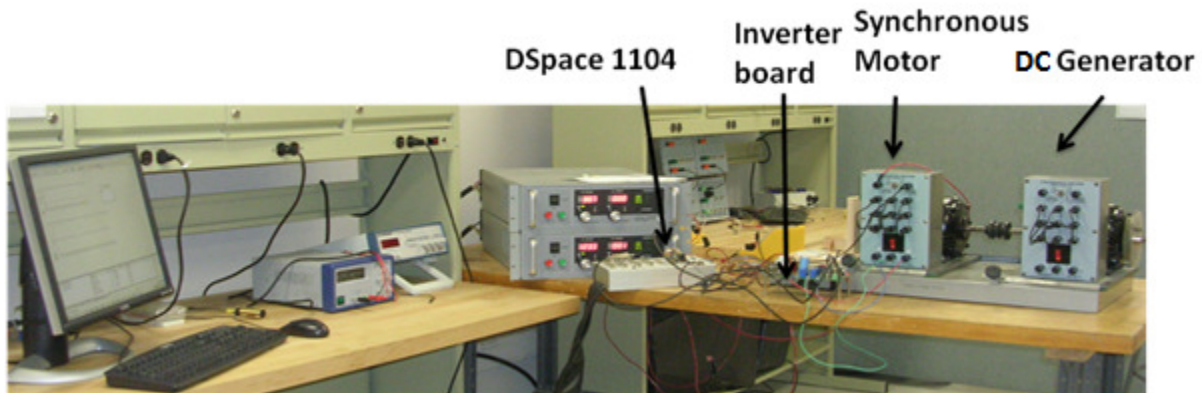
Figure 5.3: Experimental setup of aeroderivative engine emulation system
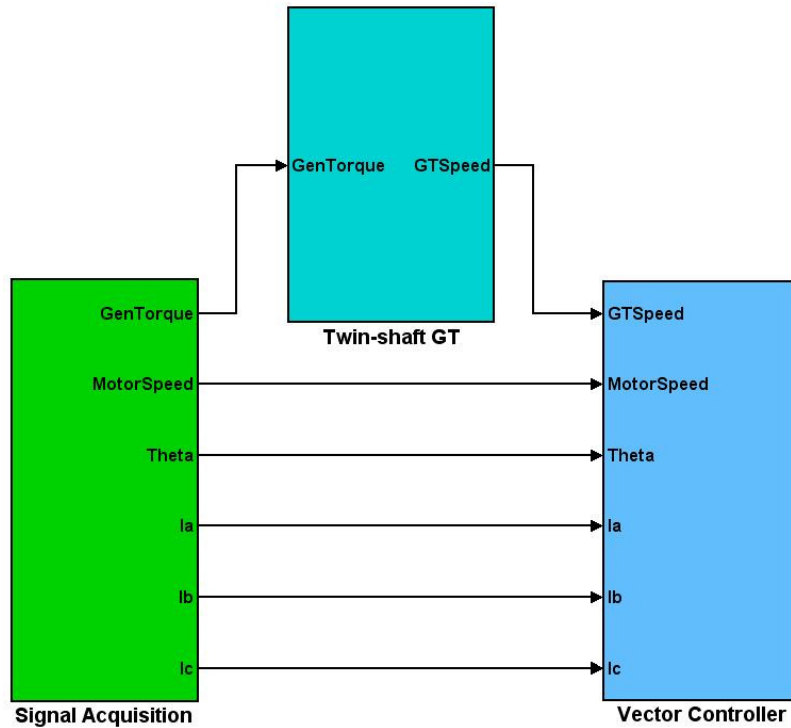
Figure 5.4: Real-time simulation model of the aeroderivative engine emulation system

5.2 Real-Time Simulation Model

The real-time simulation model used in the HIL simulation of the aeroderivative engine emulation system is composed of the aeroderivative twin-shaft gas turbine engine model, the synchronous motor vector controller scheme and signal acquisition blocks for speed, position and current sensing, as shown in Figure 5.4.

5.2.1 Real-Time Aeroderivative Twin-Shaft Engine Model (Engine Model 2)

The reference aeroderivative twin-shaft engine model (Engine Model 2) used in this experimental setup is based on [34], [53], and it is capable of running in real-time. A block diagram representation of the engine model together with its control and fuel systems is shown in Figure 5.5.
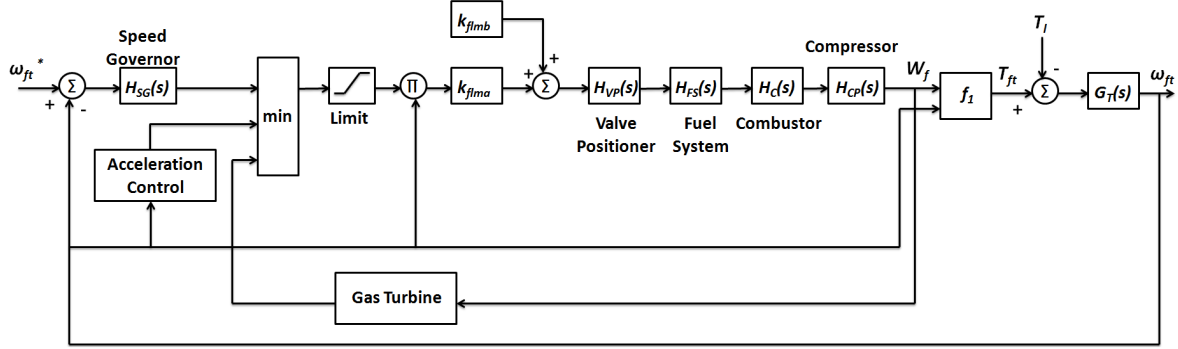
Figure 5.5: Schematic of linearized twin-shaft engine model

Similar to [53], the control system in this engine model includes speed control, acceleration control, and upper and lower fuel limits. This model is suitable for use in transient power system analysis since it describes the dynamics of turbine rotors and various transport delays associated with the compressor discharge volume, combustion reaction, etc. The main components such as the speed governor, valve positioner, fuel system, combustor, compressor, free turbine and gas turbine are described by their transfer function approximations.

The simplified mathematical representations for each block of the system are given in Equation 5-1, and the model parameters are described in Table 5.1. In Equation 5-1, H_{SG}, represents the free turbine governor transfer function, which is based on a proportional-integral controller; H_{VP} defines the characteristics of the fuel gas control system; H_{FS} represents the volumetric time constant associated with the downstream piping and fuel gas distribution manifold; H_C and H_{CP} represent the transport delay associated with the combustion reaction and the compressor discharge volume [53], respectively; $G_T(s)$ describes the rotor dynamics of the free turbine, in which J_T accounts for the inertia of the free turbine and generator, and B_T accounts for the damping coefficient of the free turbine and generator. The output of $G_T(s)$ is ω_{ft}, which is used as a reference for the synchronous motor drive controller.

68

$$H_{SG}(s) = \frac{K_{pft}s + K_{ift}}{s}$$

$$H_{VP}(s) = \frac{(a/c)}{1+(b/c)s}$$

$$H_{FS}(s) = \frac{1}{1+\tau_{FS}s}$$

$$H_C(s) = e^{-sT_c}$$

$$H_{CP}(s) = \frac{1}{1+\tau_{CP}s}$$

$$f_1(W_F, \omega_{ft}) = \frac{1}{k_{flmb}}\left[(W_F - k_{flma}) + 0.5(1 - \omega_{ft})\right]$$

$$G_T(s) = \frac{1}{J_T s + B_T}$$

Equation 5-1

Table 5.1: Aeroderivative twin-shaft engine model parameters

Symbol	Quantity	Value
a	Valve positioner constant	1 pu
b	Valve positioner constant	0.05 pu
c	Valve positioner constant	1 pu
k_{flma}	No-load fuel parameter	0.2 pu
k_{flmb}	No-load fuel parameter	0.8 pu (1- k_{flma})
T_c	Combustor delay time	0.01 s
K_{pft}	Speed governor proportional constant	1 pu
K_{ift}	Speed governor integral constant	2 pu/s
τ_{FS}	Fuel system time constant	0.4 s
τ_{CP}	Compressor discharge volume time constant	0.1 s

The engine model is implemented in Simulink using per unit values. The gas and free turbine speed controllers are implemented in digital form using the Simulink discrete PID block. The Simulink implementation of the free turbine rotor dynamics block is shown in Figure 5.6. The free turbine speed, ω_{ft}, is computed in Equation 5-2 by using as inputs the free turbine torque, T_{ft}, which is calculated in the engine model, and the generator torque, T_{Gen}, which is obtained from the actual DC generator.

$$\omega_{ft} = \frac{1}{2(H_{ft}+H_{Gen})}\frac{T_s}{z-1}\left(T_{ft}-T_{Gen}-\left(B_{ft}+B_{Gen}\right)\cdot\omega_{ft}\right)$$

Equation 5-2
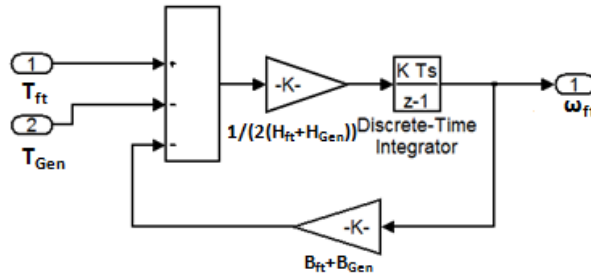
Figure 5.6: Implementation of free turbine rotor dynamics in Simulink

5.2.2 Vector Control Scheme

Figure 5.7 shows the Simulink implementation of the synchronous motor vector control scheme, which includes a speed and an internal current loop. The magnetizing reference current, i_{mref}, is set to zero in order to ensure decoupling of torque and flux. This synchronous motor vector control scheme does not include a flux or field controller as presented in Chapter 4 due to lack of a complete set of machine parameters and also for simplicity. Therefore, flux weakening operation is not tested. The synchronous motor field is set at a constant DC voltage as is also the case in reference [54].

70
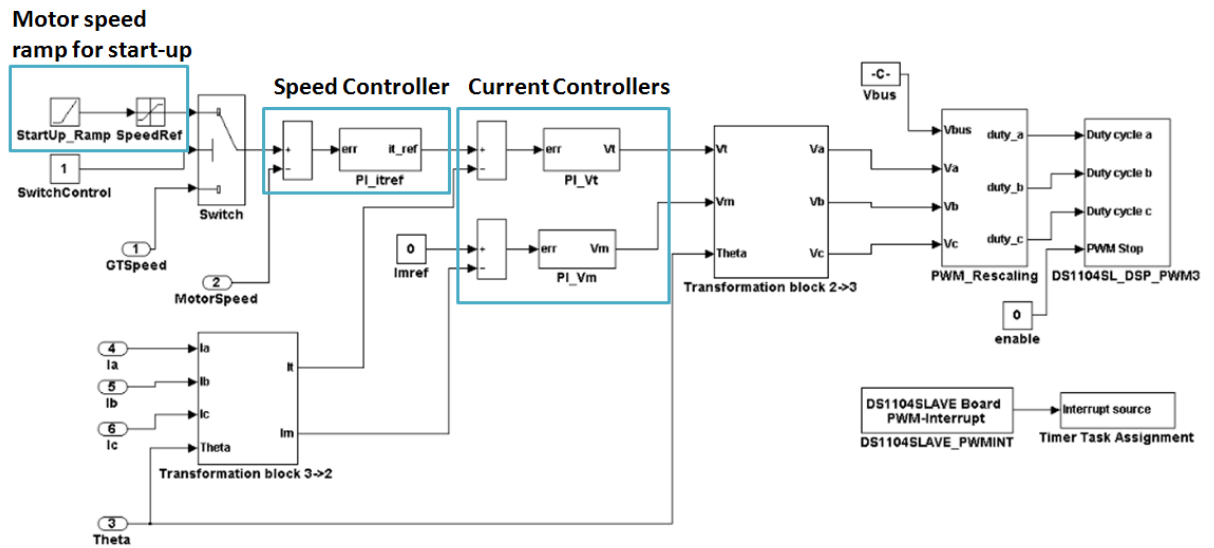
Figure 5.7: Schematic of synchronous motor vector controller

5.2.3 Signal Acquisition

5.2.3.1 Speed and Position Sensing

The motor speed is detected by using the US Digital speed encoder E3-2048-625-I-H-T-3

and the transmissive optical encoder module HEDS-9040-TOO. The HEDS module consists of a

lensed LED source and a monolithic detector IC. The HEDS module provides digital quadrature

outputs, channel A and channel B, and the Index [55]. The motor speed is detected by calculating

the frequency of channel A and B. The phase relationship between channel A and B determines

if the motor is turning in either forward or reverse direction. The position is obtained from the

Index signal.
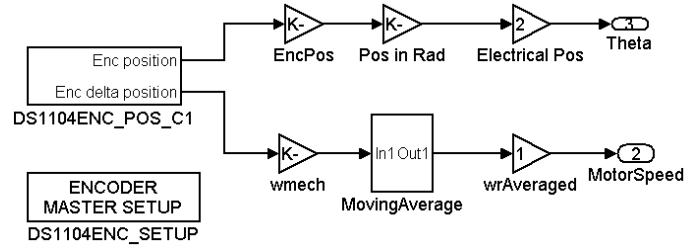
Figure 5.8: Speed measurement

Figure 5.8 shows the acquisition of speed and position in Simulink. Speed is measured using the DS1104ENC POS C1 block. This dSPACE library block provides access to the first encoder interface input channel. The gain value presented in Equation 5-3 is used to obtain the radian angle from the *Enc delta position* output signal of the DS1104ENC POS C1 block .

$$\frac{2\pi}{encoder\_lines} = \frac{2\pi}{2047}$$ **Equation 5-3**

In order to obtain the speed in rad/s, the radian angle has to be divided by the sampling time as expressed in Equation 5-4. A moving average filter is used to filter the speed signal.

$$\omega = \frac{\Delta\theta}{t_{k+1} - t_k} = \frac{\Delta\theta}{T_s}$$ **Equation 5-4**

5.2.4 Current Sensing

The two line output currents of the inverter, phases A and B, are measured by LEM sensors. The C phase current is calculated by using the relationship $i_a+i_b+i_c=0$. The measurement of current using ADC dSPACE library blocks is shown in Figure 5.9.
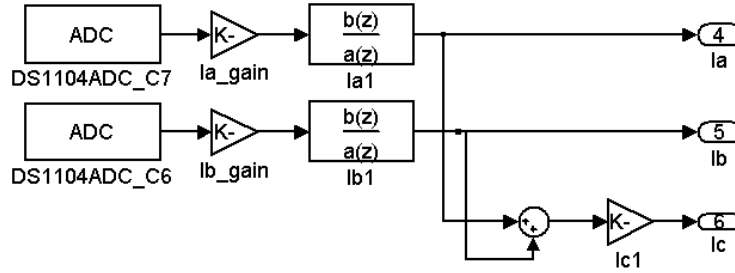
Figure 5.9: Current measurement

Two digital Butterworth low-pass filters with cutoff frequency of 500Hz are included, in order to remove high frequency noise signals in the measured A and B line currents.

5.2.5 Generator Torque Signal Acquisition

The generator torque, T_{Gen}, is estimated by measuring the armature DC current, i_a, of the DC generator and using Equation 5-5. The parameter, K_T, is the torque constant of the DC generator. Appendix C describes the estimation of K_T.

$$T_{Gen} = K_T i_a \qquad\qquad \textbf{Equation 5-5}$$

5.3 Speed Controller Design

Equation 5-6 describes the rotor dynamics transfer function of the synchronous motor connected to the DC generator in the benchtop-scale experimental setup. The parameter J accounts for the inertia of the synchronous motor and generator, and B accounts for the damping coefficient of the motor and generator.

$$G_P(s) = \frac{1}{Js + B} \qquad\qquad \textbf{Equation 5-6}$$

Figure 5.10 shows a block diagram representation of the synchronous motor control design. In this figure, K_e refers to the motor torque constant. The speed controller, $G_C(s)$, consists of a PI controller as defined by Equation 5-7. The parameters K_P and K_I are calculated using the frequency tuning method presented in Chapter 4.
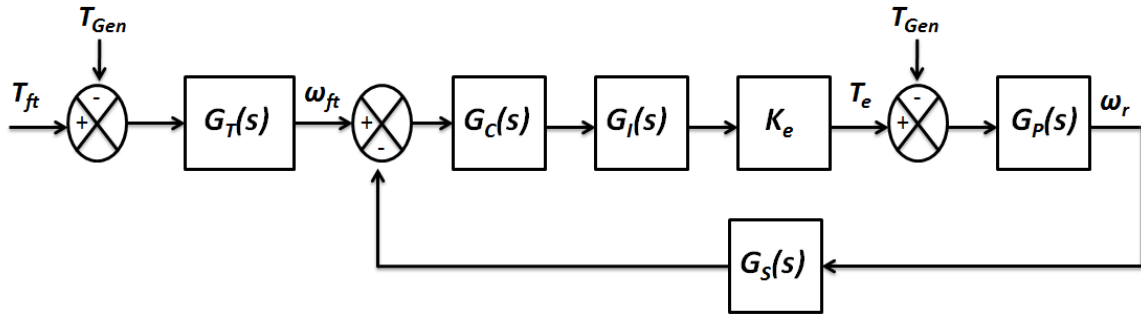
Figure 5.10: Block diagram of speed controller

$$G_C(s) = K_P + \frac{K_I}{s}$$

Equation 5-7

The transfer function $G_I(s)$ accounts for the current controller delay, τ_i, and it is given by Equation 5-8.

$$G_I(s) = \frac{1}{\tau_i s + 1}$$

Equation 5-8

, where, $\tau_i = L_q/K_{Pi}$. The parameter K_{Pi} is the proportional constant of the PI current controller. The transfer function $G_S(s)$ accounts for the sampling delay, τ_s, as expressed in Equation 5-9.

$$G_S(s) = \frac{1}{\tau_s s + 1}$$

<div align="right">**Equation 5-9**</div>

For simplification, $G_I(s)$ and $G_S(s)$ are combined in a single block $G_D(s)$ as given by Equation 5-10.

$$G_D(s) = \frac{1}{\tau_\alpha s + 1}$$

<div align="right">**Equation 5-10**</div>

, where, $\tau_\alpha = \tau_i + \tau_s$. The open loop system can be written in the frequency domain as shown in Equation (37).

$$G_o(j\omega) = G_C(j\omega)G_D(j\omega)K_e G_P(j\omega)$$

<div align="right">**Equation 5-11**</div>

The controller is designed by specifying the desired control bandwidth, ω_{bw}, and phase margin, φ_m, of the closed-loop system. By using Equations 4-7 and 5-11, the gains K_P and K_I are derived as shown in Equation 5-12.

$$K_P = \frac{\cos(-\pi + \varphi_m - \varphi_{bm})}{|G_D(j\omega)K_e G_P(j\omega)|}$$

$$K_I = \frac{-\omega_{bw}\sin(-\pi + \varphi_m - \varphi_{bm})}{|G_D(j\omega)K_e G_P(j\omega)|}$$

<div align="right">**Equation 5-12**</div>

, where $|G_D(j\omega)K_e G_P(j\omega)|$ is given by Equation 5-13 in terms of J and B.

$$\left| G_D(j\omega)K_e G_P(j\omega) \right| = \frac{\dfrac{K_e}{B}\sqrt{1+\omega_{bw}{}^2\left(\left(\dfrac{J}{B}\right)^2\left(1+\dfrac{J}{B}\tau_\alpha\omega_{bw}{}^2\right)+\tau_\alpha^2\right)}}{\left(1-\dfrac{J}{B}\tau_\alpha\omega_{bw}\right)^2+\left(\left(\dfrac{J}{B}+\tau_\alpha\right)\omega_{bw}\right)^2}$$

Equation 5-13

It can be seen from Equations 5-12 and 5-13 that the feedback controller is tuned according to the inertia of the emulating motor and it can be designed for different inertia values of the emulating motor.

Next, the continuous controller is converted to digital form by using a forward Euler approximation, which results in $G_C(z)$ as expressed in Equation 5-14.

$$G_C(z) = K_P + \frac{K_I T_s}{z-1}$$

Equation 5-14

At the mega-watt power level, the inertia of the engine is significantly lower than that of a similarly rated synchronous motor. Thus, the motor will require a large control effort that may not be met by the emulating motor due to its current and torque limitations. Therefore, it is of interest to explore how the accuracy of the engine emulation system depends on motor inertia.

The experimental results presented in Section 5.4 consider three cases: Case 1, when the inertia constant of the emulating motor is lower than that of the engine, Case 2, when inertial loading is added to the motor shaft so that its inertia constant is approximately equal to that of the engine, and Case 3, when further inertial loading is added so that the emulating motor inertia constant is larger than that of the engine.

The closed-loop transfer function of the speed loop is given in Equation 5-15 assuming τ_α is small so that $G_D(s) \approx 1$.

$$G_{CL}(s) = \frac{(K_P / K_I)s + 1}{\left(\dfrac{J}{K_e K_I}\right)s^2 + \left(\dfrac{(B / K_e) + K_P}{K_I}\right)s + 1}$$

Equation 5-15

The corner frequency, ω_{CL}, of $G_{CL}(s)$ is given by Equation 5-16.

$$\omega_{CL} = \sqrt{\frac{K_e K_I}{J}}$$

Equation 5-16

Therefore, the closed-loop system bandwidth is limited by K_I and J. This equation allows understanding the effect of inertia with respect to the bandwidth of a motor drive system. With K_I constant, the bandwidth of a system is lower when the inertia increases. The bandwidth of $G_T(s)$ is determined by $\omega_{ft} = B_T / J_T$. In Case 1 (low inertia case), $J < J_T$ and this implies that $\omega_{ft} < \omega_{CL}$. Therefore, for a given K_I that maintains system stability the controlled emulating motor is able to emulate the engine model over its full bandwidth. However, in Case 3 (high inertia case), $J > J_T$ and this implies that $\omega_{ft} > \omega_{CL}$. Therefore, for a given K_I that maintains system stability the motor can emulate the engine model only over a limited bandwidth. This limitation is imposed by the saturation of the motor speed controller which protects the motor drive from exceeding its physical constraints.

5.3.1 Antiwind-Up Scheme

An antiwind-up scheme limits the integrator output within a certain range, in order to prevent the unbounded increase of the integrator output value. Figure 5.11 shows the implementation of the digital PI controller including its antiwind-up scheme, which is used in the vector controller. The integration action works as long as there is a zero difference between the output of the PI controller (input to the saturation block) and the output of the saturation block. When the difference between the output of the PI controller and the output of the saturation block is a nonzero value, the relational operator outputs a zero value which causes the integrator to hold its last value.
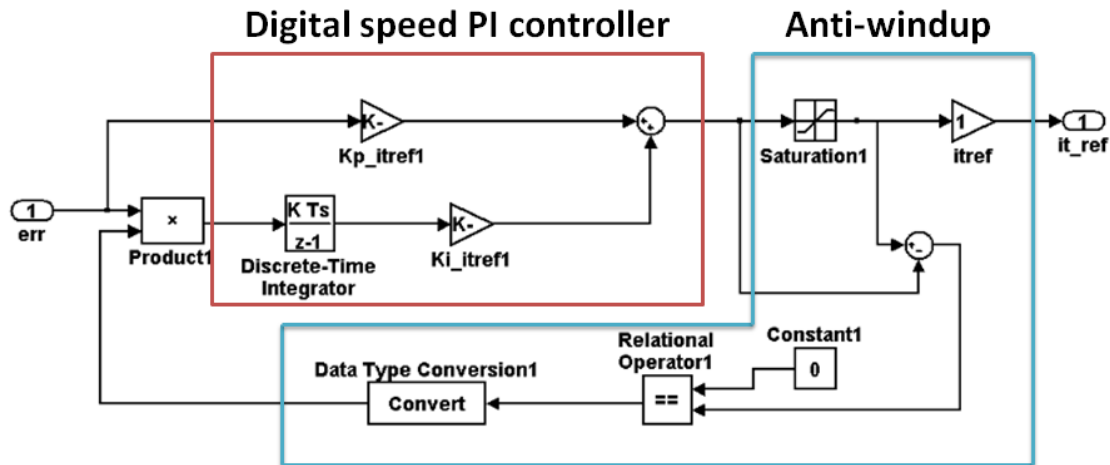
Figure 5.11: Implementation of the speed controller and its anti-windup scheme in Simulink

5.4 Experimental Results of Aeroderivative Engine Emulation

Initially, experimental results are obtained by performing four dynamic tests, which show the speed tracking performance of the aeroderivative engine emulation system in Cases 1 (low inertia case), 2 (equal inertia case) and 3 (high inertia case). The same speed controller design is used in all cases. Then, the effect of varying the speed controller crossover frequency in the high inertia case is analyzed. Tables 5.2, 5.3 and 5.4 indicate the specifications of the synchronous

78

emulating motor, the DC generator and the inertial disks. The estimation of machine parameters

is presented in Appendix C.

Table 5.2: Synchronous machine specifications

Speed/ Frequency	1800 rpm/60 Hz
Voltage	120 V-3 Phase
Power	250 W
Poles	4
Field excitation current	1.6 A
Estimated inertia	0.0094 kg·m^2
Estimated damping coefficient	0.0005 N·s/m
Estimated torque constant	0.26
Estimated stator inductance	396.5 mH
Estimated stator resistance	4.65 Ω

Table 5.3: DC machine specifications

Speed	1800 rpm
Voltage	150 V
Power	250 W
Field excitation voltage	120 V
Field excitation current	1.6 A
Estimated inertia	0.0073 kg·m^2
Estimated damping coefficient	0.0015 N·s/m
Estimated torque constant	0.6632

Table 5.4: Inertial loading specifications

Shaft estimated inertia	0.0143 kg·m^2
Shaft estimated damping coefficient	0.0126 N·s/m
Disk estimated inertia	0.0169 kg·m^2

5.4.1 Dynamic Testing of Engine Emulation

Two dynamic tests are performed in this section: Test 1 consists of 5 % step changes in reference free turbine governor speed, and Test 2 consists of small step changes in generator electrical loading. Test 1 is performed in order to analyze the engine emulation system tracking performance during operation of the engine below rated speed, as well as during acceleration and deceleration caused by variations of the engine fuel input. Test 2 is performed in order to analyze the engine emulation system tracking performance during acceleration and deceleration of the engine caused by changes in torque load. Each test is presented for Cases 1, 2 and 3. Table 5.5 includes the values of inertia constant of the engine model and of the emulating motor in the three analyzed cases.

Table 5.5: Engine inertia constant and emulating motor inertia constant for Cases 1, 2 and 3

H_{Engine} [s]	Estimated $H_{EngineEmulation}$ [s]		
	Case 1: Low inertia case	Case 2: Equal inertia case (adding 3 inertial disks)	Case 3: High inertia case (adding 6 inertial disks)
4	0.6680	4.0862	8.8902

The speed controller design in the three analyzed cases is the same for Tests 1 and 2. The speed PI parameters, K_P and K_I, are computed according to the plant model based on Case 3 (the high inertia case), in which the total inertia is equal to the emulating motor inertia, the DC generator inertia and the combined inertia of six inertial disks, and the total damping coefficient is equal to the sum of the damping coefficients of each of these elements. Experimental results are obtained by designing the speed controller with $\omega_c=0.8\ rad/s$ and $\varphi_m=60°$, which yields $K_P=0.3082$ and $K_I=0.1889$. Experimental results are obtained by designing the current PI controllers with $\omega_{ci}=80\ rad/s$ and $\varphi_{mi}=70°$, which yields $K_{Pi}=28.2167$ and $K_{Ii}=1.2175\cdot10^3$. The

maximum limit of the speed controller saturation is set to the trip value of the motor protection system which is 2.4 A of peak current.

5.4.1.1 Test 1: 5% Step Changes in Reference Free Turbine Governor Speed

Figures 5.12, 5.13 and 5.14 show the speed of the emulation system compared to the speed of the engine when consecutive 5 % step decreases and increases in ω_{ft}^{*} occur below nominal speed for Cases 1, 2 and 3, respectively. In Case 1 (low inertia case), the speed tracking performance of the emulating motor is excellent as shown in terms of the speed tracking percentage error in Figure 5.15 a). In Case 3 (high inertia case), the speed response of the motor lags the reference speed signal by 0.6 s during the step decreases and by 0.4 s during the step increases. In Figure 5.15 a), Case 3 presents a larger tracking error than Cases 1 and 2. In Case 2 (equal inertia case), the motor presents a smaller speed tracking delay than Case 3. In Case 2, the speed response of the motor lags the reference speed signal by 0.28 s during the step decreases and 0.16 s during the step increases. Figure 5.15 b) shows the control effort during this test for Cases 1, 2 and 3. The control effort is the output signal of the speed controller representing the torque producing component of the emulating motor armature current. In Figure 5.15 b) it can be seen that Case 3 demands a larger control effort compared to Cases 1 and 2, and it reaches a maximum value of 2 A during the last 5 % step increase. Figure 5.15 d) shows the engine fuel input, which is restricted to maximum and minimum fuel supply values and represents the engine control effort. The generator torque variation during this test is shown in Figure 5.15 c).
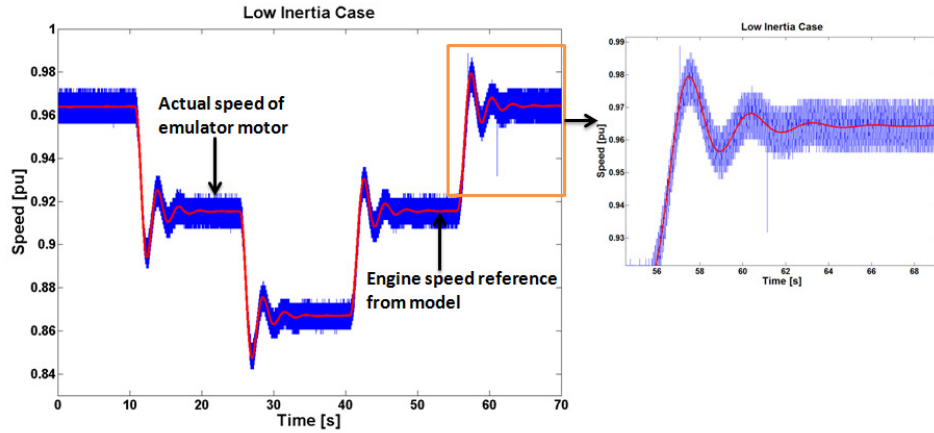
Figure 5.12: Low inertia case: Engine model and emulation system speed comparison during

5 % step decreases and increases in reference free turbine governor speed
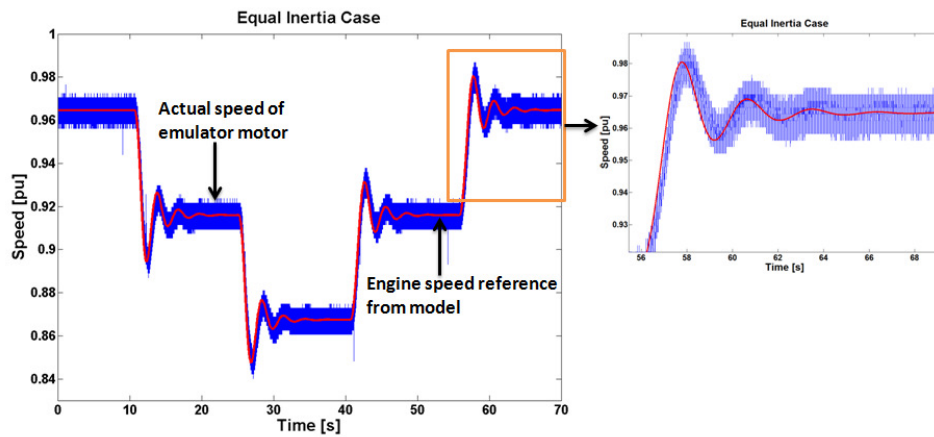
Figure 5.13: Equal inertia case: Engine model and emulation system speed comparison

during 5 % step decreases and increases in reference free turbine governor speed
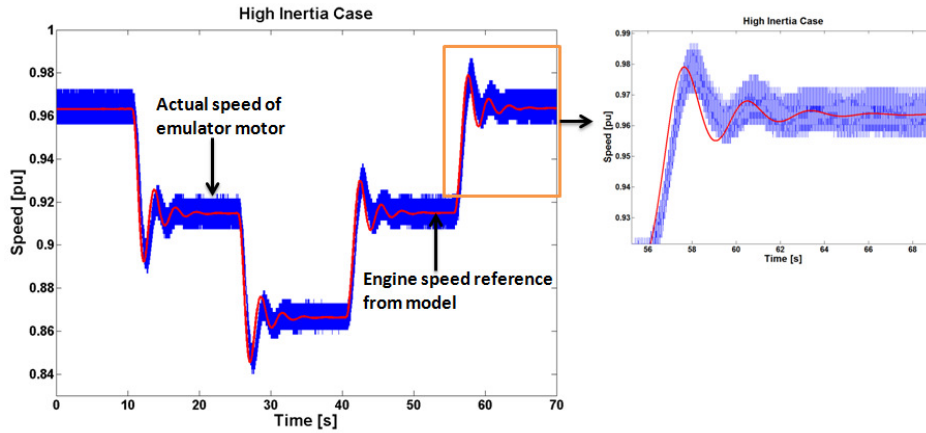
Figure 5.14: High inertia case: Engine model and emulation system speed comparison

during 5 % step decreases and increases in reference free turbine governor speed
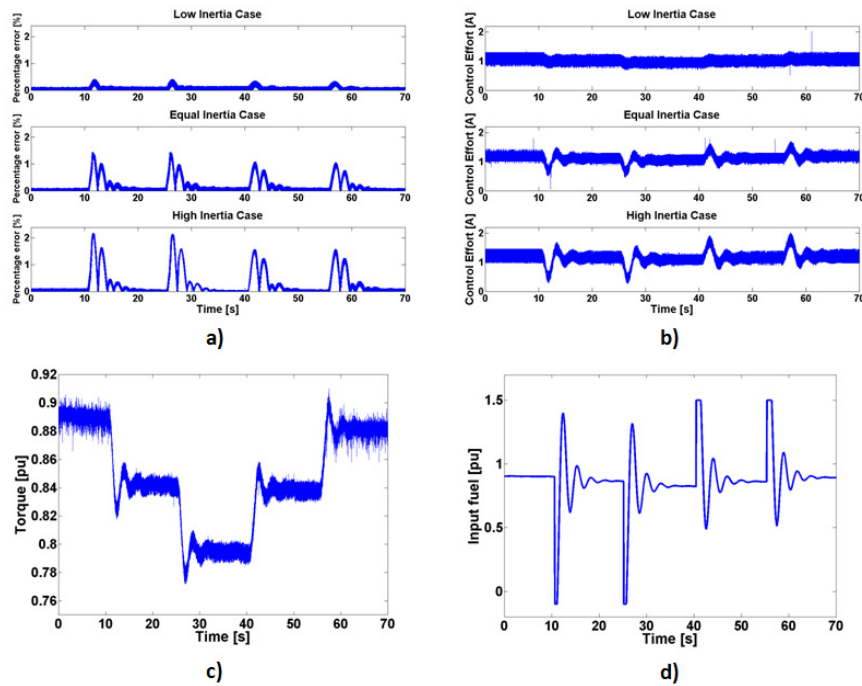
Figure 5.15: 5 % step decreases and increases in reference free turbine governor speed: a)

Percentage Error vs Time, b) Control Effort vs Time, c) Torque vs Time, d) Input Fuel vs

Time

5.4.1.2 Test 2: Small Step Load Changes in Electrical Load

Experimental results in Figures 5.16 and 5.18 show the speed tracking performance of the engine emulation system when small step changes in generator electrical loading are applied. In Figure 5.16, a torque step from 0.9 to 0.68 pu is applied at t=10 s, and then a torque step from 0.68 to 0.9 pu follows at t=25 s. It can be seen that the engine emulation system can track the speed of the engine model with great accuracy in Case 1. A delay between the engine emulation system and engine speed is noticeable as the inertia of the engine emulation system is increased. During the torque step decrease, the motor lags the engine speed by 0.12 s and 0.31 s in Cases 2 and 3, respectively. During the torque step increase, the motor lags the engine speed by 0.15 s and 0.32 s in Cases 2 and 3, respectively. Figure 5.17 shows the speed tracking percentage error, control effort, engine fuel input and generator torque, respectively. Figure 5.17 c) shows that a reduction in generator torque initially causes motor speed acceleration. Therefore, Figure 5.17 b) shows that Case 3 requires a larger control effort so that the motor can accelerate and track the engine speed. As expected, in the high inertia case the requirement for a larger control effort during acceleration affects the accuracy of the engine emulation system.

Figure 5.18 shows the case when a torque step from 0.9 to 1.1 pu is applied at t=10 s, and then a torque step from 1.1 to 0.9 pu follows at t=25 s. As in the latter case, in Figure 5.18 a dynamic lag between the engine emulation system and engine speed can be seen as the inertia of the engine emulation system is increased. During the torque step increase, the motor lags the engine speed by 0.18 s and 0.35 s in Cases 2 and 3, respectively. During the torque step decrease, the motor lags the engine speed by 0.19 s and 0.31 s in Cases 2 and 3, respectively. Figure 5.19 shows the speed tracking percentage error, control effort, engine fuel input and generator torque, respectively. Figure 5.19 c) shows that when the initial torque step load increase is applied it

causes the speed to decelerate. At this instant, it can be seen in Figure 5.19 b) that the control

effort in Case 3 decreases much more than in Cases 1 and 2.
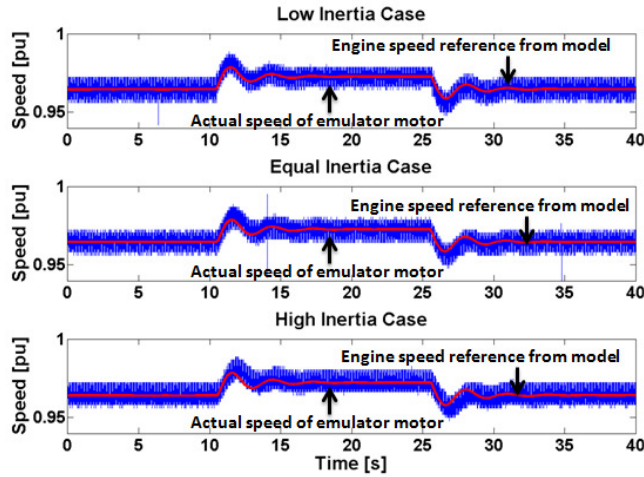
Figure 5.16: Engine model and emulation system speed comparison during small step

changes (first 0.9 to 0.68, second 0.68 to 0.9 pu) of generator torque
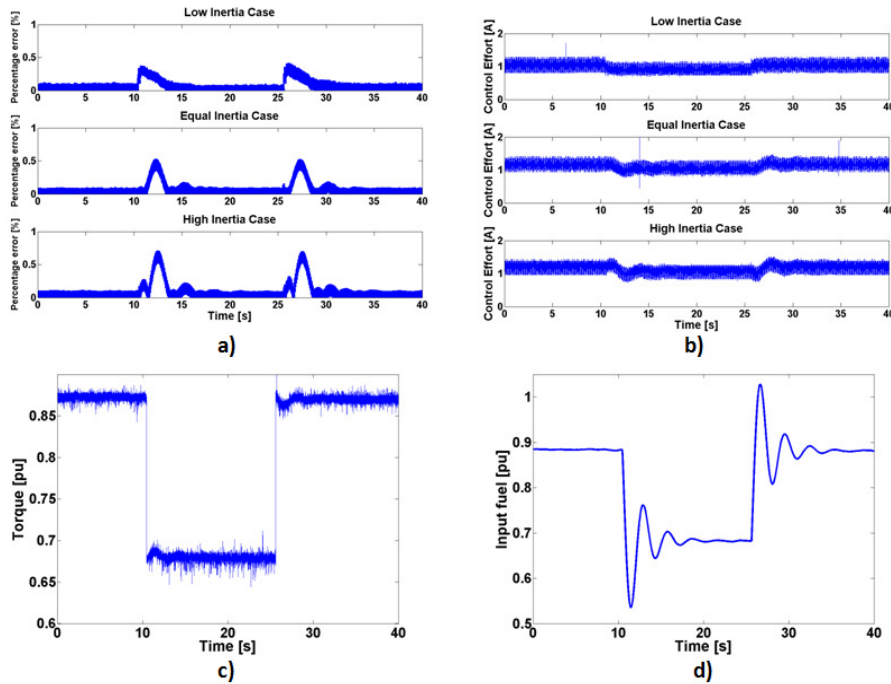
Figure 5.17: Small step changes (first 0.9 to 0.68, second 0.68 to 0.9 pu): a) Percentage Error

vs Time, b) Control Effort vs Time, c) Torque vs Time, d) Input Fuel vs Time

85
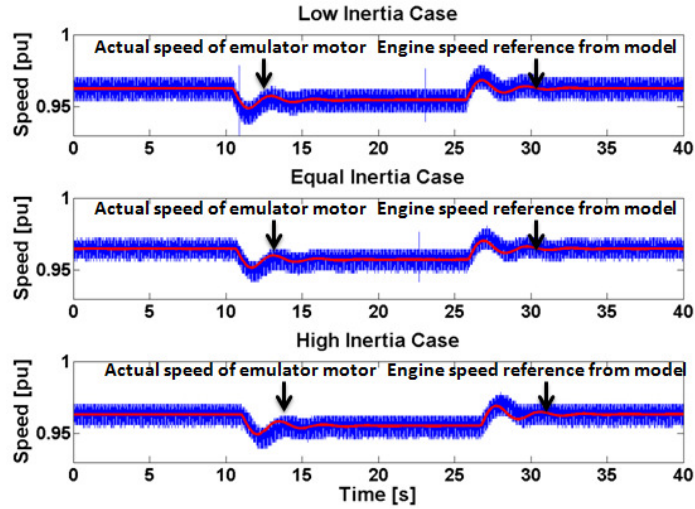
Figure 5.18: Engine model and emulation system speed comparison during small step changes (first 0.9 to 1.1 pu, second 1.1 to 0.9 pu) of generator torque
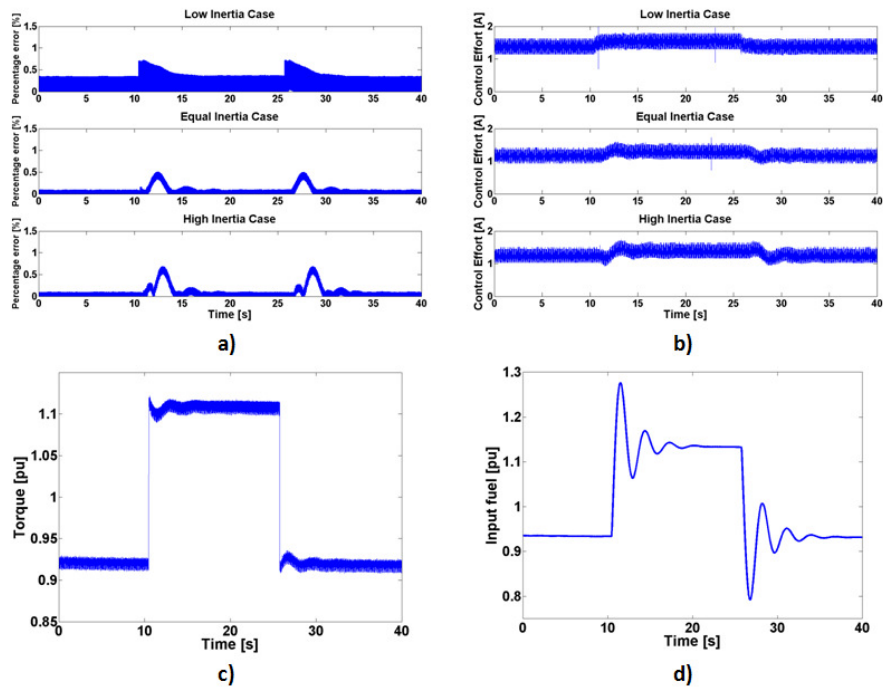
Figure 5.19: Small step changes (first 0.9 to 1.1 pu, second 1.1 to 0.9 pu): a) Percentage Error vs Time, b) Control Effort vs Time, c) Torque vs Time, d) Input Fuel vs Time

5.4.2 Variation of Crossover Frequency in the High Inertia Case

This section shows the effect of varying the speed controller crossover frequency on the speed tracking performance of the engine emulation system, when the motor has a larger inertia than the engine model. For comparison purposes, the results of Figures 5.16 and 5.17 are shown again in Figure 5.20. In these figures, the speed tracking performance and control effort of the engine emulation system are shown during an initial torque step from 0.9 to 0.68 pu and then from 0.68 to 0.9 pu. In this test, the speed controller design is the one described in Section 5.4.1 and for further analysis it will be considered as the speed controller base design. As can be seen in Figure 5.20, the motor presents a small dynamic lag with respect to the engine speed when using the speed controller base design. The control effort is maintained below the saturation limit, which is 2.4 A.

Next, two different cases are analyzed: the low crossover frequency case and the large crossover frequency case. In the low crossover frequency case, the crossover frequency of the speed controller base design is reduced by a factor of 8, and in the large crossover frequency case the crossover frequency of the speed controller base design is increased by a factor of 12.5. Figure 5.21 shows the engine emulation system speed tracking performance and control effort for the low crossover frequency case. In this case, a torque step from 0.9 to 0.68pu at t=10s is initially applied and then a torque step from 0.68 to 0.9 pu follows at t=25 s. Since reducing the crossover frequency decreases the motor speed controller bandwidth, the tracking performance of the engine emulation system is very poor in this case.

Figure 5.22 shows the engine emulation system speed tracking performance and control effort for the large crossover frequency case. In Figure 5.22, the tracking performance of the engine emulation system improves significantly and the motor no longer lags the engine speed since the speed controller bandwidth is larger. However, it can be seen that the improvement in

tracking performance is at the expense of speed controller saturation. Therefore, it can be concluded that the speed tracking performance of the engine emulation system can be improved by using a faster speed controller design but this can force the system into saturation.
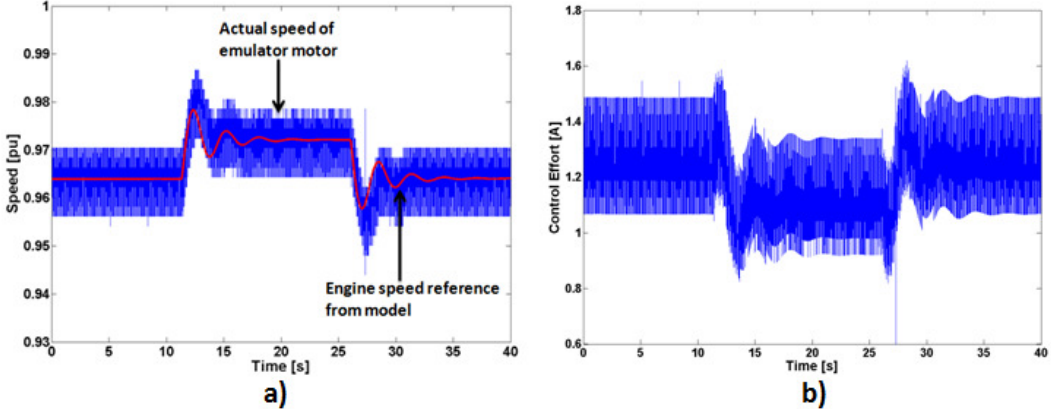
Figure 5.20: Base speed control design case during small step changes (first 0.9 to 0.68, second 0.68 to 0.9 pu) of generator torque: a) Engine model and emulation system speed comparison, b) Control Effort vs Time
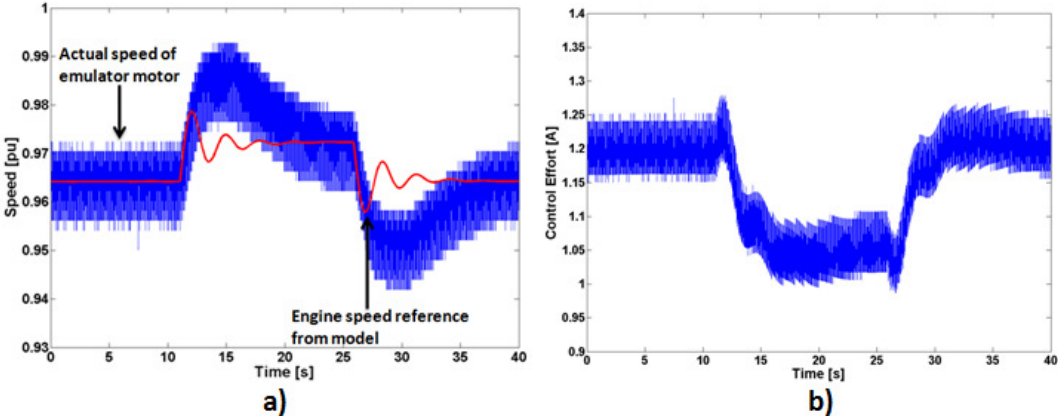
Figure 5.21: Low crossover frequency case during small step changes (first 0.9 to 0.68, second 0.68 to 0.9 pu) of generator torque: a) Engine model and emulation system speed comparison, b) Control Effort vs Time
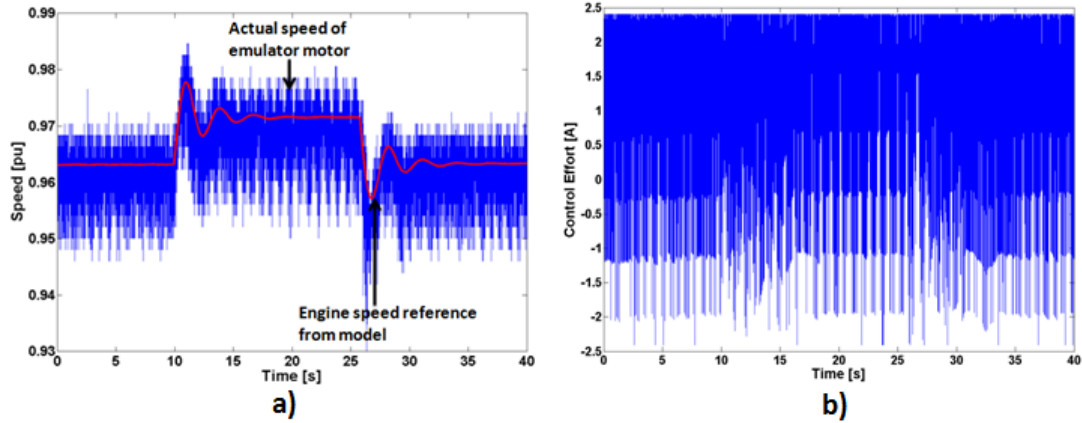
Figure 5.22: Large crossover frequency case during small step changes (first 0.9 to 0.68, second 0.68 to 0.9 pu) of generator torque: a) Engine model and emulation system speed comparison, b) Control Effort vs Time

5.5 Discussion and Chapter Summary

This chapter has presented the experimental emulation of an aeroderivative twin-shaft engine by using a vector controlled synchronous motor drive which tracks the speed of a real-time engine model as it drives an electric generator supplying power to steady-state and dynamic loads. The engine emulation method has been validated on a benchtop-scale HIL implementation. Furthermore, the inertia of the synchronous motor has been varied by adding inertial loading to its shaft in order to study the effect of emulating a prime mover with a higher inertia than the emulating motor. It has been shown mathematically that the bandwidth of the motor speed loop is limited by the inertia of the motor and that the feedback controller can be tuned according to the inertia of the emulating motor. Therefore, the feedback controller can be designed to accommodate motors having different inertias.

Experimental results have shown that the accuracy of the engine emulation system depends on the inertia difference between the engine and emulating motor. When the inertia of the emulating motor is lower than that of the engine (low inertia case), the speed controller can

89

be tuned so that accurate speed tracking performance with a percentage error of less than 1% is possible. This is because the motor can emulate the engine over its entire bandwidth.

However, speed tracking accuracy is lost when the inertia of the emulating motor is larger than that of the engine (high inertia case) as it is driven by the same speed controller design used in the low inertia case. In this case, the speed of the emulating motor presents a dynamic lag with respect to the engine model. This is because during speed acceleration and deceleration the high inertia case requires a larger control effort. The engine tracking performance in the high inertia case can be improved by increasing the controller bandwidth. However, increasing the controller bandwidth can force the system into saturation.

CHAPTER 6: LOW-POWER HIL SIMULATION OF AN AERODERIVATIVE TWIN-SHAFT GAS TURBINE ENGINE EMULATION SYSTEM

This chapter presents the implementation details of an aeroderivative twin-shaft engine emulation system, which is realized using a low-power HIL experimental setup. This engine emulation system is used to validate a method for selecting the appropriate AC electric motor and drive to emulate an aeroderivative engine, which is presented in Chapter 7, and a model-based analysis of an engine emulation system, which is presented in Chapter 8.

6.1 Concept of the Low-Power Engine Emulation System

Figure 6.1 shows the concept of the proposed engine emulation system, in which the performance of an aeroderivative twin-shaft engine is emulated by dynamically setting the speed reference of a vector controlled induction motor drive according to the performance predicted by a real-time model of the engine. This concept is similar to the one presented in Chapter 5. However, in this case the shaft torque is fed back to the engine model instead of the generator or load machine electrical torque. It can be seen in Figure 6.1, that the engine speed can be affected by variations in the speed reference of the free turbine governor, ω_{ft}^{*}, which determines the engine fuel demand, and the load torque, T_l. Therefore, the motor drive includes a speed tracking controller in order to minimize the error between the free turbine speed, ω_{ft}, and the motor rotor speed, ω_r, during variations in ω_{ft}^{*} and T_l.
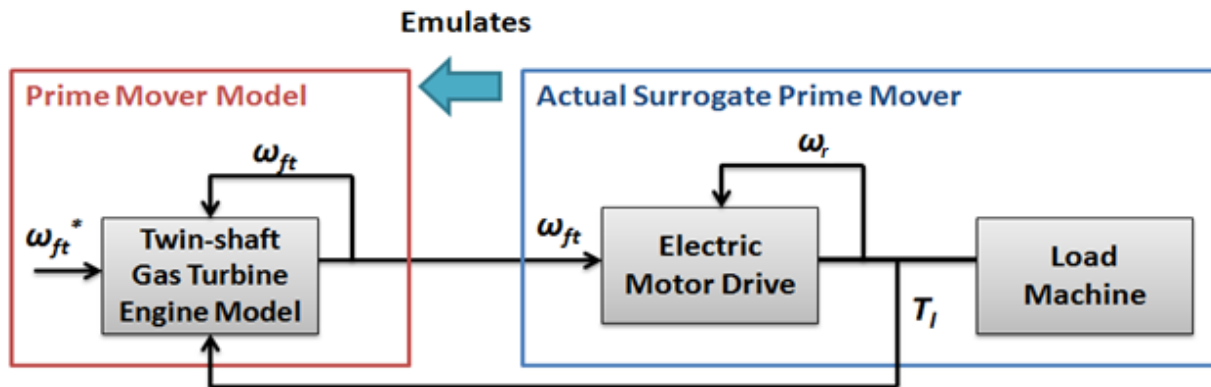
Figure 6.1: Concept of engine emulation system

6.2 Hardware-in-the-Loop Simulation of the Engine Emulation System

The engine emulation system is implemented in a HIL setup using two identical 15 kW induction machines on a common shaft available at the Center for Advanced Power Systems (CAPS) at Florida State University [56]. The HIL setup involves the use of a commercial drive from Alstom motor drives. One of the machines acts as emulating motor and the other one as the load machine that is tested in steady-state and dynamic conditions. The emulating motor operates in speed control mode so that the motor drive inverter outputs the appropriate voltage command according to a speed tracking control loop. The load machine operates in torque control mode.

The reference speed of the speed loop is provided by a real-time aeroderivative twin-shaft gas turbine engine model. In this configuration, the shaft torque is fed back to the real-time engine model so that the output speed signal of this model is computed as if the engine was really connected to the load machine. A vector controller is already incorporated in the drive system so that the real-time simulation consists only of the aeroderivative twin-shaft engine

model and interface blocks for the measured speed, torque and current signals. The specifications of the induction machines and drives can be found in Appendix D. A notational schematic of the low-power HIL setup is shown in Figure 6.2. The experimental setup of the engine emulation system is shown in Figure 6.3.
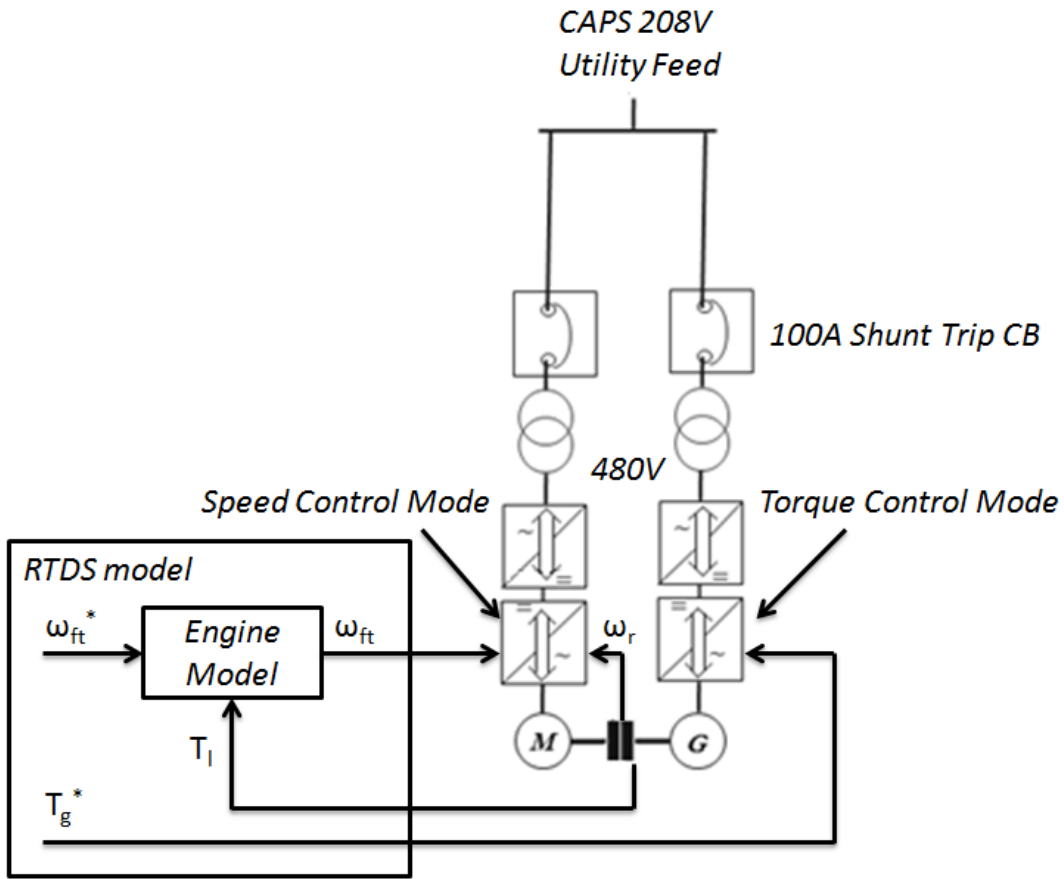
Figure 6.2: Schematic of the low-power HIL aeroderivative twin-shaft engine emulation system
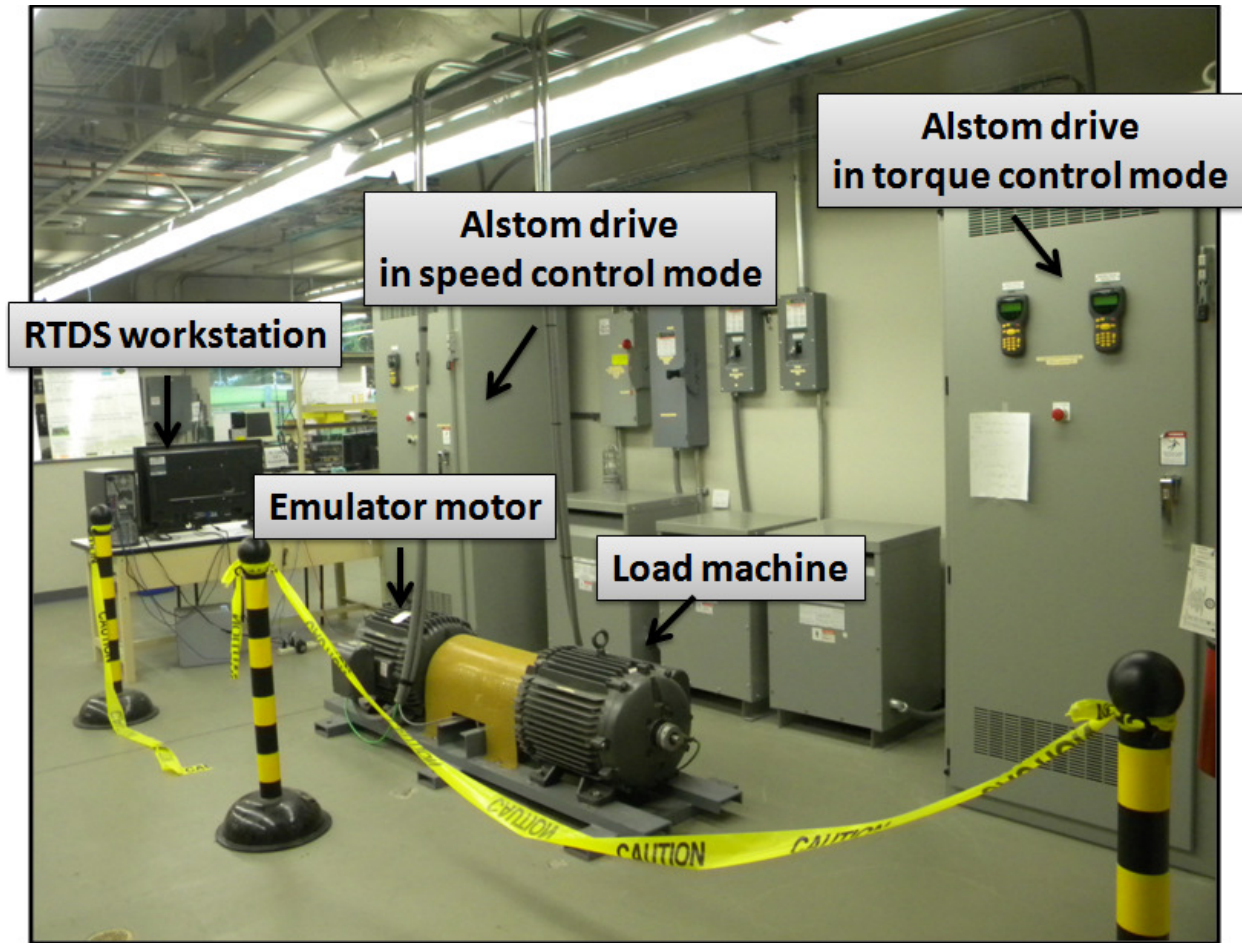
Figure 6.3: Experimental setup of the engine emulation system at CAPS

6.3 Real-Time Simulation Model

The real-time simulation is performed using the Real−Time Digital Simulator (RTDS), which consists of a special purpose computer designed to study electromagnetic transient phenomena in real−time, and it is composed of specially designed hardware and software. The RTDS software includes power system and control component models, and it employs nodal analysis as network solution technique. It also includes a graphical user interface, referred to as RSCAD, through which the user can design and analyze simulation cases [57].
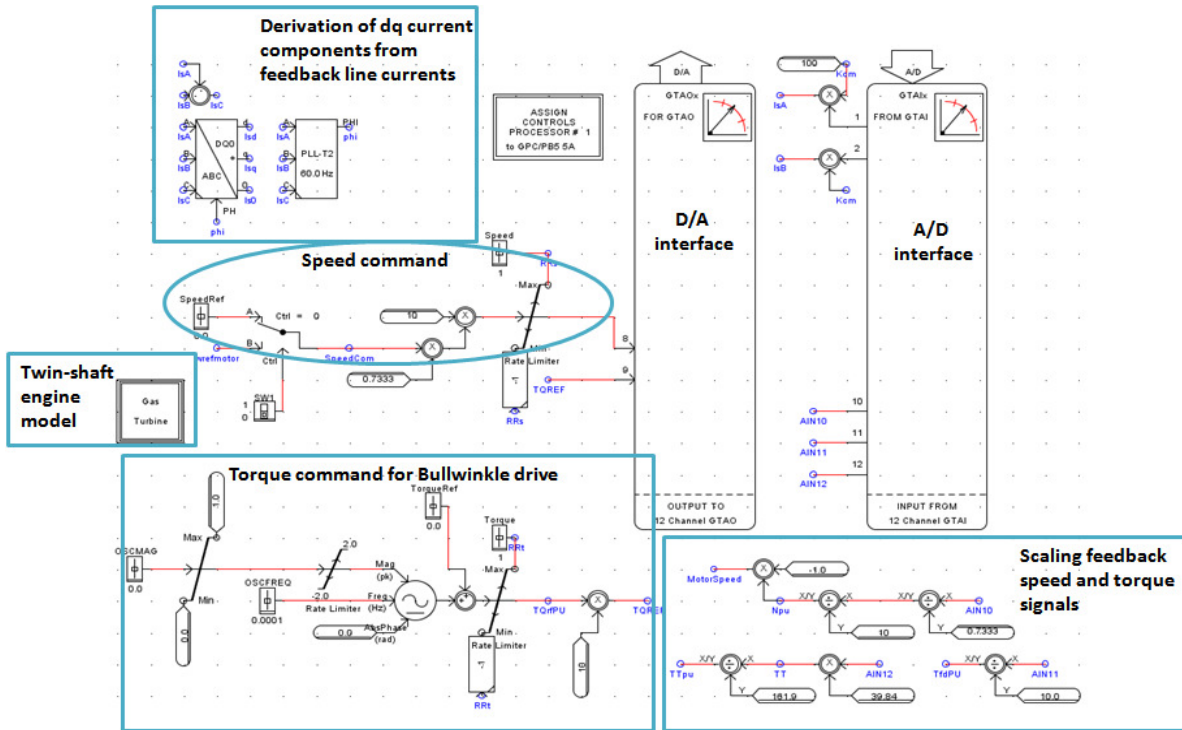
Figure 6.4: RTDS system model used in the engine emulation system

The aeroderivative engine emulation system presented in this chapter includes the aeroderivative twin-shaft gas turbine engine model (Engine Model 2) described in Chapter 5. However, in this case the engine model is implemented in RTDS. Figure 6.5 shows the real-time system model used in the engine emulation system. A D/A interface is used for commanding the speed reference to the emulating motor drive that is provided by the aeroderivative engine model. An A/D interface is used for obtaining the shaft torque transducer signal, the measured speed and the emulating motor armature currents. A PLL block and an *a-b-c/d-q-o* transformation block are used to derive the *dq* motor current components.

6.3.1 Motor Drive Control Loops

Figure 6.5 presents the schematic of the Alstom motor drive control loops involved in the computation of the motor torque demand, when the drive is set for vector control mode [58]. As can be seen, the torque demand can result from the sum of three control loops: the torque control

95

loop, the inertia compensation loop and the speed control loop. In our study, the emulating motor is controlled by enabling the speed loop, and disabling the torque and inertia compensation loops. The machine used as generator is controlled by enabling the torque control loop, and disabling the speed control and inertia compensation loops. The limits on the torque demand can also be specified by the user. However, the maximum allowable torque limit of the motor drive is 3 pu. The speed control loop contains a PID controller, and its parameters can be set by the user. The control tuning technique described in Chapter 4 is used to compute the PID controller parameters as K_p= *31.06 pu* and K_i=*274 pu/s*, so that the crossover frequency of the closed-loop system, ω_c, is 50 rad/s and the phase margin of the closed-loop system, φ_m, is 80°. The derivative term, K_d, is set to zero.

In Figure 6.6, it can be seen that the torque demand is fed to a vector control block that contains the current control loop. Only the bandwidth of the current controller can be specified by the user. In this study, it is set to 750 rad/s. The vector control block is also fed by the output of the temperature compensation blocks, the flux limit and the output of the motor model. The Alstom motor drive only requires the measurement of speed and position for vector control operation, so it is assumed that the output of the motor model calculates the motor current. The output of the vector control block is then fed to a PWM block to generate appropriate voltage commands for the inverter fed motor. The switching frequency of the inverter can also be set by the user. In this case, it is set to 2.5 kHz.

96
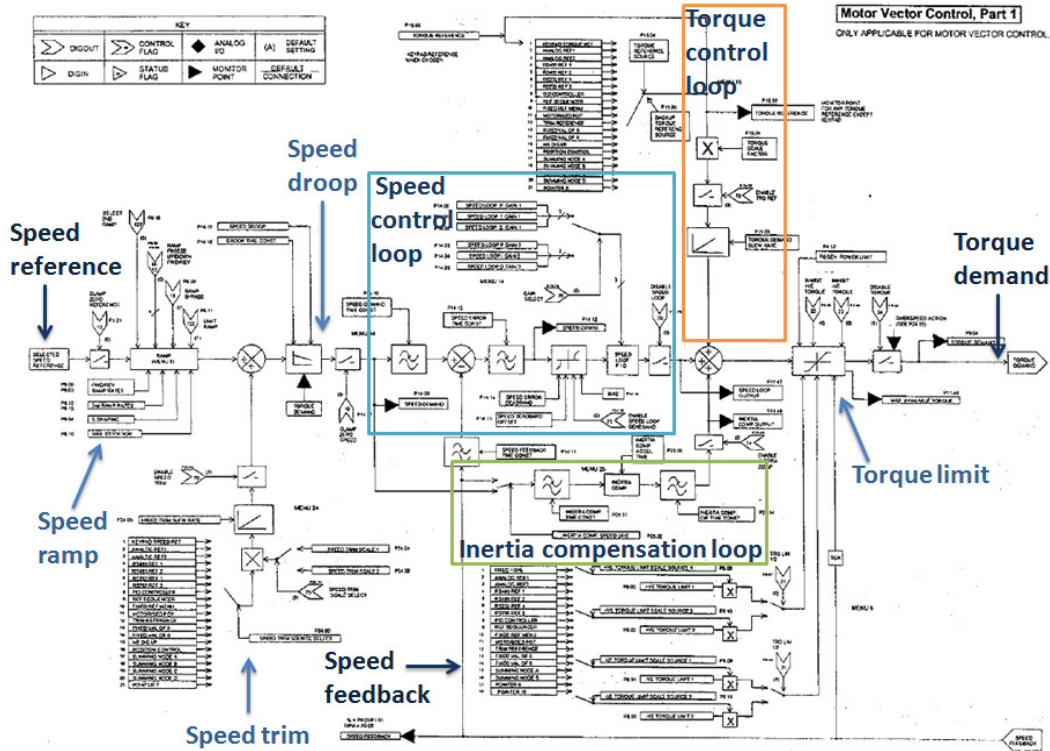
Figure 6.5: Alstom motor drive torque demand computation in vector control mode [58]
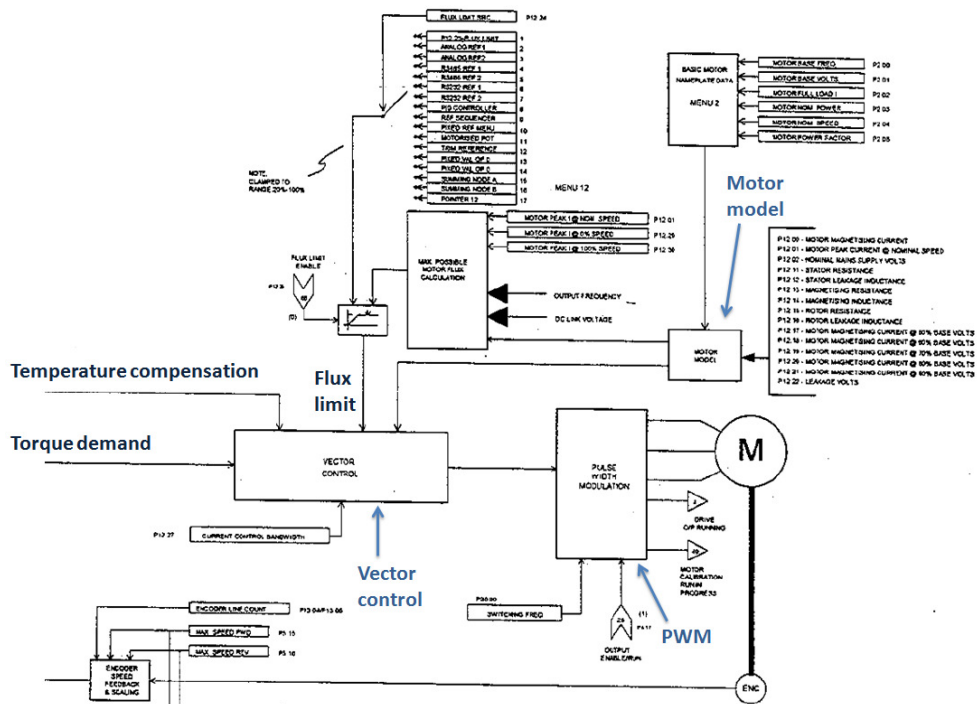
Figure 6.6: Alstom motor drive current control loop and generation of PWM voltage signal

commands [58]

6.3.2 Aeroderivative Twin-Shaft Engine Model in RTDS

As previously stated, the aeroderivative engine simulation model described in Chapter 5 is used in this study. The implementation of the free turbine rotor dynamics in RTDS is shown in Figure 6.7. The free turbine inertia constant is varied in the experimental studies in order to study the effect of emulating an engine with a larger or lower inertia than the emulating motor. As can be seen in Figure 6.7, a second-order Butterworth low-pass filter is also implemented in simulation to filter high-frequency components in the torque transducer signal.
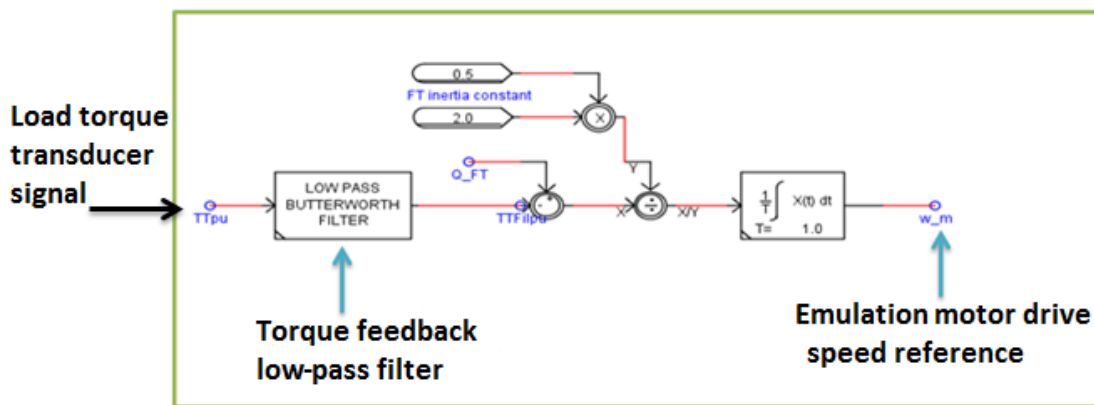
Figure 6.7: Implementation of free turbine rotor dynamics in RTDS

6.4 Procedure for Emulating an Aeroderivative Twin-Shaft Engine using an AC Electric Motor Drive

Figure 6.8 illustrates a procedure for designing an aeroderivative twin-shaft gas turbine engine emulation system. This procedure takes into account torque, power, and stability limitations that need to be considered when designing an engine emulation system for a specific aeroderivative twin-shaft engine – generator system that is already available. The first step involves the selection of the appropriate AC electric motor and drive for emulating an engine

[59]. This step depends on torque and power requirements that are described in Chapter 7. Once the motor and drive are selected, the speed tracking controller and the load torque low-pass filter are designed. Next, analysis of stability and inertia loading effects of the complete engine emulation system is performed. Chapter 8 presents a model-based analysis of an engine emulation system that allows examination of system stability and inertial loading effects. The methods presented in Chapters 7 and 8 are validated using the HIL setup described in this chapter.

```
┌─────────────────────────────────────────────────────────┐
│        Select the AC electric motor and variable speed drive        │
├─────────────────────────────────────────────────────────┤
│  1. Determine  the main supply voltage level and operating  │
│     frequency.                                              │
│  2. Determine  the speed range and load characteristics of  │
│     the engine-generator set.                               │
│  3. Select the emulation motor: Check the ability of the    │
│     motor to meet the speed and torque requirements         │
│     defined by the engine emulation system.                 │
│  4. Select the variable speed drive: Check the ability of the│
│     drive to produce the required current and power.        │
└─────────────────────────────────────────────────────────┘
```

```
┌─────────────────────────────────────────────────────────┐
│  Select the speed controller PI parameters, $K_p$ and $K_i$: Achieve │
│  satisfactory speed tracking performance while maintaining │
│                    system stability                        │
└─────────────────────────────────────────────────────────┘
```

```
┌─────────────────────────────────────────────────────────┐
│              Design load torque low-pass filter             │
└─────────────────────────────────────────────────────────┘
```

```
┌─────────────────────────────────────────────────────────┐
│          Check engine emulation system stability and        │
│                  inertia loading effects                    │
└─────────────────────────────────────────────────────────┘
```

Figure 6.8: Procedure for designing an aeroderivative twin-shaft engine emulation system

CHAPTER 7: SELECTION OF AN AC ELECTRIC MOTOR AND VARIABLE SPEED DRIVE FOR THE EMULATION OF AN AERODERIVATIVE TWIN-SHAFT ENGINE

This chapter presents a method for selecting the AC electric motor and variable speed drive that are used for emulating the steady-state, and transient loading and unloading dynamics of an aeroderivative twin-shaft gas turbine engine. Since an aeroderivative engine typically has a higher power-to-weight ratio than an AC motor of the same power rating, the torque limitations of the emulating motor can present challenges to the emulation during transient step loading conditions. Therefore, torque and power criteria need to be defined for selecting the appropriate AC motor and variable speed drive to emulate an engine. The torque criterion defined in this chapter depends on the inertia constant ratio between the emulating motor and free turbine, and on the size of the desired step loading that is to be tested on the generator. A design example based on the HIL setup presented in Chapter 6 is presented in order to demonstrate the applicability of the torque and power criteria.

7.1 Emulating Motor Nominal and Peak Torque Requirements

The torque and speed requirements for a motor driving a given load are expressed in terms of the continuous torque, peak torque and speed limits as expressed in Equations 7-3, 7-4 and 7-5 [60]. These requirements are expressed in terms of the 2-norm and infinity norm. The 2-norm, $\|\cdot\|_2$, is defined for a continuous function $C[a,b]$ in Equation 7-1.

$$\left\| f(x) \right\|_2 = \sqrt{\int_a^b \left| f(x) \right|^2 dx}$$

Equation 7-1

The infinity norm, $\left\| \cdot \right\|_\infty$, is defined for a continuous function *C[a,b]* in Equation 7-2.

$$\left\| f(x) \right\|_\infty = \max_{a \le x \le b} \left| f(x) \right|$$

Equation 7-2

Equation 7-3 states that the root-mean-square torque required by the motor has to be lower than the continuous nominal motor torque, in order to prevent overheating of the machine winding insulation.

$$\left\| T_m(t) \right\|_2 \le T_n(t)$$

$$\left\| T_m(t) \right\|_2 = \sqrt{\frac{1}{\tau} \int_0^\tau \left| T_m(t) \right|^2 dt}$$

Equation 7-3

Equation 7-4 states that the required maximum motor torque needs to be lower or equal to the nominal motor peak torque.

$$\left\| T_m(t) \right\|_\infty \le T_{peak}(t)$$

$$\left\| T_m(t) \right\|_\infty = \max_{0 \le t \le \tau} \left| T_m(t) \right|$$

Equation 7-4

Equation 7-5 states that the required maximum motor speed needs to be lower or equal to the nominal maximum motor speed. The maximum motor speed limit depends on the mechanical machine limit and on the maximum supply voltage.

$$\left\|\omega_m(t)\right\|_\infty \leq \omega_{max}(t)$$

$$\left\|\omega_m(t)\right\|_\infty = \max_{0 \leq t \leq \tau} \left|\omega_m(t)\right|$$

Equation 7-5

Next, the emulating motor nominal and peak torque requirements are derived using the rotor dynamics equations defined for the free turbine and emulating motor. The required free turbine torque to drive the generator is given in Equation 7-6.

$$T_{ft}(t) = J_{ft} \frac{d\omega_{ft}(t)}{dt} + T_l(t) + T_{fft}(t)$$

Equation 7-6

, where $T_l(t)$ is the load torque, and J_{ft}, $\omega_{ft}(t)$ and $T_{fft}(t)$ correspond to the free turbine inertia, speed and friction torque, respectively. The required motor torque to drive the generator is given in Equation 7-7.

$$T_m(t) = J_m \frac{d\omega_m(t)}{dt} + T_l(t) + T_{fm}(t)$$

Equation 7-7

, where J_m, $\omega_m(t)$ and $T_{fm}(t)$ correspond to the emulating motor inertia, speed and friction torque, respectively.

It is desired that the free turbine and the emulating motor speeds and accelerations be equal when the motor is emulating the speed performance of the aeroderivative engine. This is stated in Equation 7-8.

$$\omega(t) = \omega_{ft}(t) = \omega_m(t)$$

$$\frac{d\omega(t)}{dt} = \frac{d\omega_{ft}(t)}{dt} = \frac{d\omega_m(t)}{dt}$$ **Equation 7-8**

The acceleration of the free turbine is expressed in Equation 7-9.

$$\frac{d\omega(t)}{dt} = \frac{T_{ft}(t) - T_l(t) - T_{fft}(t)}{J_{ft}}$$ **Equation 7-9**

Equation 7-9 in 7-7 yields Equation 7-10, which corresponds to the motor torque when emulating an engine.

$$T_m(t) = \frac{J_m}{J_{ft}} T_{ft}(t) + \left(1 - \frac{J_m}{J_{ft}}\right) T_l(t) + T_{fm}(t) - \frac{J_m}{J_{ft}} T_{fft}(t)$$ **Equation 7-10**

As can be seen from Equation 7-10, the emulation motor torque depends on the free turbine torque, the ratio of motor inertia to free turbine inertia, and the size of the desired step loading that is to be tested on the generator. The root-mean-square emulating motor torque and the maximum emulating motor torque are expressed in Equations 7-11 and 7-12 following Equations 7-3 and 7-4.

$$\left\| T_m(t) \right\|_2 = \sqrt{\frac{1}{\tau} \int_0^\tau \left(\frac{J_m}{J_{ft}} T_{ft}(t) + \left(1 - \frac{J_m}{J_{ft}} \right) T_l(t) + T_{fm}(t) - \frac{J_m}{J_{ft}} T_{fft}(t) \right)^2 dt}$$ **Equation 7-11**

$$\left\| T_m(t) \right\|_\infty = \max_{0 \le t \le \tau} \left| \frac{J_m}{J_{ft}} T_{ft}(t) + \left(1 - \frac{J_m}{J_{ft}} \right) T_l(t) + T_{fm}(t) - \frac{J_m}{J_{ft}} T_{fft}(t) \right|$$ **Equation 7-12**

7.1.1 Nominal Torque Emulation Requirement

The nominal torque requirement for emulating an aeroderivative twin-shaft engine using an AC motor can be stated mathematically as follows: Given an aeroderivative twin-shaft engine with free turbine inertia, J_{ft}, select a motor with inertia, J_m, and nominal torque, T_n, that satisfies,

$$\left\| T_m(t) \right\|_2 \le T_n(t)$$

, where

$$\left\| T_m(t) \right\|_2 = \sqrt{\frac{1}{\tau} \int_0^\tau \left(\frac{J_m}{J_{ft}} T_{ft}(t) + \left(1 - \frac{J_m}{J_{ft}} \right) T_l(t) + T_{fm}(t) - \frac{J_m}{J_{ft}} T_{fft}(t) \right)^2 dt}$$ **Equation 7-13**

7.1.2 Peak Torque Emulation Requirement

When emulating an aeroderivative engine using an AC motor there is special concern not to exceed the peak torque limit during transient conditions. The peak torque requirement for emulating an aeroderivative twin-shaft engine using an AC motor can be stated mathematically as follows: Given an aeroderivative twin-shaft engine with free turbine inertia, J_{ft}, select a motor with inertia, J_m, and peak torque, T_p, that satisfies,

$$\left\| T_m(t) \right\|_\infty \leq T_p(t)$$

, where

$$\left\| T_m(t) \right\|_\infty = \max_{0 \leq t \leq \tau} \left| \frac{J_m}{J_{ft}} T_{ft}(t) + \left(1 - \frac{J_m}{J_{ft}} \right) T_l(t) + T_{fm}(t) - \frac{J_m}{J_{ft}} T_{fft}(t) \right| \qquad \textbf{Equation 7-14}$$

7.2 Peak Power and Current Requirements of the Variable-Speed Drive

The motor input power is given by Equation 7-15.

$$P_m(t) = P_{loss}(t) + P_{mech}(t) \qquad \textbf{Equation 7-15}$$

The power loss is considered to be only related to heat resistive loss. The mechanical power is given in Equation 7-16.

$$P_{mech}(t) = T_m(t)\omega_m$$
$$= \frac{J_m}{J_{ft}} T_{ft}(t)\omega_m + \left(1 - \frac{J_m}{J_{ft}} \right) T_l(t)\omega_m + (T_{fm}(t) - \frac{J_m}{J_{ft}} T_{fft}(t))\omega_m \qquad \textbf{Equation 7-16}$$

Therefore, the drive peak power is defined in Equation 7-17 as,

$$P_{peak}(t) = \left\| P_m(t) \right\|_\infty = \max_{0 \leq t \leq \tau} \left(P_{loss}(t) + P_{mech}(t) \right) \qquad \textbf{Equation 7-17}$$

The maximum inverter drive line current can be calculated in terms of the drive peak power as expressed in Equation 7-18.

$$P_m(t) = \sqrt{3} v_{ab} i_a(t) \cos \delta$$

$$i_a(t) = \frac{P_m(t)}{\sqrt{3} v_{ab} \cos \delta}$$

$$i_{peak}(t) = \frac{P_{peak}(t)}{\sqrt{3} v_{ab} \cos \delta} \qquad\qquad \textbf{Equation 7-18}$$
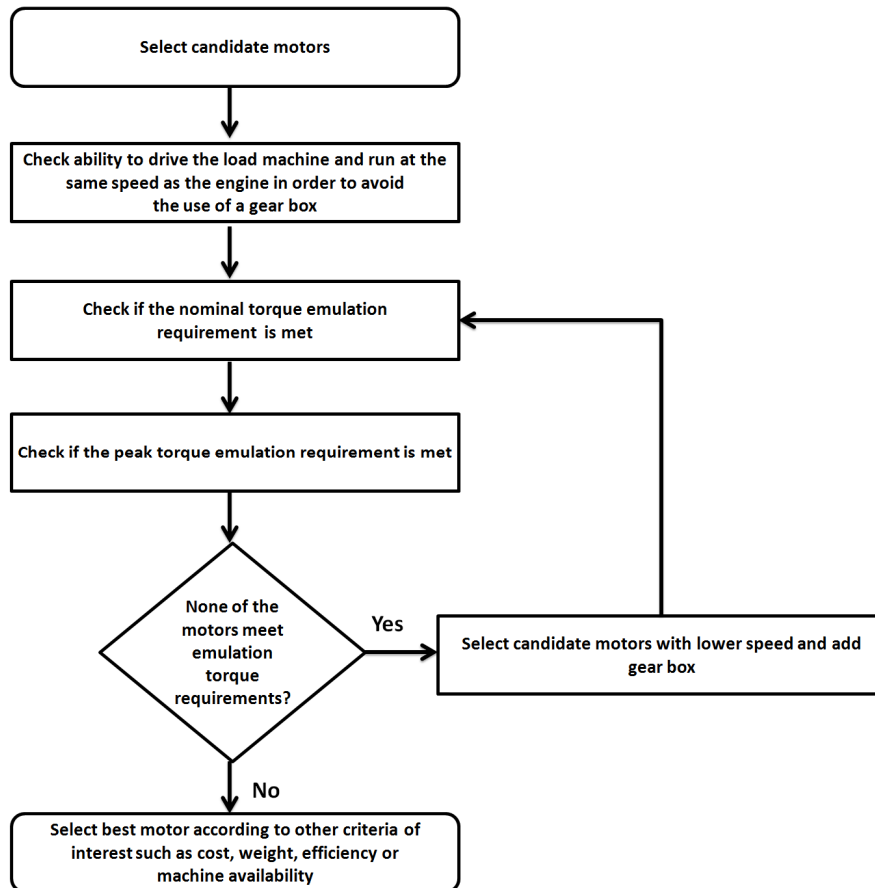
Figure 7.1: Flow diagram for the selection the emulating motor

7.3 Emulating Motor Selection Procedure

A selection procedure for determining the appropriate motor to emulate an aeroderivative engine is illustrated in the flow diagram in Figure 7.1.

7.4 Design Example

This design example is based on the aeroderivative engine emulation system described in Chapter 6. The 15 kW motor drive is used to emulate the aeroderivative twin-shaft engine model, when the motor inertia constant, H_m, is equal to the free turbine inertia constant, H_{ft}. The torque, power and current requirements are investigated for this case, during a torque load step from 0.9 to 1 pu. The motor speed and torque demand, transducer load torque and free turbine torque are measured during the torque load step. In order to verify the validity of Equation 7-10 experimentally, Figure 7.2 shows a comparison between the theoretical torque demand, which is the torque demand calculated using Equation 7-10, and the experimental torque demand. The theoretical torque matches the experimental torque demand except for an initial spike during the load step that can be associated with noise components that are not modeled in Equation 7-10. The motor friction torque in Equation 7-10 is obtained by subtracting the transducer load torque from the experimental torque demand. The free turbine friction torque is zero since the free turbine damping coefficient is not included in the calculation of the free turbine speed in the engine model.

Figure 7.3 shows the plot of motor peak torque, calculated using Equation 7-12, versus the ratio between motor and free turbine inertia constant, H_m/H_{ft}. Figure 7.4 shows the plot of motor peak power, calculated using Equation 7-17, versus H_m/H_{ft}. Figure 7.5 shows the plot of maximum inverter drive line current, calculated using Equation 7-18, versus H_m/H_{ft}. In these plots, the motor peak torque and power, and maximum inverter drive line current are averaged using a moving average function. It can be seen that the required peak torque and power, and

maximum inverter drive line current increases as the ratio between motor and free turbine inertia

constant is larger.
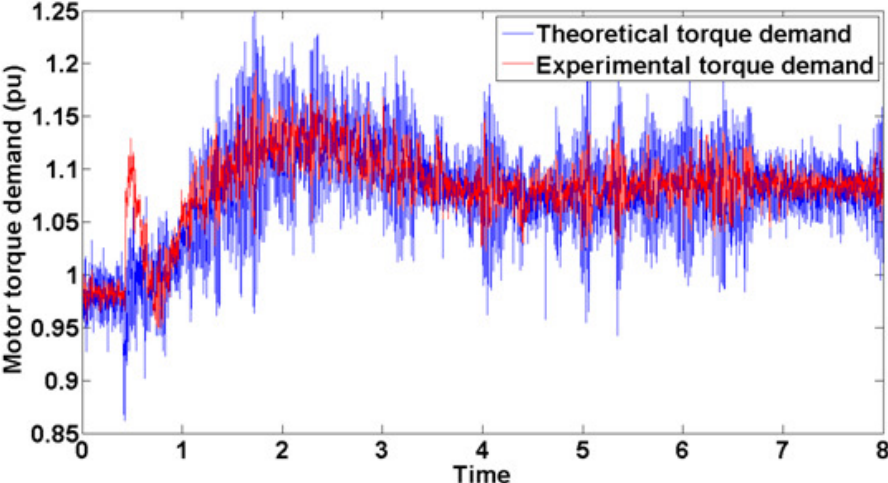
Figure 7.2: Comparison between theoretical and experimental torque demand
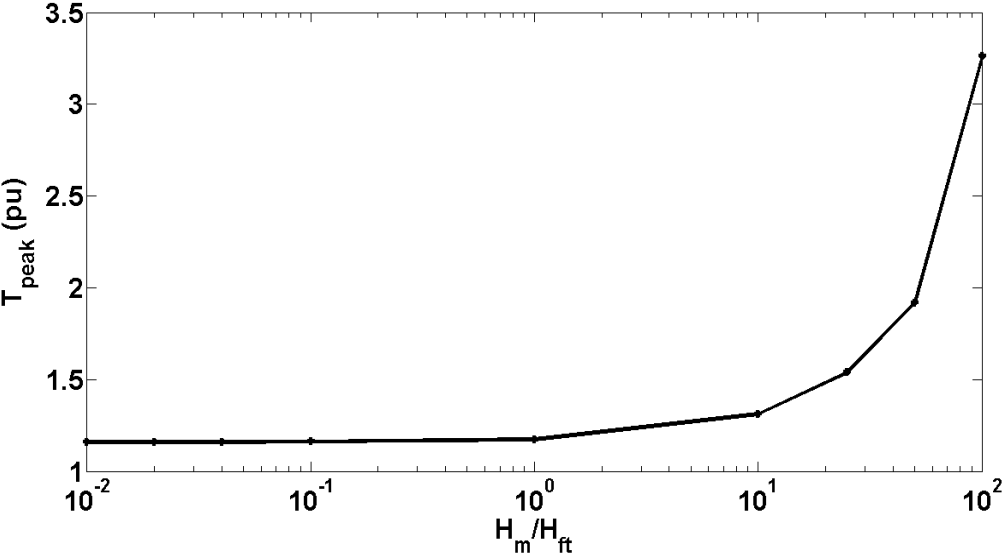
Figure 7.3: Motor peak torque vs H_m/H_{ft}
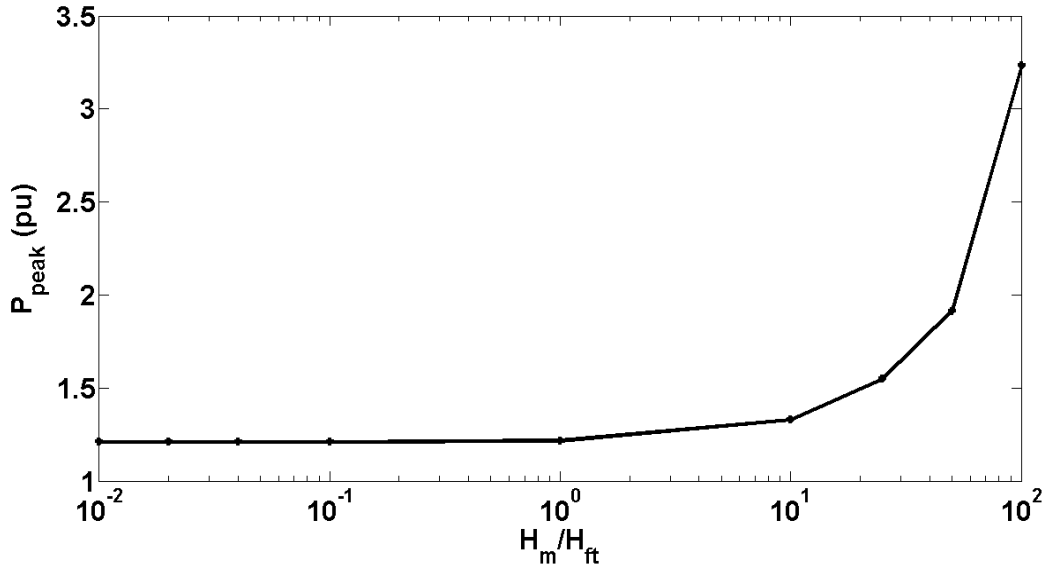
Figure 7.4: Motor peak power vs H_m/H_{ft}
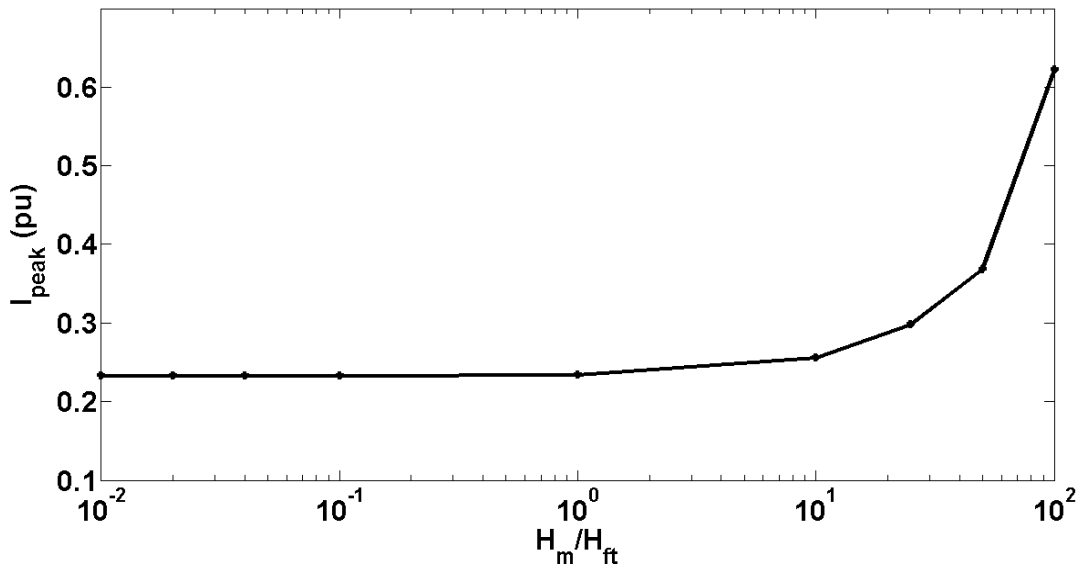
Figure 7.5: Motor peak current vs H_m/H_{ft}

As stated in Chapter 6, the Alstom motor drive torque demand limits can be specified by the user. However, the maximum allowable motor drive torque limit is 3 pu. Therefore, in the experimental test that follows the torque demand limits are varied in order to observe the effect

of not meeting the peak torque requirement when $H_m=H_{ft}$. According to Figure 7.3, when $H_m=H_{ft}$, the peak torque requirement is 1.176 pu.

Initially, a torque step from 0.9 to 1 pu is applied while the motor drive torque limit is set to 1.1 pu. Figure 7.6 shows the engine emulating motor speed tracking performance during this test. It can be seen that the motor speed controller saturates when tracking the free turbine speed, because the motor drive requires more torque for this size in step change, as predicted by Figure 7.3. Figure 7.7 shows the torque reference, motor torque demand, transducer torque and filtered transducer torque during this test. In this figure, it can be seen that the motor torque demand remains at the maximum torque limit after the torque step change is applied.

Next, a torque step from 0.9 to 1 pu is applied while the motor drive torque limit is set to 1.5 pu. Figure 7.8 shows the engine emulating motor speed tracking performance during this test. It can be seen that the speed controller does not saturate since the torque limit is adequate as predicted by Figure 7.3. Figure 7.9 shows the torque demand, torque reference, transducer torque and filtered transducer torque during this test. In this figure, it can be seen that the motor torque demand reaches a peak value of 1.16 pu during the step increase in load and settles in steady state at 1.08 pu.
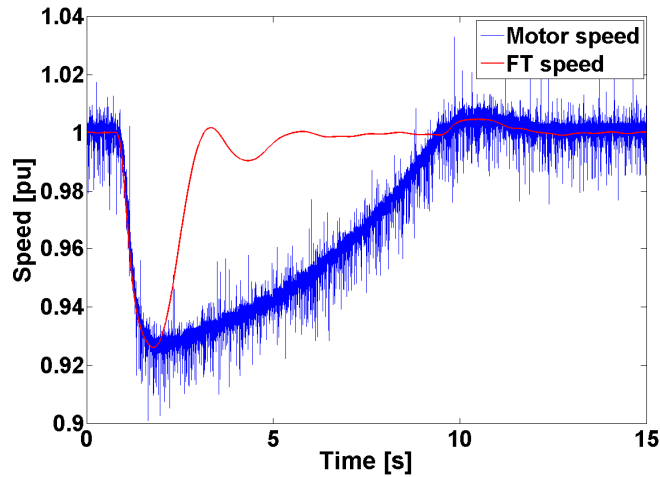
Figure 7.6: Emulating motor and free turbine speed when the load torque is stepped up from

0.9 to 1 pu and the torque limit is set to 1.1 pu
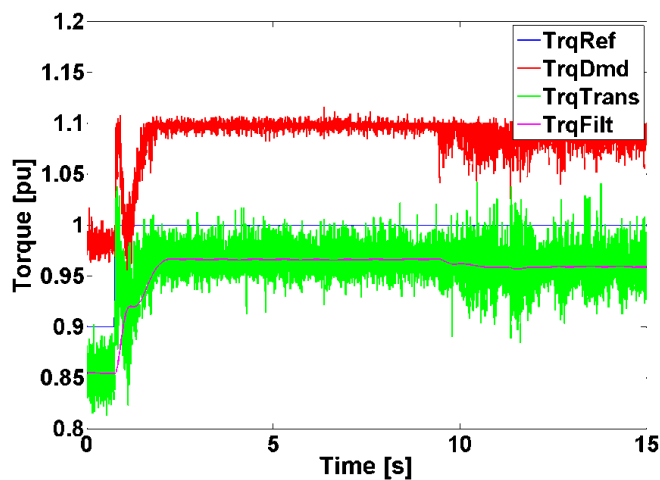
Figure 7.7: Torque reference, motor torque demand, transducer torque and filtered

transducer torque when the load torque is stepped up from 0.9 to 1 pu and the torque limit is

set to 1.1 pu
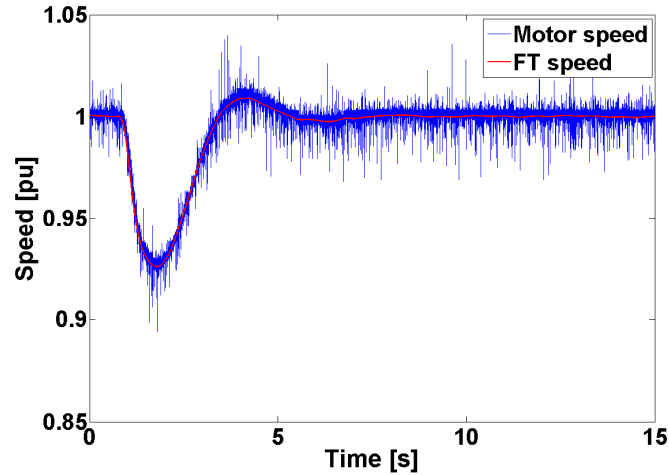
Figure 7.8: Emulating motor and free turbine speed when the load torque is stepped up from

0.9 to 1 pu and the torque limit is set to 1.5 pu
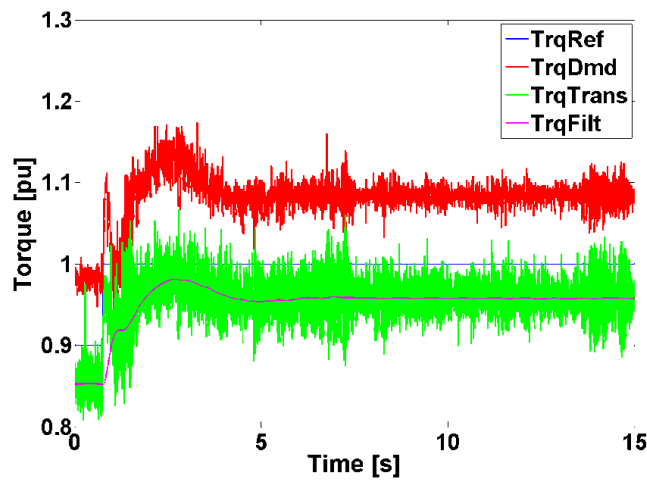
Figure 7.9: Torque reference, motor torque demand, transducer torque and filtered

transducer torque when the load torque is stepped up from 0.9 to 1 pu and the torque limit is

set to 1.5 pu

7.5 Discussion and Chapter Summary

A method for selecting the AC electric motor and variable-speed drive that are used for

emulating the steady-state, and transient loading and unloading dynamics of an aeroderivative

twin-shaft gas turbine engine model has been presented in this chapter. The method includes the definition of the emulating motor nominal and peak torque requirements, and the peak power and current requirements of the variable-speed drive. These requirements depend on the inertia constant ratio between the emulating motor and free turbine, and on the size of the desired step loading that is to be tested on the generator. A design example has shown that the emulating motor drive peak torque and power, and maximum inverter drive line current demands increase when the inertia of the motor is larger than the inertia of the free turbine. Experimental results also show that if the emulating motor does not meet the peak torque requirement when emulating an engine, speed controller saturation occurs and the engine emulation system is no longer capable of tracking the speed performance of the free turbine.

.

CHAPTER 8: MODEL-BASED ANALYSIS OF AN AERODERIVATIVE TWIN-SHAFT GAS TURBINE ENGINE EMULATION SYSTEM

This chapter presents a model-based analysis of the engine emulation system described in Chapter 6. The model-based analysis is developed using a linear model of the engine emulation system, and it allows the study of system stability and inertia loading effects. Experimental results demonstrate the validity of the model-based analysis.

8.1 Linear Model of an Aeroderivative Engine Emulation System

The model-based analysis of the engine emulation system is based on a simplified model of the experimental setup presented in Chapter 6. The block diagram of the engine emulation system model is shown in Figure 8.1. This model uses transfer function based approximations to describe the motor drive speed control loop, the shaft dynamics, and the generator torque control loop. The terms J_m, J_g, K_t and K_{eq} correspond to motor inertia, generator inertia, generator torque constant and shaft coupling constant, respectively. In this model, T_g^* refers to the reference generator torque of the generator torque control loop.

In this engine emulation system model, the aeroderivative twin-shaft engine model described in Chapter 5 is further simplified for analysis purposes so that the engine emulation model only considers the actuation of the free turbine governor for the determination of the fuel demand. This is reasonable during steady-state, and small transient loading and unloading conditions since the control input to the fuel system is provided by the free turbine speed governor.
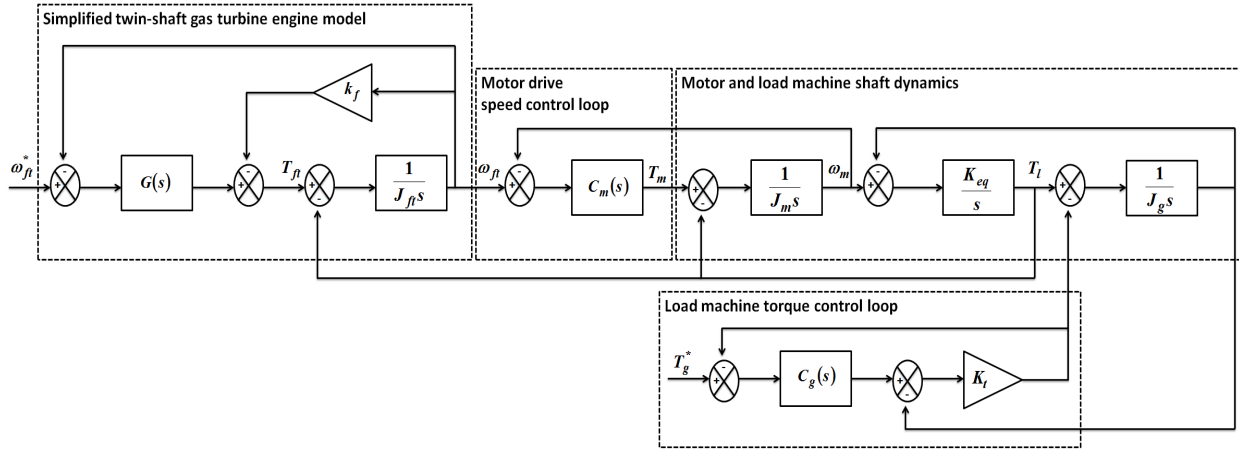
Figure 8.1: Block diagram of aeroderivative engine emulation system

Equation 8-1 defines the transfer functions included in Figure 8.1, and Table 8.1 describes the engine emulation system model parameters.

$$G(s) = \frac{k_{f1ma}}{k_{f1mb}} H_{SG}(s) H_{VP}(s) H_{FS}(s) H_C(s) H_{CP}(s)$$

$$k_f = \frac{0.6 T_b}{k_{f1mb} \omega_b}$$

$$C_m(s) = \frac{K_{pm}s + K_{im}}{s}$$

$$C_g(s) = \frac{K_{pg}s + K_{ig}}{s} \qquad\qquad \textbf{Equation 8-1}$$

Table 8.1: Aeroderivative engine emulation system model parameters

Symbol	Quantity	Value
T_b	base torque	159 N·m
ω_b	base speed	92.15 rad/s
K_{pm}	motor drive speed controller proportional constant	219.43
K_{im}	motor drive speed controller integral constant	483.64
K_{pg}	load machine drive torque controller proportional constant	0.5
K_{ig}	load machine drive torque controller integral constant	1
b_1	Butterworth filter parameter	$1.421 \cdot 10^{-9}$
b_2	Butterworth filter parameter	0.0002369
b_3	Butterworth filter parameter	39.48
a_2	Butterworth filter parameter	8.886
a_3	Butterworth filter parameter	39.48
K_{eq}	shaft coupling constant	$9.0735 \cdot 10^{3}$
K_t	torque constant	44.1579

8.2 Analysis of Stability and Inertia Loading Effects

In this analysis, non-emulation mode or open-loop testing refers to the case when the speed reference of the motor drive is a constant value and the torque signal obtained from the torque transducer on the motor-generator shaft is fed to the engine model. On the other hand, emulation mode or closed-loop testing refers to the case when the engine provides the speed reference to motor drive while the torque signal is fed to the engine model. Next, two cases are considered in order to investigate the stability and the effect of inertia loading in the aeroderivative engine emulation system.

8.2.1 Case 1: Engine Emulation when ω_{ft}^* is Varied and T_g^* is a Constant Value

The non-emulation mode is analyzed first in order to determine the transfer function that determines the output ω_{ft} that is used as reference for the aeroderivative engine emulation system when variations in ω_{ft}^* occur while T_g^* is maintained at a constant value. Therefore, the engine

emulation system block diagram is reduced as shown in Figure 8.2 for the analysis of non-emulation mode Case 1. The motor drive speed control loop, the motor and generator shaft dynamics, and the generator torque loop do not have an effect on this transfer function since ω_{ft} is not connected to the reference input of the motor drive and T_l remains a constant since T_g^* is not varied. The transfer function from input ω_{ft}^* to output ω_{ft} in emulation mode is given by $G_{\omega 1}(s)$ in Equation 8-2. The transfer function $K(s)$ is defined as $K(s) = k_f + G(s)$.

$$G_{\omega 1}(s) = \frac{\omega_{ft}}{\omega_{ft}^*} = \frac{\dfrac{G(s)}{J_{ft}}}{s + \dfrac{K(s)}{J_{ft}}}$$

Equation 8-2

The transfer function of a Butterworth low-pass filter, which is used to filter the high-frequency components in the signal obtained from the shaft torque transducer, is given in Equation 8-3.

$$F(s) = \frac{b_1 s^2 + b_2 s + b_3}{s^2 + a_2 s + a_3}$$

Equation 8-3

118
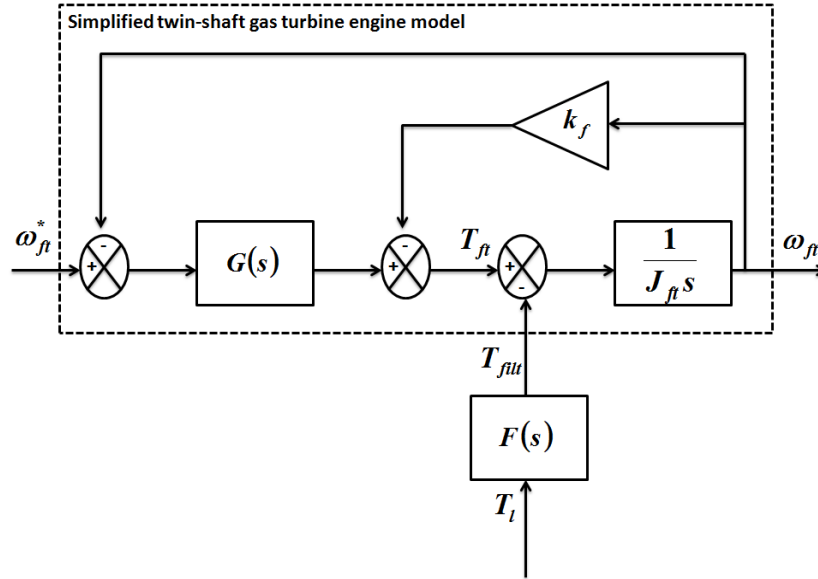
Figure 8.2: Block diagram for non-emulation mode Case 1
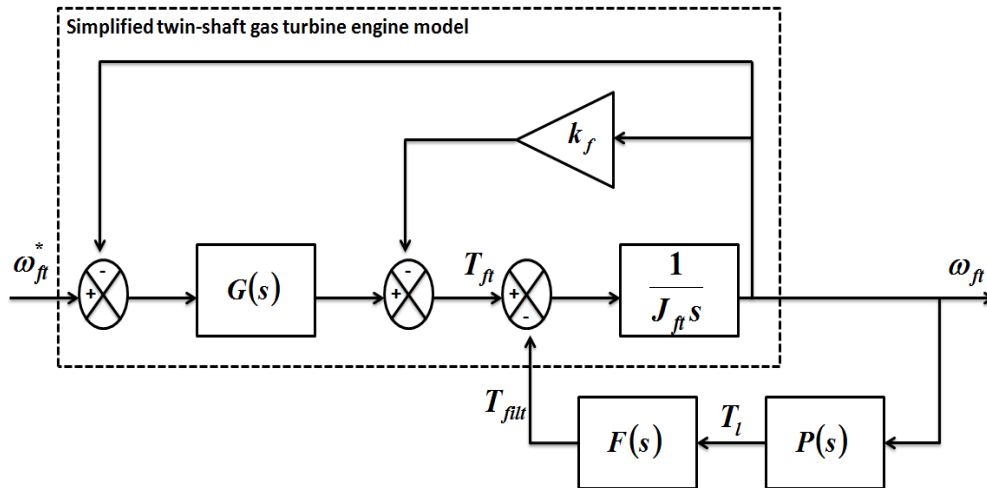
Figure 8.3: Block diagram for emulation mode Case 1

In emulation mode, Case 1 yields the block diagram representation shown in Figure 8.3. In this case, ω_{ft} is connected to the reference input of the motor drive so that the motor tracks the performance of the engine during variations in ω_{ft}^* while T_g^* remains constant. Therefore, the motor drive speed control loop, the motor and generator shaft dynamics, and the generator torque loop influence the transfer function from input ω_{ft}^* to output ω_{ft}, $G_{\omega 2}(s)$. The transfer function $G_{\omega 2}(s)$ is given in Equation 8-4 with $Q_1(s) = F(s) \cdot P(s)$. The interaction of the motor drive speed

control loop, the motor and generator shaft dynamics, and the generator torque loop transfer function is described by $P(s)$, which is the transfer function from input ω_{ft} to output T_l. The transfer function $P(s)$ is given in Equation 8-5.

$$G_{\omega 2}(s) = \frac{\omega_{ft}}{\omega_{ft}^*} = \frac{\dfrac{G(s)}{J_{ft}}}{\left(s + \dfrac{K(s)}{J_{ft}}\right) + \dfrac{Q_1(s)}{J_{ft}}}$$

Equation 8-4

$$P(s) = \frac{T_l}{\omega_{ft}} = \frac{\dfrac{K_{eq}C_m(s)H_m(s)}{s}}{1 + \dfrac{K_{eq}}{s}\left(T_g(s) + H_m(s)\right)}$$

Equation 8-5

When comparing Equations 8-2 and 8-4 it can be seen that if J_{ft} is large we can approximate the emulation mode transfer function, $G_{\omega 2}(s)$, to the non-emulation mode transfer function, $G_{\omega 1}(s)$. However, when J_{ft} is small the emulation mode transfer function, $G_{\omega 2}(s)$, will be different from the non-emulation mode transfer function, $G_{\omega 1}(s)$. This explains the effect of inertial loading when the system goes from open to closed-loop. In the closed-loop system the inertia of the generator affects the dynamic response of the free turbine.

The stability of the emulation system depends on the poles of $G_{\omega 2}(s)$, which are given by the solution of the characteristic equation in Equation 8-6. The emulation system will be stable if all the roots of Equation 8-6 have negative real parts.

$$\left(s + \frac{K(s)}{J_{ft}}\right) + \frac{Q_1(s)}{J_{ft}} = 0$$

Equation 8-6

120

8.2.2 Case 2: Engine Emulation when $T_g{}^*$ is Varied and $\omega_{ft}{}^*$ is a Constant Value

In non-emulation mode, Case 2 yields the block diagram representation shown in Figure 8.4. Since $T_g{}^*$ is varied in this case instead of $\omega_{ft}{}^*$, the transfer function from input $T_g{}^*$ to output ω_{ft} in non-emulation mode, $G_{T1}(s)$, is influenced by the motor drive speed control loop, the motor and generator shaft dynamics, and the generator torque loop. The transfer function terms presented in Figure 8.4 are defined in Equation 8-7. The transfer function $G_{T1}(s)$ is given in Equation 8-8.

$$H_t(s) = \frac{\dfrac{K_{eq}}{s}}{1 + \dfrac{K_{eq}}{s}T_g(s)}$$

$$T_g(s) = \frac{\dfrac{1}{J_g s}}{1 - \dfrac{M_g(s)}{J_g s}}$$

$$M_g(s) = \frac{K_t}{1 + K_t C_g(s)}$$

$$H_g(s) = M_g(s)C_g(s)T_g(s)$$

$$H_m(s) = \frac{\dfrac{1}{J_m s}}{1 + \dfrac{C_m(s)}{J_m s}}$$

Equation 8-7

$$G_{T1}(s) = \frac{\omega_{ft}}{T_g^*} = \frac{\dfrac{-H_g(s)H_t(s)F(s)}{J_{ft}}}{s(1 + H_t(s)H_m(s)) + \dfrac{K(s)}{J_{ft}}(1 + H_t(s)H_m(s))}$$

Equation 8-8

In emulation mode, Case 2 yields the block diagram representation shown in Figure 8.5. The transfer function from input T_g^* to output ω_{ft} in emulation mode, $G_{T2}(s)$, is given in Equation 8-9 with $Q_2(s) = H_t(s) \cdot H_m(s) \cdot C_m(s) \cdot F(s)$.

$$G_{T2}(s) = \frac{\omega_{ft}}{T_g^*} = \frac{\dfrac{-H_g(s)H_t(s)F(s)}{J_{ft}}}{s(1 + H_t(s)H_m(s)) + \dfrac{K(s)}{J_{ft}}(1 + H_t(s)H_m(s)) + \dfrac{Q_2(s)}{J_{ft}}}$$

Equation 8-9

Similar to Case 1, it can be observed from Equations 8-8 and 8-9 that if J_{ft} is large we can approximate the emulation mode transfer function, $G_{T2}(s)$, to the non-emulation mode transfer function, $G_{T1}(s)$. However, when J_{ft} is small the emulation mode transfer function, $G_{T2}(s)$, will be different from the non-emulation mode transfer function, $G_{T1}(s)$. This comparison allows us to explain the effect of inertial loading when the system goes from open to closed-loop.

The stability of the emulation system depends on the poles of $G_{T2}(s)$, which are given by the solution of the characteristic equation in Equation 8-10. The emulation system will be stable if all the roots in Equation 8-10 have negative real parts.

$$s(1 + H_t(s)H_m(s)) + \frac{K(s)}{J_{ft}}(1 + H_t(s)H_m(s)) + \frac{Q_2(s)}{J_{ft}} = 0$$

Equation 8-10
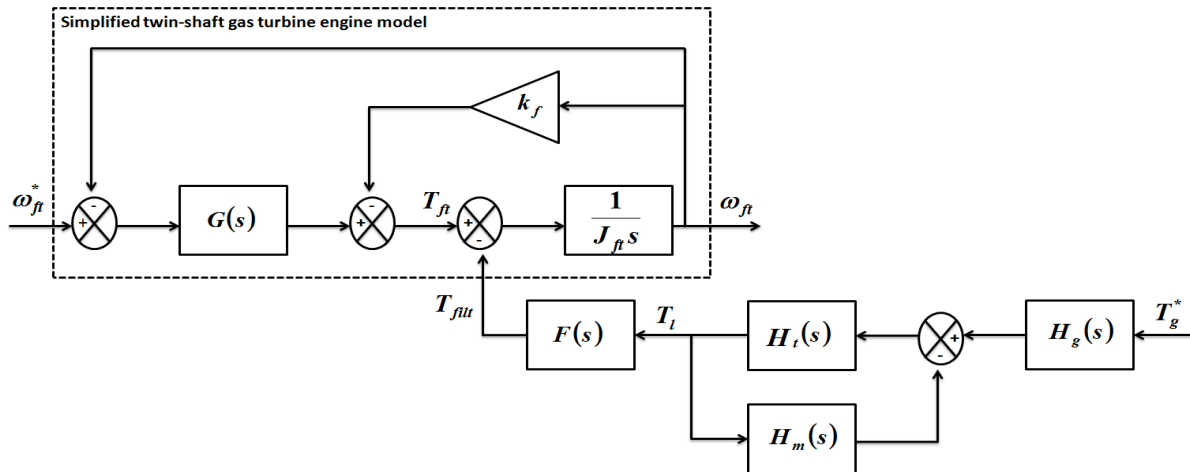
Figure 8.4: Block diagram for non-emulation mode Case 2
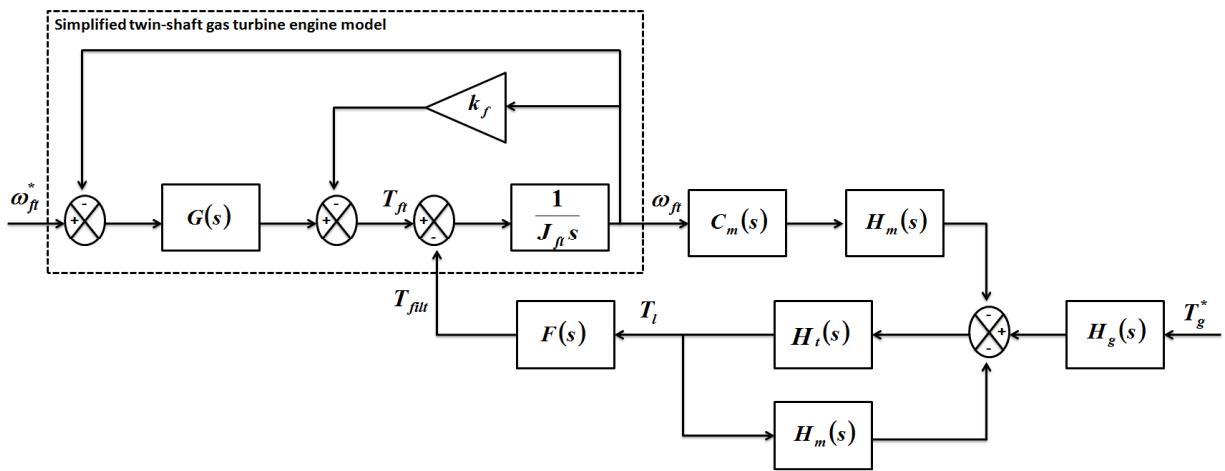
Figure 8.5: Block diagram for emulation mode Case 2

8.3 Simulation Example

In this section, the analysis of stability and inertia loading effects is applied to the engine emulation system model of the low-power HIL setup when the free turbine inertia is varied so that $H_{ft}=H_m \cdot 10=1.261\ s$ (low inertia case) and $H_{ft}=H_m/10=0.01261\ s$ (high inertia case). The cutoff frequency of the Butterworth low-pass filter on the torque transducer signal is varied between 10 and 1 Hz, in order to observe the effect that the low frequency oscillations in the measured torque have on the engine emulation. The pole locations resulting from the parameter

123

variations of the emulation mode Case 1 system transfer function, $G_{\omega 2}(s)$, are presented in Table 8.2. In Table 8.2, it can be seen that the pole locations of $G_{\omega 2}(s)$ for the low inertia case and both filter designs have negative real parts, so the emulation system in this case is expected to present stability. Furthermore, in the low inertia case, Figures 8.6 and 8.7 reveal that $G_{\omega 2}(s)$ presents a similar frequency response to $G_{\omega 1}(s)$. Therefore, in the low inertia case it is expected that the system response is similar in non-emulation and emulation modes.

Table 8.2: Pole locations of engine emulation system for Case 1

Variations of $G_{\omega 2}(s)$	Pole locations
Low inertia case when low-pass filter cutoff frequency is 10 Hz	-350.73; -18.79 + 130.98i; -18.79 - 130.98i; -44.65 + 50.05i; -44.65 - 50.05i; -19.96; -10.18; -2.45; -2.26; -1.58; -0.09 + 0.93i; -0.09 - 0.93i
Low inertia case when low-pass filter cutoff frequency is 1 Hz	-350.52; -18.94 + 132.65i; -18.94 - 132.65i; -19.95; -10.19; -4.66 + 5.01i; -4.66 - 5.01i; -2.46; -2.24; -0.09 + 0.92i; -0.09 - 0.92i; -1.50;
High inertia case when low-pass filter cutoff frequency is 10 Hz	-368.99; -124.42+157.97i; -124.42-157.97i; <u>55.16 + 130.41i</u>; <u>55.16 - 130.41i</u>; -19.73; -11.11; -2.44; -2.16; -1.12; <u>0.19 + 3.30i</u>; <u>0.19 - 3.30i</u>
High inertia case when low-pass filter cutoff frequency is 1 Hz	-350.70; -19.48 + 131.20i; -19.48 - 131.20i; -19.62 + 18.83i; -19.62 - 18.83i; -2.45; -14.23 + 1.89i; -14.23 - 1.89i; -2.18; -1.07; -0.32 + 2.79i; -0.32 - 2.79i

The high inertia case only presents stability in emulation mode when the low-pass filter on the torque transducer signal is designed to have a cutoff frequency of 1 Hz but not 10 Hz. In Table 8.2, it can be seen that in this case $G_{\omega 2}(s)$ has two positive complex conjugate poles when the cutoff frequency of the low-pass filter is set to 10 Hz. Furthermore, Figures 8.8 and 8.9 reveal that in the high inertia case there are magnitude and phase differences between $G_{\omega 2}(s)$ and $G_{\omega 1}(s)$. This indicates a different system response in non-emulation and emulation modes.

Figure 8.6: Bode diagram of $G_{\omega 1}(s)$ and $G_{\omega 2}(s)$ for low inertia case (low-pass filter cutoff frequency is 10 Hz)
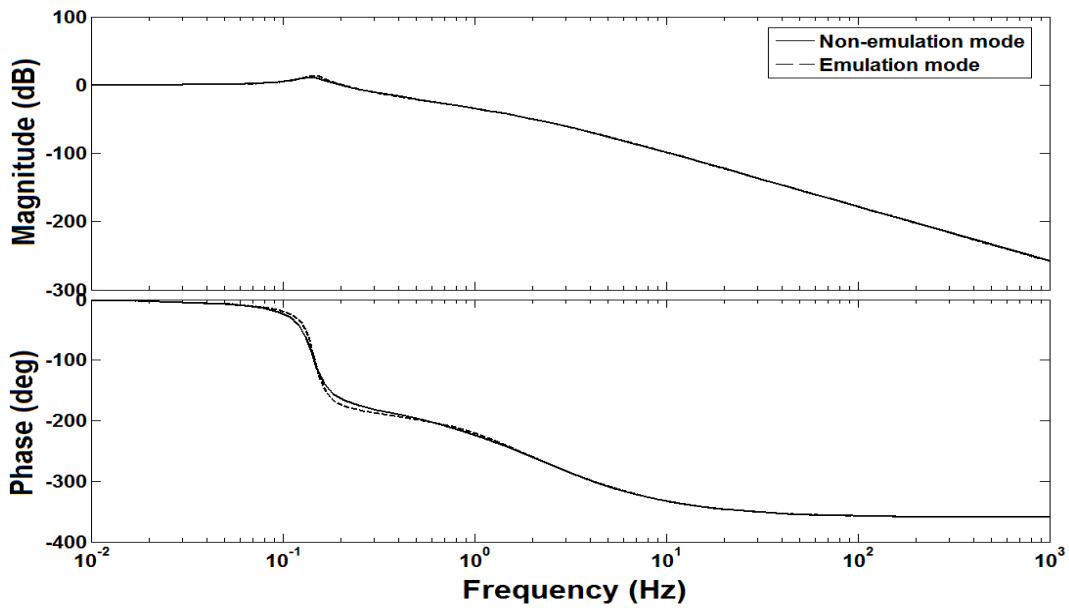
Figure 8.7: Bode diagram of $G_{\omega 1}(s)$ and $G_{\omega 2}(s)$ for low inertia case (low-pass filter cutoff frequency is 1 Hz)
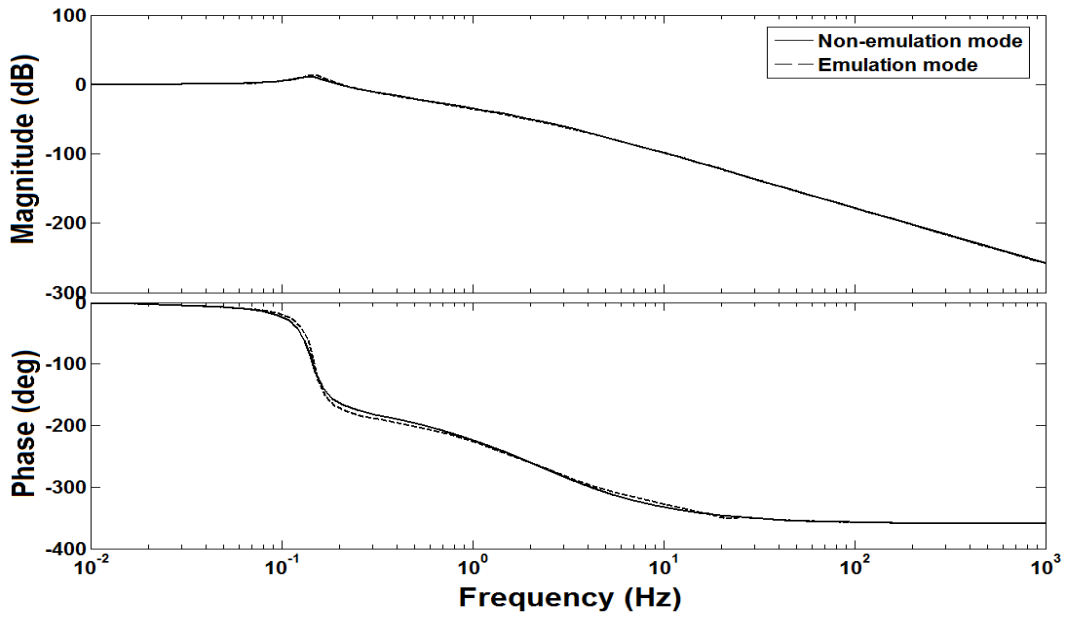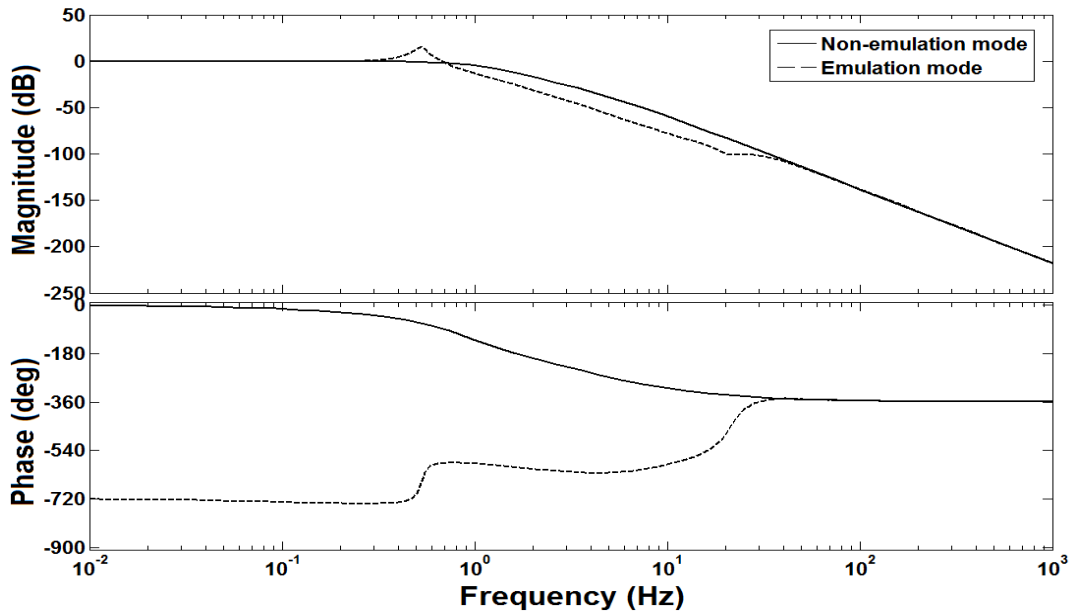
Figure 8.8: Bode diagram of $G_{\omega 1}(s)$ and $G_{\omega 2}(s)$ for high inertia case (low-pass filter cutoff frequency is 10 Hz)
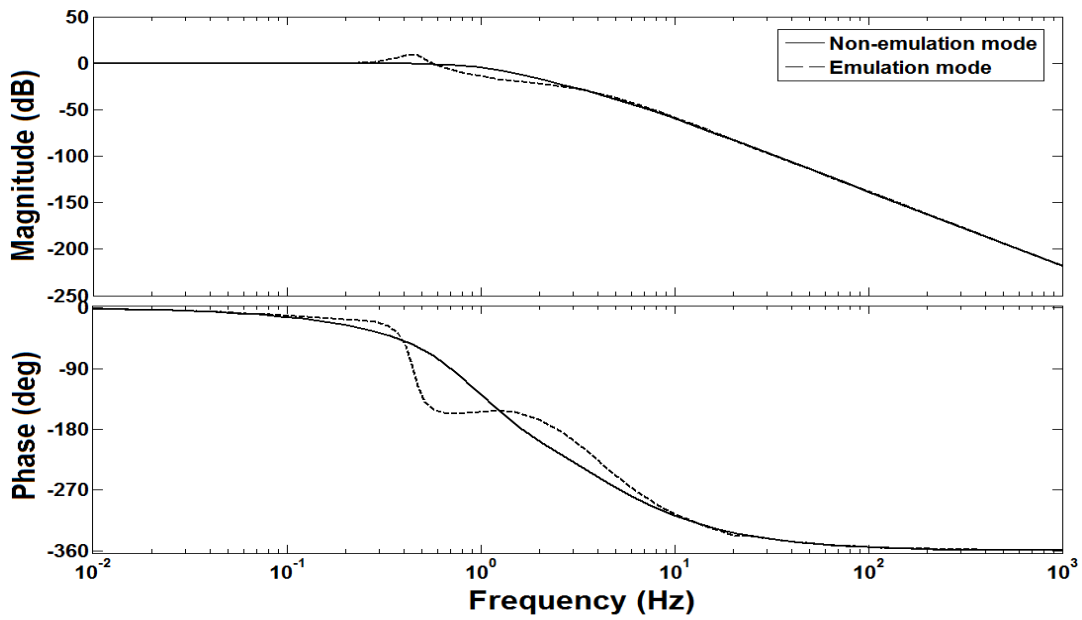
Figure 8.9: Bode diagram of $G_{\omega 1}(s)$ and $G_{\omega 2}(s)$ for high inertia case (low-pass filter cutoff frequency is 1 Hz)

126

8.4 Experimental Verification of Stability and Inertia Loading Effects Analysis

First, the inertia loading effects in the aeroderivative engine emulation system are analyzed. A comparison between the free turbine response in non-emulation and emulation modes is presented in Figures 8.10, 8.11 and 8.12 for the low and high inertia cases, when the low-pass filter on the torque transducer signal cuts off at 1 Hz. In Figure 8.10, ω_{ft}^* is stepped down from 1 to 0.98 pu while T_g^*=1pu (Case 1). In Figure 8.11, the load torque is stepped up from 0.9 to 1 pu while ω_{ft}^*=1 pu (Case 2). In Figure 8.12, the load torque is stepped down from 1 to 0.9 pu while ω_{ft}^*=1 pu (Case 2). As predicted by the model-based analysis, the free turbine speed in emulation or closed-loop mode changes significantly compared to the free turbine speed in non-emulation or open-loop mode as the inertia constant of the engine is decreased. This is because the inertia of the generator affects the dynamic response of the free turbine when the system is operated in closed-loop mode.

Next, stability issues that arise when performing the emulation studies are discussed. The speed tracking performance in the low inertia case when the low-pass filter on the torque transducer signal cuts off at 10 Hz is shown in Figures 8.13 and 8.14. In Figure 8.13, ω_{ft}^* is stepped down from 1 to 0.98 pu while T_g^*=1 pu (Case 1). In Figure 8.14, the load torque is stepped up from 0.9 to 1 pu while ω_{ft}^*=1 pu (Case 2). As predicted by the simulation model, in emulation mode, the low inertia case is stable and has good tracking performance when the low-pass filter cutoff frequency is 10 Hz. Figure 8.15 shows the high inertia case when the system is switched from non-emulation to emulation mode. In this case, the low-pass filter on the torque transducer signal cuts off at 10 Hz and T_g^*=0 pu. As predicted by the simulation model, the system becomes unstable, showing oscillations in the motor speed and torque. The source of the instability appears to be due, at least in part, to low frequency oscillations in the torque demand,

which are understood to be due to low damping in the dynamometer drive train and aggressive speed control settings. The inertia of the free turbine also plays a role in the stability by providing a degree of filtering of the measured torque.

The speed tracking performance in the low and high inertia cases when the low-pass filter on the torque transducer signal cuts off at 1 Hz is shown in Figures 8.16, 8.17 and 8.18. In Figure 8.16, ω_{ft}^* is stepped down from 1 to 0.98 pu while $T_g^*=1$ pu (Case 1). In Figure 8.17, the load torque is stepped up from 0.9 to 1 pu while maintaining $\omega_{ft}^*=1$ pu (Case 2). In Figure 8.18, the load torque is stepped down from 1 to 0.9 pu while $\omega_{ft}^*=1$ pu (Case 2). As predicted by the simulation model, in emulation mode, both inertia cases present stability and good tracking performance when the low-pass filter cutoff frequency is 1 Hz. In the high inertia case, it can be observed that the 1 Hz cutoff frequency of the filter provides stability but smooths out torque oscillations. The selection of the low-pass filter on the torque measurement can affect the stability of the engine emulation, and the system can become unstable if there is not enough filtering to smooth out any torque oscillations on the torque measurement. In the low inertia case, a larger filter cutoff frequency is possible because the larger free turbine inertia smooths out the torque oscillations.
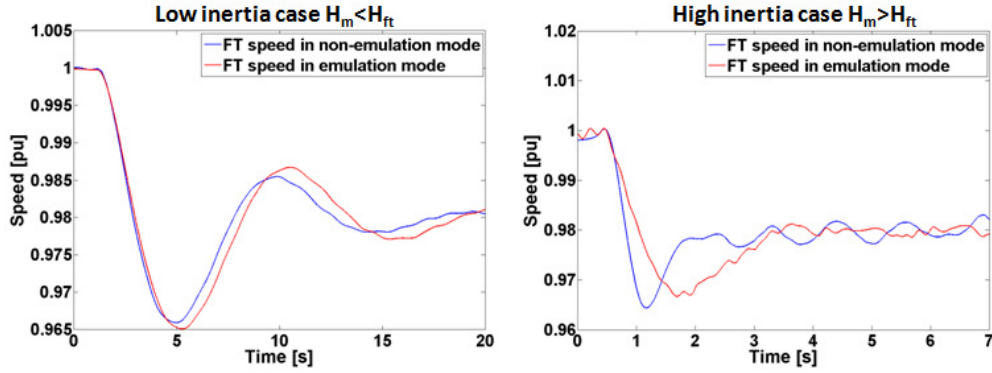
Figure 8.10: Non-emulation vs emulation free turbine speed comparison when ω_{ft}^* is stepped down from 1 to 0.98 pu with T_g^*=1 pu
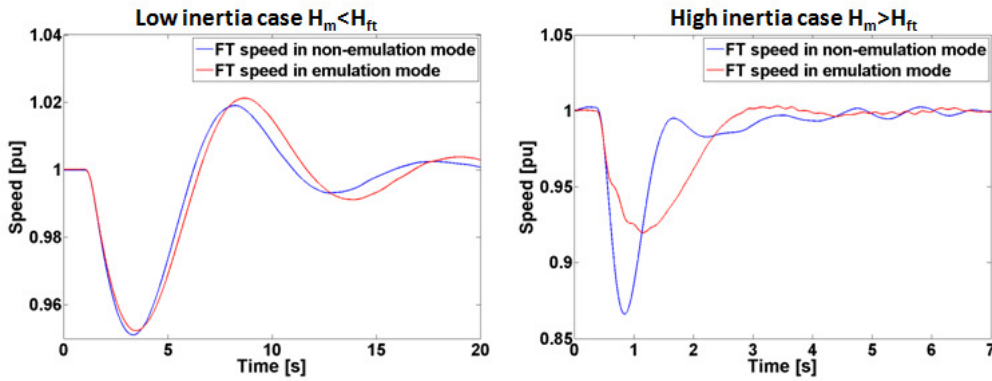
Figure 8.11: Non-emulation vs emulation free turbine speed comparison when the load torque is stepped up from 0.9 to 1 pu with ω_{ft}^*=1 pu
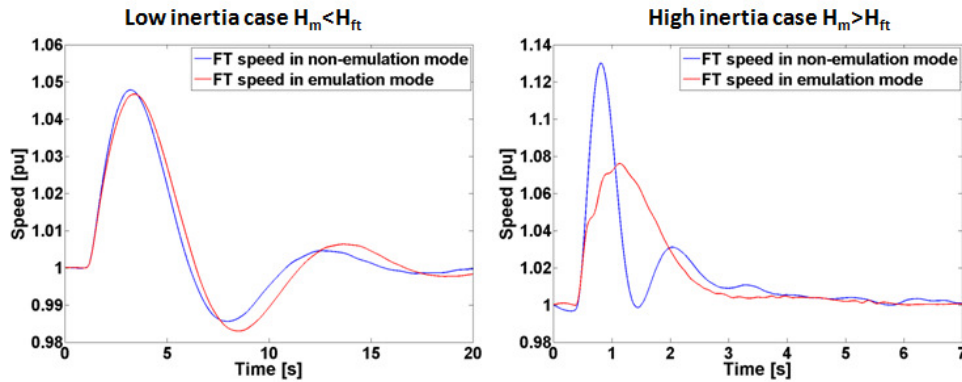
Figure 8.12: Non-emulation vs emulation free turbine speed comparison when the load torque is stepped down from 1 to 0.9 pu with ω_{ft}^*=1 pu

129
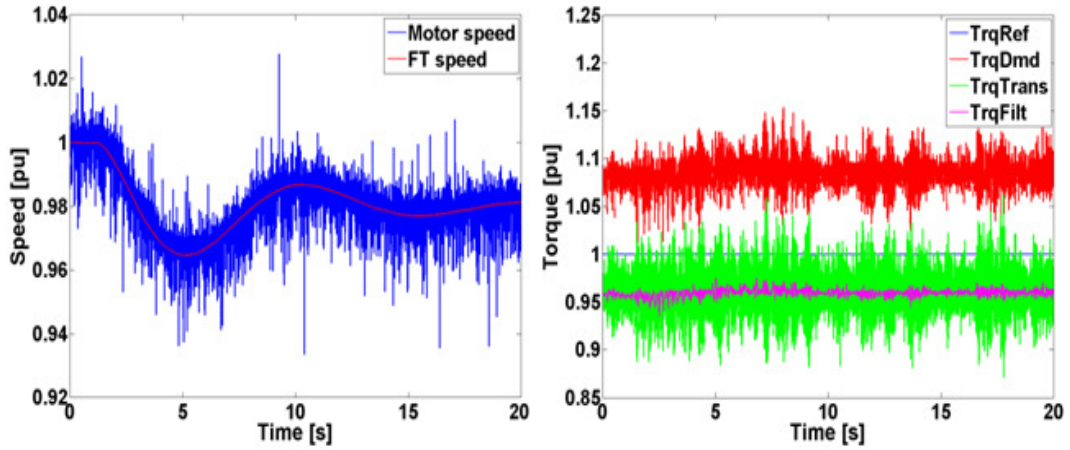
Figure 8.13: Speed tracking performance in the low inertia case when $\omega_{ft}{}^*$ is stepped down from 1 to 0.98pu with T_g=1 pu (low-pass filter cutoff freq. is 10 Hz)
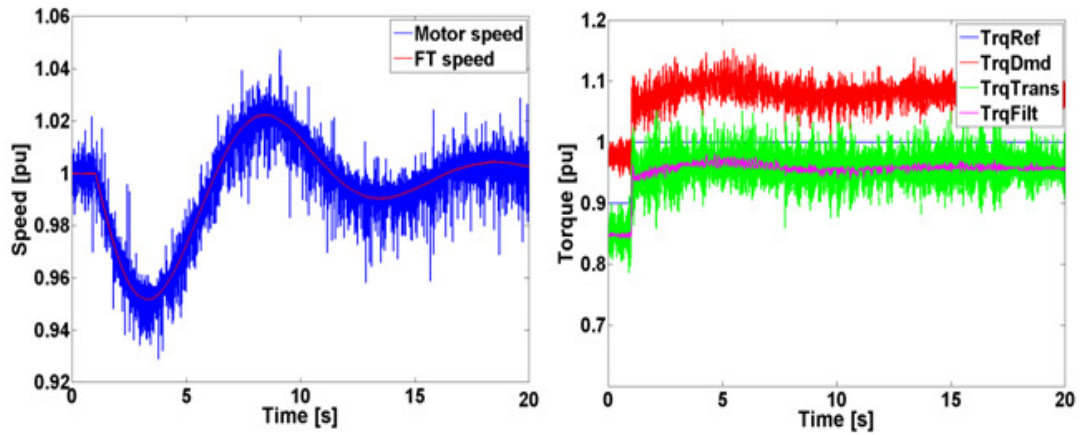
Figure 8.14: Speed tracking performance in the low inertia case when the load torque is stepped up from 0.9 to 1 pu with $\omega_{ft}{}^*$=1 pu (low-pass filter cutoff freq. is 10 Hz)
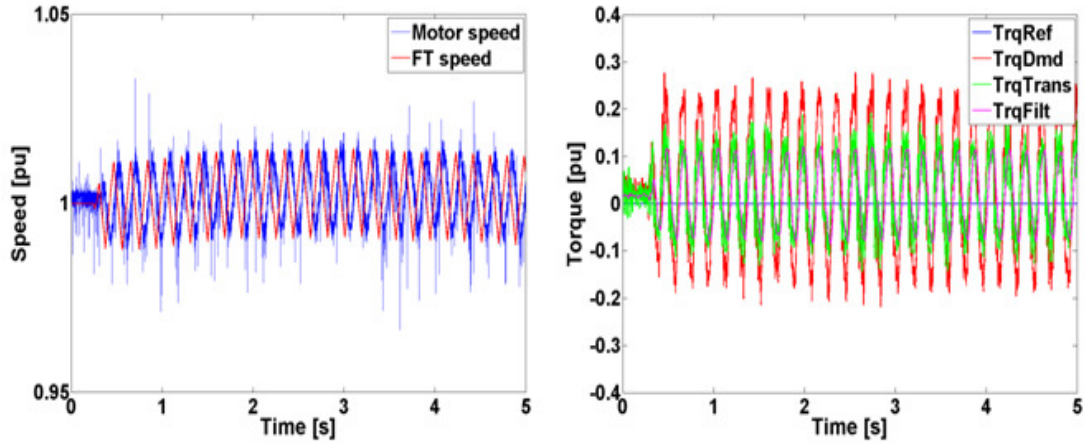
Figure 8.15: Switching from non-emulation to emulation mode in the high inertia case (low-pass filter cutoff freq. is 10 Hz)
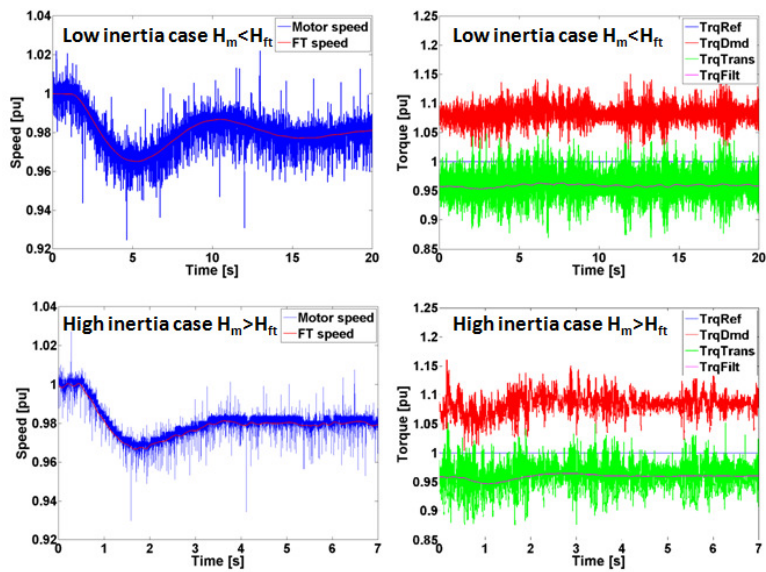
Figure 8.16: Speed tracking performance in the low and high inertia cases when ω_{ft}^* is stepped down from 1 to 0.98 pu with T_g^*=1 pu (low-pass filter cutoff freq. is 1 Hz)
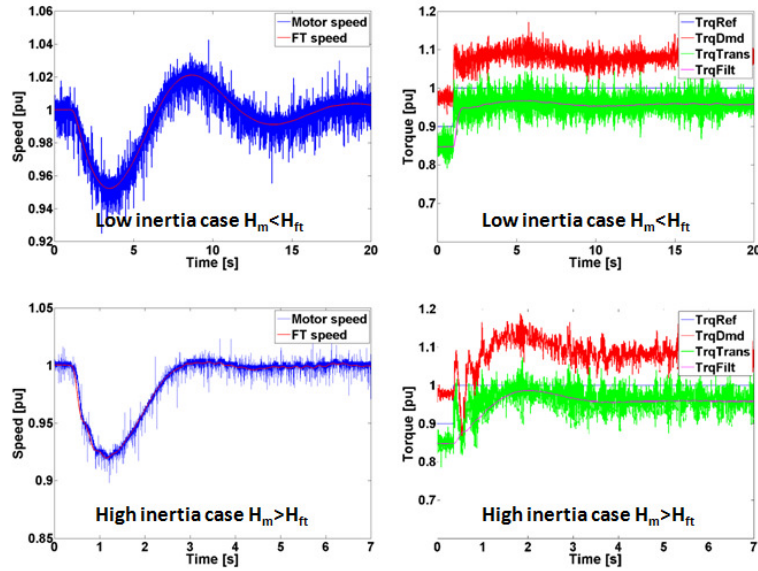
Figure 8.17: Speed tracking performance in the low and high inertia cases when the load torque is stepped up from 0.9 to 1 pu with ω_{ft}^* =1 pu (low-pass filter cutoff freq. is 1 Hz)
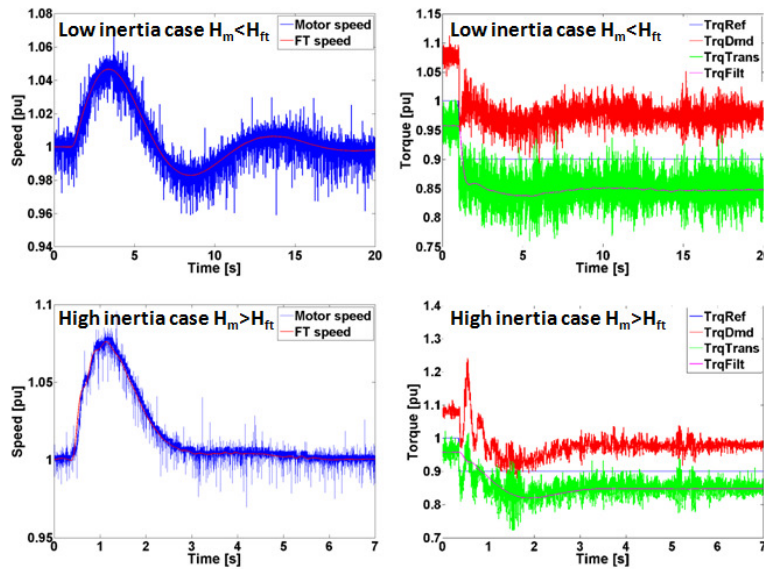
Figure 8.18: Speed tracking performance in the low and high inertia cases when the load torque is stepped down from 1 to 0.9 pu with ω_{ft}^* = 1 pu (low-pass filter cutoff freq. is 1 Hz)

8.5 Discussion and Chapter Summary

This chapter has presented a model-based analysis of an aeroderivative gas turbine engine emulation system that enables the examination of system stability and the effect of inertia coupling. The stability of the aeroderivative engine emulation system can be affected by the design of the low-pass filter on the torque transducer signal and the inertia of the free turbine, since it provides a degree of filtering of the measured torque. When there is not enough filtering to smooth out any torque oscillations on the torque measurement, the system can become unstable. Furthermore, inertia coupling considerations have a significant effect on the transient speed response of the engine. A model-based analysis of the engine emulation system reveals that when the inertia of the motor is much larger than the engine, the speed response of the open-loop system is faster than the closed-loop system (emulation mode). Experimental results validate the model-based analysis of the aeroderivative engine emulation system for variations in the free turbine inertia of a real-time engine model, and cutoff frequency of the load torque low-pass filter.

CHAPTER 9: CONCLUSION AND FUTURE WORK

9.1 Conclusion

The first main contribution of this dissertation is the definition of a model-based control method for emulating an aeroderivative twin-shaft gas turbine engine that is part of a turbogenerator system during steady-state and transient conditions. The method involves the use of a vector controlled AC motor drive, which tracks the speed of an engine model as it drives an electric generator supplying power to steady-state and dynamic loads. The load torque is fed back to the engine model so that it calculates the speed reference as if it was really connected to the generator. One of the main challenges in emulating an aeroderivative twin-shaft engine using an electric motor drive is the fact that the engine is likely to have a high power density along with high power-to-weight ratio, which translates into very low inertia relative to a motor of the same power rating. Therefore, when emulating an aeroderivative engine by using an electric motor drive, power and accuracy limitations, as well as stability issues can arise.

A HFAC simulation system model and a benchtop-scale HIL experiment provide initial verification of the aeroderivative engine emulation model-based control method. A linear model-based analysis of the benchtop-scale aeroderivative engine emulation system reveals that the bandwidth of the emulating motor speed control loop is limited by the inertia of the motor, and that the feedback controller can be tuned according to the inertia of the emulating motor. Therefore, the feedback controller can be designed to accommodate motors having different inertias. Experimental results obtained using the benchtop-scale aeroderivative engine emulation

system show that the accuracy of the aeroderivative engine emulation system depends on the inertia difference between the engine and emulating motor. The high inertia case (when the motor inertia is larger than that of the engine) requires a larger control effort during speed acceleration and deceleration than the low inertia case (when the motor inertia is smaller than that of the engine). The engine tracking performance in the high inertia case can be improved by increasing the controller bandwidth. However, increasing the controller bandwidth can affect system stability and force the system into saturation.

The second main contribution of this dissertation is the definition of a design procedure for developing an aeroderivative twin-shaft engine emulation system. A HIL simulation of a low-power aeroderivative engine emulation system is used to validate methods developed for this design procedure. This procedure takes into account torque, power, and stability limitations that need to be considered when designing an aeroderivative engine emulation system for a specific aeroderivative engine–generator system that is already available. The first step involves the selection of the appropriate AC electric motor and variable-speed drive for emulating an engine. Once the motor and drive are selected, the speed tracking controller and the load torque low-pass filter are designed. Next, analysis of stability and inertia loading effects of the engine emulation system is performed.

One major achievement is the definition of a method for selecting the appropriate AC electric motor and variable-speed drive to emulate an aeroderivative twin-shaft engine based on torque, power and inverter current criteria that take into account the difference in inertia between the motor and engine, and the size of the desired step loading that is to be tested on the generator. The mathematical criteria establish that the emulating motor drive peak torque and power, and maximum inverter drive line current demands increase when the inertia of the motor is larger

135

than the inertia of the free turbine. Experimental results show that if the emulating motor does not meet the peak torque requirement when emulating an engine, speed controller saturation occurs and the engine emulation system is no longer capable of tracking the speed performance of the free turbine.

Another important achievement is the development of a linear model-based analysis of an aeroderivative engine emulation system. This allows predicting the stability and inertia loading effects of the emulation system according to variation in parameters such as engine inertia, motor drive control design and load torque filter design. The selection of the low-pass filter on the torque measurement can affect the stability of the engine emulation, and the system can become unstable if there is not enough filtering to smooth out any torque oscillations on the torque measurement. The inertia of the free turbine plays an important role in the stability by providing a degree of filtering of the measured torque. System instability appears to be due, at least in part, to low frequency oscillations in the torque demand, which are understood to be due to low damping in the dynamometer drive train and aggressive speed control settings. The model-based analysis of the emulation system also reveals that inertia coupling considerations have a significant effect on the transient speed response of the engine. When the inertia of the motor is much larger than the engine, the speed response of the open-loop system (non-emulation mode) is faster than the closed-loop system (emulation mode).

9.2 Future Work

This dissertation considers the use of a linear aeroderivative twin-shaft gas turbine engine model for the emulation studies. This limits the types of transient studies that can be performed since the accuracy of the engine model determines the types of tests that can be evaluated in the engine emulation system. Therefore, it is recommended to address the design of a non-linear

real-time aeroderivative twin-shaft gas turbine engine model that can be used in a HIL simulation of the engine emulation system. This would allow testing the engine emulation during critical conditions in generator loading such as fault conditions that can cause engine surge. Two possible ways of implementing a non-linear engine model in real-time simulation are using non-linear system identification techniques such as neural networks or coding a non-linear engine model.

Furthermore, the development of an aeroderivative engine emulation system using a mega-watt HIL setup is recommended, since the ultimate application of this research is testing HFAC generation systems operating at the mega-watt power level.

REFERENCES

[1] "Next Generation Integrated Power Systems, NGIPS Master Plan," Naval Sea Systems Command, Washington, DC, 2007.

[2] R. M. Calfo, G. E. Poole, and J. E. Tessaro, "High Frequency AC Power System," *Naval Engineers Journal*, vol. 120, pp. 45–54, 2008.

[3] H. M. Kojabadi, Liuchen Chang, and T. Boutot, "Development of a novel wind turbine simulator for wind energy conversion systems using an inverter-controlled induction motor," *Energy Conversion, IEEE Transactions on DOI - 10.1109/TEC.2004.832070*, vol. 19, no. 3, pp. 547–552, 2004.

[4] L. Chang, R. Doraiswami, T. Boutot, and H. Kojabadi, "Development of a wind turbine simulator for wind energy conversion systems," presented at the Electrical and Computer Engineering, 2000 Canadian Conference on, 2000, vol. 1, pp. 550–554 vol.1.

[5] Seung-Ho SOng, Byoung-Chang Jeong, Hye-In Lee, Jeong-Jae Kim, Jeong-Hun Oh, and G. Venkataramanan, "Emulation of output characteristics of rotor blades using a hardware-in-loop wind turbine simulator," presented at the Applied Power Electronics Conference and Exposition, 2005. APEC 2005. Twentieth Annual IEEE, 2005, vol. 3, pp. 1791–1796 Vol. 3.

[6] B. Rabelo, W. Hofmann, and M. Gluck, "Emulation of the static and dynamic behaviour of a wind-turbine with a DC-machine drive," presented at the Power Electronics Specialists Conference, 2004. PESC 04. 2004 IEEE 35th Annual, 2004, vol. 3, pp. 2107–2112 Vol.3.

[7] M. Chinchilla, S. Arnaltes, and J. L. Rodriguez-Amenedo, "Laboratory set-up for wind turbine emulation," presented at the Industrial Technology, 2004. IEEE ICIT '04. 2004 IEEE International Conference on, 2004, vol. 1, pp. 553–557 Vol. 1.

[8]   F. A. Farret, R. Gules, and J. Marian, "Micro-turbine simulator based on speed and torque of a DC motor to drive actually loaded generators," presented at the Devices, Circuits and Systems, 1995. Proceedings of the 1995 First IEEE International Caracas Conference on, 1995, pp. 89–93.

[9]   Bing Gong and Dewei Xu, "Real time wind turbine simulator for wind energy conversion system," presented at the Power Electronics Specialists Conference, 2008. PESC 2008. IEEE, 2008, pp. 1110–1114.

[10] D. Dolan and P. W. Lehn, "Real-Time Wind Turbine Emulator Suitable for Power Quality and Dynamic Control Studies," Montreal, Canada, 2005, pp. 1–6.

[11] D. S. L. Dolan and P. W. Lehn, "Simulation model of wind turbine 3p torque oscillations due to wind shear and tower shadow," *Energy Conversion, IEEE Transactions on DOI - 10.1109/TEC.2006.874211*, vol. 21, no. 3, pp. 717–724, 2006.

[12] M. Monfared, H. Madadi Kojabadi, and H. Rastegar, "Static and dynamic wind turbine simulator using a converter controlled dc motor," *Renewable Energy*, vol. 33, no. 5, pp. 906–913, May 2008.

[13] B. T. Boulter, "Designing a Dynamometer Test Stand with an Emulated Gasoline/Diesel Engine Power Source: A White Paper," ApICS LLC, 13, 2000.

[14] Honeywell International, Inc., "AGT1500 Turbine Technology." May-2000.

[15] H. Kapeller, A. Haumer, C. Kral, and C. Grabner, "Investigation of the Operational Behavior of a Large Chipper Drive," in *Proceedings of the World Congress on Engineering 2009 Vol I WCE 2009*, London, U.K., 2009.

[16] K. U. Voigt, "A control scheme for a dynamical combustion engine test stand," in *Control 1991. Control '91., International Conference on*, vol. 2, pp. 938–943.

[17] M. Schmidt, "Model-based torque controller for dynamical engine test stands," in *American Control Conference, 1999. Proceedings of the 1999*, 1999, vol. 5, pp. 3245–3249.

[18] J. Zhang, X. Wang, and Z. Guan, "Research on power measurement and loading control system of Automobile Engine Test Stand," vol. 3, pp. 478–481.

[19] Z. H. Akpolat, G. M. Asher, and J. C. Clare, "Experimental dynamometer emulation of nonlinear mechanical loads," *Industry Applications, IEEE Transactions on DOI - 10.1109/28.806051*, vol. 35, no. 6, pp. 1367–1373, 1999.

[20] R. Todd and A. J. Forsyth, "HIL emulation of all-electric UAV power systems," presented at the Energy Conversion Congress and Exposition, 2009. ECCE 2009. IEEE, 2009, pp. 411–416.

[21] S. M. Camporeale, B. Fortunato, and M. Mastrovito, "A Modular Code for Real Time Dynamic Simulation of Gas Turbines in Simulink," *Journal of Engineering for Gas Turbines and Power*, vol. 128, no. 3, pp. 506–517, 2006.

[22] L. Bozzi, G. Crosa, and A. Trucco, "Simplified Simulation Block Diagram of Twin-Shaft Gas Turbines," 2003, pp. 519–526.

[23] S. K. Yee, J. V. Milanović, and F. M. Hughes, "Validated Models for Gas Turbines Based on Thermodynamic Relationships," *Power Systems, IEEE Transactions on DOI - 10.1109/TPWRS.2010.2046428*, vol. 26, no. 1, pp. 270–281, 2011.

[24] T. Lovett, A. Monti, E. Santi, and R. A. Dougal, "A multilanguage environment for interactive simulation and development controls for power electronics," presented at the Power Electronics Specialists Conference, 2001. PESC. 2001 IEEE 32nd Annual, 2001, vol. 3, pp. 1725–1729 vol. 3.

[25] W. Jiang, R. Fang, J. Khan, and R. Dougal, "Control Strategies for Start-Up and Part-Load Operation of Solid Oxide Fuel Cell/Gas Turbine Hybrid System," *Journal of Fuel Cell Science and Technology*, vol. 7, no. 1, p. 011016, 2010.

[26] J. Kurzke, "The GasTurb Program." [Online]. Available: http://www.gasturb.de/index.html. [Accessed: 30-Sep-2012].

[27] J.-Y. Park, J.-K. Lee, K.-Y. Oh, J.-S. Lee, and B.-J. Kim, "Design of Simulator for 3MW Wind Turbine and Its Condition Monitoring System," in *Proceedings of The International*

MultiConference of Engineers and Computer Scientists 2010, Hong Kong, 2010, pp. 930–933.

[28] C. Ginet, R. Joho, and M. Verrier, "The Turbogenerator - A Continuous Engineering Challenge," presented at the Power Tech, 2007, pp. 1055–1060.

[29] Saravanamutto, G. F. C. Rogers, H. Cohen, and P. V. Straznicky, *Gas Turbine Theory*, 6th ed. Pearson Prentice Hall, 2009.

[30] Soon Kiat Yee, J. V. Milanovic, and F. M. Hughes, "Overview and Comparative Analysis of Gas Turbine Models for System Stability Studies," *Power Systems, IEEE Transactions on DOI - 10.1109/TPWRS.2007.907384*, vol. 23, no. 1, pp. 108–118, 2008.

[31] G. . Badeer, "GE Aeroderivative Gas Turbines - Design and Operating Features." [Online]. Available:
http://www.gepower.com/prod_serv/products/tech_docs/en/downloads/ger3695e.pdf.

[32] M. P. Boyce, *Gas Turbine Engineering Handbook, Second Edition*, 2nd ed. Gulf Professional Publishing, 2002.

[33] P. Centeno, I. Egido, C. Domingo, F. Fernandez, L. Rouco, and M. Gonzalez, "Review of gas turbine models for power system stability studies," presented at the 9th Spanish Portuguese Congress on Electrical Engineering, Marbella, Spain, 2005.

[34] L. N. Hannett, G. Jee, and B. Fardanesh, "A governor/turbine model for a twin-shaft combustion turbine," *IEEE Transactions on Power Systems*, vol. 10, no. 1, pp. 133 –140, Feb. 1995.

[35] T. Giampaolo, *Gas Turbine Handbook: Principles and Practice: Tony Giampaolo*, 3rd edition. Fairmont Press, 2006.

[36] B. K. Bose, *Modern Power Electronics and AC Drives*. Prentice Hall, 2001.

[37] D. W. Novotny and T. A. Lipo, *Vector Control and Dynamics of AC Drives*. Oxford University Press, 1996.

[38] R. Krishnan, *Electric Motor Drives: Modeling, Analysis, and Control*, United States ed. Prentice Hall, 2001.

[39] S. P. Das and A. K. Chattopadhyay, "Observer-based stator-flux-oriented vector control of cycloconverter-fed synchronous motor drive," *Industry Applications, IEEE Transactions on DOI - 10.1109/28.605736*, vol. 33, no. 4, pp. 943–955, 1997.

[40] F. Blaschke, "The Principle of Field Orientation as applied to the New TRANSVEKTOR Closed-Loop Control System for Rotating-Field Machines," *Siemens Review*, vol. 39, no. 5, pp. 217–220, May 1972.

[41] ABB, "Technical guide No. 1 Direct torque control - the world's most advanced AC drive technology." 2011.

[42] "Induction & Synchronous Motors," General Electric Motors.

[43] M. Matuonto and A. Monti, "High Performance Field Oriented Control for Cycloconverter-Fed Synchronous Machine: From Theory to Application," Sevilla, 1995, pp. 3.458–3.463.

[44] P. Vas, *Sensorless Vector and Direct Torque Control*. Oxford University Press, USA, 1998.

[45] Y. Liu, M. Steurer, and P. Ribeiro, "A novel approach to power quality assessment: real time hardware-in-the-loop test bed," *Power Delivery, IEEE Transactions on*, vol. 20, no. 2, pp. 1200 – 1201, Apr. 2005.

[46] W. Ren, M. Steurer, and T. L. Baldwin, "Improve the Stability and the Accuracy of Power Hardware-in-the-Loop Simulation by Selecting Appropriate Interface Algorithms," *Industry Applications, IEEE Transactions on*, vol. 44, no. 4, pp. 1286 – 1294.

[47] X. Wu, S. Lentijo, and A. Monti, "A novel interface for power-hardware-in-the-loop simulation," in *Computers in Power Electronics, 2004. Proceedings. 2004 IEEE Workshop on*, 2004, pp. 178 – 182.

[48] B. A. Correa, A. Smith, Wei Jiang, and R. A. Dougal, "Gas turbine emulator for testing of high-speed generators," presented at the IEEE SoutheastCon 2010 (SoutheastCon), Proceedings of the, 2010, pp. 226–229.

[49] P. M. Gerhart and R. J. Gross, *Fundamentals of fluid mechanics*. Addison-Wesley Pub. Co., 1985.

[50] M. J. Moran and H. N. Shapiro, *Fundamentals of Engineering Thermodynamics*. John Wiley & Sons, 2000.

[51] C. L. Phillips and H. T. Nagle, *Digital Control System Analysis and Design*, 3rd ed. Prentice Hall, 1994.

[52] "dSPACE - DS1104 R&D Controller Board." [Online]. Available: http://www.dspace.com/en/inc/home/products/hw/singbord/ds1104.cfm. [Accessed: 05-Oct-2012].

[53] W. I. Rowen, "Simplified mathematical representations of heavy duty gas turbines," *Transactions of the ASME Journal of Engineering for Power*, vol. 105, pp. 865–70, 1983.

[54] C. Szabo, M. Imecs, and I. I. Incze, "Vector control of the synchronous motor operating at unity power factor," in *Optimization of Electrical and Electronic Equipment, 2008. OPTIM 2008. 11th International Conference on*, 2008, pp. 15–20.

[55] "US Digital E3 Optical Kit Encoder." [Online]. Available: http://www.usdigital.com/products/encoders/incremental/rotary/kit/E3. [Accessed: 05-Oct-2012].

[56] "Center for Advanced Power Systems (CAPS)." [Online]. Available: http://www.caps.fsu.edu/. [Accessed: 10-Oct-2012].

[57] "Real Time Power System Simulation | RTDS Technologies." [Online]. Available: http://www.rtds.com/index/index.html. [Accessed: 10-Oct-2012].

[58] Alstom, "Alstom MV3000 (Alspa) technical guide." .

[59] "Dimensioning of a drive system." Fact File - Technical notes ABB, 2007.

[60] F. Roos, H. Johansson, and J. Wikander, "Optimal selection of motor and gearhead in mechatronic applications," *Mechatronics*, vol. 16, no. 1, pp. 63–72, Feb. 2006.

[61] P. Kundur, *Power System Stability and Control*. McGraw-Hill Professional, 1994.

[62] R. F. Schiferl and C. M. Ong, "Six Phase Synchronous Machine with AC and DC Stator Connections, Part I: Equivalent Circuit Representation and Steady-State Analysis," *IEEE Transactions on Power Apparatus and Systems*, vol. PAS-102, no. 8, pp. 2685–2693, Aug. 1983.

Appendix A: SYNCHRONOUS MACHINE MATHEMATICAL MODEL

The round rotor synchronous motor model described is based on [61]. It includes one damper winding on the *d* axis and two damper windings on the *q* axis. The voltage equations are given in Equation A-1.

$$v_q = R_s i_{qs} + \omega \lambda_{ds} + p \lambda_{qs}$$

$$v_d = R_s i_{ds} - \omega \lambda_{qs} + p \lambda_{ds}$$

$$v_f = R_f i_f + p \lambda_{fr}$$

$$0 = R_{k1q} i_{k1q} + p \lambda_{k1q}$$

$$0 = R_{k2q} i_{k2q} + p \lambda_{k2q}$$

$$0 = R_{kd} i_{kd} + p \lambda_{kd}$$

Equation A-1

,where

v_q and v_d are the stator voltages in the *q* and *d* axis, respectively,

i_{qs} and i_{ds} are the stator currents in the *q* and *d* axis, respectively,

v_f and i_f are the field voltage and current, respectively,

i_{k1q} and i_{k2q} are the damper winding currents in the q_1 and q_2 axis, respectively,

i_{kd} is the damper winding current in the *d* axis,

λ_{qs} and λ_{ds} are the stator flux linkages in the q and d axis, respectively,

λ_{k1q} and λ_{k2q} are the damper winding flux linkages in the q_1 and q_2 axis, respectively,

λ_{kd} is the damper winding flux linkage in the d axis,

λ_{fr} is the field flux linkage,

R_s is the stator resistance,

R_f is the field resistance,

R_{k1q} and R_{k2q} are the damper winding resistances in the q_1 and q_2 axis, respectively, and

R_{kd} is the damper winding resistance in the d axis.

Equation A-2 describes the synchronous machine model flux linkage equations.

$$\lambda_{qs} = L_{ls} i_{qs} + L_{mq} (i_{qs} + i_{k1q} + i_{k2q})$$

$$\lambda_{ds} = L_{ls} i_{ds} + L_{md} (i_{ds} + i_{kd} + i_{f})$$

$$\lambda_{k1q} = L_{lk1q} i_{k1q} + L_{mq} (i_{k1q} + i_{qs} + i_{k2q})$$

$$\lambda_{k2q} = L_{lk2q} i_{k2q} + L_{mq} (i_{k2q} + i_{qs} + i_{k1q})$$

$$\lambda_{kd} = L_{lkd} i_{kd} + L_{md} (i_{kd} + i_{ds} + i_{f})$$

$$\lambda_{fr} = L_{lf} i_{f} + L_{md} (i_{f} + i_{kd} + i_{ds})$$

Equation A-2

, where

L_{ls} is the stator leakage inductance,

L_{mq} and L_{md} are the mutual inductances in the q and d axis, respectively,

L_{lk1q} and L_{lk2q} are the damper winding leakage inductances in the q_1 and q_2 axis, respectively,

L_{lkd} is the damper winding leakage inductance in the d axis, and

L_{lf} is the field leakage inductance.

The machine electromagnetic torque is given by Equation A-3.

$$T_e = \lambda_{ds} i_{qs} - \lambda_{qs} i_{ds}$$

The motor rotor dynamics is described by Equation A-4.

$$T_e - T_l = J \frac{2}{P} \frac{d\omega_r}{dt} + B\omega_r$$

, where T_l is the load torque, J is the machine inertia, B is the machine damping coefficient, P is the number of poles in the machine and ω_r is the rotor speed.

Appendix B: HFAC SIX-PHASE SYNCHRONOUS GENERATOR MODEL AND EXCITATION CONTROLLER

B.1 Six-Phase Synchronous Generator Model

The model of a six-phase synchronous machine is developed following the specifications of an actual HFAC synchronous generator. The model developed is based on [62]. The six-phase synchronous machine is described mathematically by dividing the six stator phases into two three-phase sets displaced by an angle ε, and each set is labeled as *abc* and *xyz*. The effect of two damper windings is considered in the model. Figure B.1 shows a schematic representation of the two stator windings, field winding and damper windings.
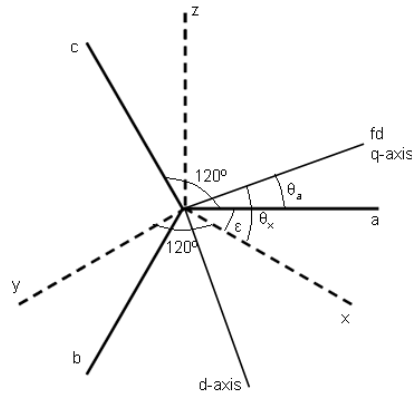

Figure B.1: Phasor representation of the two stator windings, field winding and damper windings of the six-phase generator

Phase *a* voltage is defined so that it is displaced by an angle of *ε = 60°* from phase *x* and has 0° phase reference when field current flows into the field plus terminal. Phases *abc* are

displaced by 120° as well as phases *xyz*. The six-phase synchronous machine voltage equations are defined in Equation B-1 in the rotor reference frame and using generator convention.

$$v_{q1}^r = -r_s i_{q1}^r + \omega_r \lambda_{d1}^r + p\lambda_{q1}^r$$

$$v_{d1}^r = -r_s i_{d1}^r - \omega_r \lambda_{q1}^r + p\lambda_{d1}^r$$

$$v_{q2}^r = -r_s i_{q2}^r + \omega_r \lambda_{d2}^r + p\lambda_{q2}^r$$

$$v_{d2}^r = -r_s i_{d2}^r - \omega_r \lambda_{q2}^r + p\lambda_{d2}^r$$

$$v_{Kq} = r_{Kq} i_{Kq} + p\lambda_{Kq}$$

$$v_{Kd} = r_{Kd} i_{Kd} + p\lambda_{Kd}$$

$$v_{fr} = r_{fr} i_{fr} + p\lambda_{fr} \qquad\qquad \text{Equation B-1}$$

, where

v_{q1}^r and v_{d1}^r are the stator voltages of the *abc* winding in the *q* and *d* axis, respectively,

v_{q2}^r and v_{d2}^r are the stator voltages of the *xyz* winding in the *q* and *d* axis, respectively,

v_{Kq} and v_{Kd} are damper winding voltages in the *q* and *d* axis, respectively,

v_{fr} is the machine field voltage,

i_{q1}^r and i_{d1}^r are the stator currents of the *abc* winding in the *q* and *d* axis, respectively,

i_{q2}^r and i_{d2}^r are the stator currents of the *xyz* winding in the *q* and *d* axis, respectively,

i_{Kq} and i_{Kd} are the damper winding currents in the *q* and *d* axis, respectively,

i_{fr} is the machine field current,

λ_{q1}^r and λ_{d1}^r are the stator flux linkages of the *abc* winding in the *q* and *d* axis, respectively,

λ^r_{q2} and λ^r_{d2} are the stator flux linkages of the *xyz* winding in the *q* and *d* axis, respectively

λ_{Kq} and λ_{Kd} are the damper winding flux linkages in the *q* and *d* axis, respectively,

λ_{fr} is the field flux linkage,

r_s is the stator resistance,

r_{Kq}, r_{Kd} are the damper resistances in the *q* and *d* axis, respectively,

r_{fr} is the field resistance.

Equation B-2 describes the six-phase synchronous generator model flux terms.

$$\lambda^r_{q1} = -L_{l1}i^r_{q1} - L_{lm}(i^r_{q1} + i^r_{q2}) + L_{ldq}i^r_{d2} + L_{mq}(-i^r_{q1} - i^r_{q2} + i_{Kq})$$

$$\lambda^r_{d1} = -L_{l1}i^r_{d1} - L_{lm}(i^r_{d1} + i^r_{d2}) - L_{ldq}i^r_{q2} + L_{md}(-i^r_{d1} - i^r_{d2} + i_{Kd} + i_{fr})$$

$$\lambda^r_{q2} = -L_{l2}i^r_{q2} - L_{lm}(i^r_{q1} + i^r_{q2}) + L_{ldq}i^r_{d1} + L_{mq}(-i^r_{q1} - i^r_{q2} + i_{Kq})$$

$$\lambda^r_{d2} = -L_{l2}i^r_{d2} - L_{lm}(i^r_{d1} + i^r_{d2}) + L_{ldq}i^r_{q1} + L_{md}(-i^r_{d1} - i^r_{d2} + i_{Kd} + i_{fr})$$

$$\lambda_{Kq} = L_{lKq}i_{Kq} + L_{mq}(-i^r_{q1} - i^r_{q2} + i_{Kq})$$

$$\lambda_{Kd} = L_{lKd}i_{Kd} + L_{md}(-i^r_{d1} - i^r_{d2} + i_{Kd} + i_{fr})$$

$$\lambda_{fr} = L_{lfr}i_{fr} + L_{md}(-i^r_{d1} - i^r_{d2} + i_{Kd} + i_{fr}) \qquad \text{Equation B-2}$$

, where

L_{l1} and L_{l2} are the leakage inductances of the *abc* and *xyz* windings, respectively,

L_{mq} and L_{md} are the mutual inductances in the *q* and *d* axis, respectively,

L_{lm} is the mutual leakage inductance,

L_{ldq} is the mutual leakage coupling inductance between stator windings,

L_{lKq} and L_{lKd} are the leakage inductances of the damper windings in the q and d axis, respectively,

L_{lfr} is the field leakage inductance

The generator electromagnetic torque is given by Equation B-3.

$$T_e = i_{q1}^r \lambda_{d1}^r + i_{q2}^r \lambda_{d2}^r - i_{d1}^r \lambda_{q1}^r - i_{d2}^r \lambda_{q2}^r \qquad \text{Equation B-3}$$

The generator rotor dynamics is described by Equation B-4.

$$T_m = J \frac{2}{P} \frac{d\omega_r}{dt} + T_e \qquad \text{Equation B-4}$$

, where T_m is the prime mover mechanical torque, J is the generator inertia, P is the number of poles in the machine and ω_r is the rotor speed.

The specifications of the HFAC generator are given in Table B.1.

Table B.1: HFAC generator specifications

Rated Power Level	14 MW
Speed	7000 rpm
Poles	4
Number of Phases	6
AC Output Voltage/Frequency	6.6 kVAC@233 Hz
Mechanical shaft inertia	71.8194 kg·m^2
Stator resistance	0.01997 Ω/phase
Synchronous reactance (at line frequency)	1.37 pu
Rotor resistance	0.01256 Ω
Rotor inductance	X_d=1.37 pu X_q=1.31 pu
Stator coupling inductances	2.733 pu
Rotor damper windings mutual inductances (L_{md}, L_{mq})	1.01 pu
Field inductance	2.9 pu

B.2 HFAC Generator Field Controller Design

The excitation controller of the six-phase synchronous generator is based on a simple PI controller. The excitation control loop shown in Figure B.2.
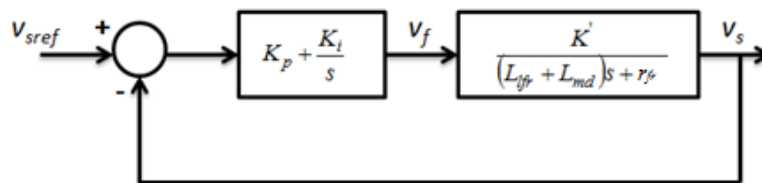

Figure B.2: Excitation control loop

152

Adequate values for K_p and K_i are obtained using the frequency tuning technique explained in Chapter 4. The value of K_p is 0.00022 and K_i is 0.00976. The output voltage, v_s, of the generator is calculated as,

$$v_s = \sqrt{v_{d1}^2 + v_{q1}^2}$$

Equation B-5

The reference output voltage, v_{sref}, is set to the peak of the rated line voltage,

$$v_{sref} = \sqrt{\frac{2}{3}} 6.6kV = 5388.9V$$

Equation B-6

Assuming that the output voltage is approximately equal to the emf during steady state, the plant transfer function relating the output v_s and input field voltage, v_f, can be established as shown in Equation B-7.

$$v_f = \left(\left(L_{lfr} + L_{md}\right)s + r_{fr}\right)i_f$$

$$v_s \approx e = K\omega i_f = K'i_f$$

$$\frac{v_s}{v_f} = \frac{K'}{(L_{lfr} + L_{md})s + r_{fr}}$$

Equation B-7

Appendix C: PARAMETER IDENTIFICATION FOR BENCHTOP-SCALE HIL EXPERIMENT

In order to design the speed controller of the synchronous motor it is necessary to estimate the mechanical parameters, inertia, J_M, and damping coefficient, B_M, and the torque constant, K_{tM}, of the motor. The electrical parameters, armature inductance, L_s, and armature resistance, R_s, are also required in order to design the current control loops. In the case of the DC motor, it is necessary to determine its inertia, J_{Gen}, and damping coefficient, B_{Gen}. Additionally, in order to estimate the torque load of the DC generator that is fed back to the engine model it is essential to determine the torque constant, K_t, of the generator. Furthermore, it is also necessary to determine the inertia and damping coefficient of the inertial load. The experiments performed to find these parameters are presented in the following sections.

C.1 Parameter Identification of Synchronous Machine

C.1.1 Inertia and Damping Coefficient

The procedure for estimating the inertia and damping coefficient of the synchronous machine is realized by tying a weight with known mass to the rotor of the synchronous machine. The weight is released so that the synchronous machine rotor starts spinning until the weight hits the ground. Speed vs Time data is recorded during the release of the weight until it hits the ground as shown in Figure C.1(blue line).

In this experiment, the mechanical torque of the synchronous machine can be calculated by using Equation C-1. The mechanical torque is equal to the mass of the weight, $m = 1\ kg$, times gravity, g, times the rotor radius, $r = 0.0084\ m$.

$$T_l = mgr$$

The machine rotor dynamics equation is defined in Equation C-2, and the solution this first order equation is expressed in Equation C-3 (in this experiment $T_e=0$). The speed of the machine is calculated by using Equation C-3, and is plotted in Figure C.1 (green line) by using a curve fitting procedure that yields the estimated values $J_M=0.0094\ kg \cdot m^2$ and $B_M=0.0005\ N \cdot s/m$.

$$T_l - T_e = J_M \frac{d\omega}{dt} + B_M \omega$$

$$\omega(t) = \frac{T_l}{B_M} \left(1 - e^{-(\frac{B_M}{J_M})t} \right)$$

C.1.2 Torque Constant

The torque constant of the synchronous machine, K_{tM}, is estimated assuming it is equal to the emf constant, K_{eM}, while the synchronous machine operates in generation mode. The emf constant is calculated by measuring the open-circuit voltage output of the synchronous machine while varying the speed. The field of the generator is kept constant at 32.3 V. Figure C.2 shows the line voltage plotted against the machine mechanical speed. The slope of this line gives the value of K_{eM}, which in this case is 0.26.
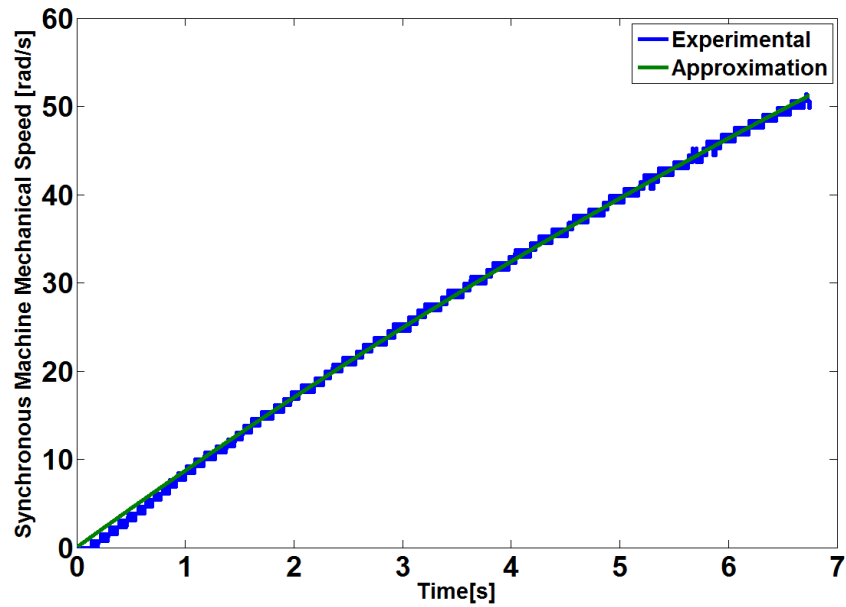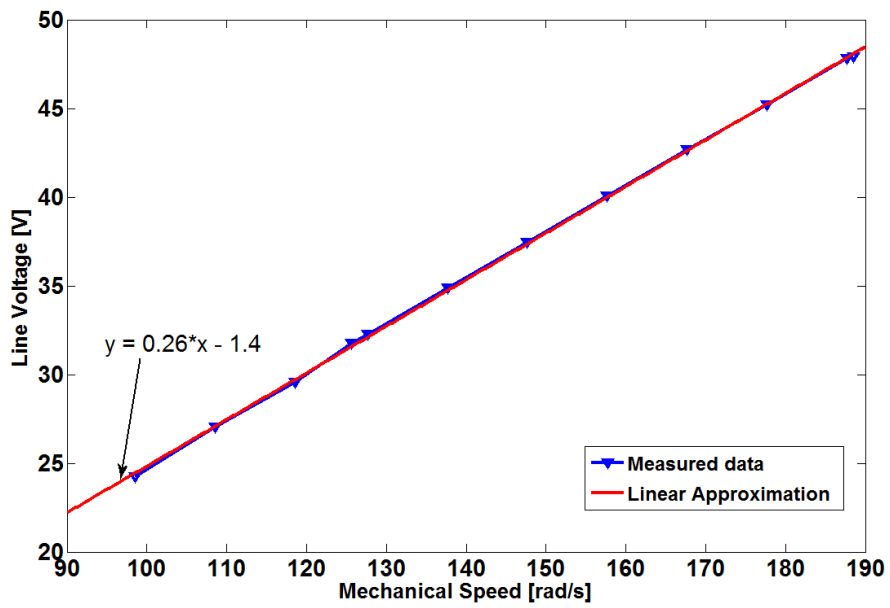
Figure C.1: Synchronous machine Speed vs Time

Figure C.2: Synchronous machine Line Voltage vs Mechanical Speed

C.1.3 Armature Inductance and Resistance

In order to estimate the armature inductance, L_s, of the synchronous machine open and short-circuit tests are performed as shown in Figure C.3. The synchronous reactance, X_s, is obtained from Equation C-4 as the ratio between the open-circuit rated line voltage and the short-circuit current at the same field current. This is indicated in Figure C.3. The armature inductance can be calculated from Equation C-5.

$$X_s = \frac{V_{aOC}}{I_{aSC}} = 149.5\Omega$$

<div align="right">**Equation C-4**</div>

$$L_s = \frac{X_s}{2\pi f_{rated}} = 396.5mH$$

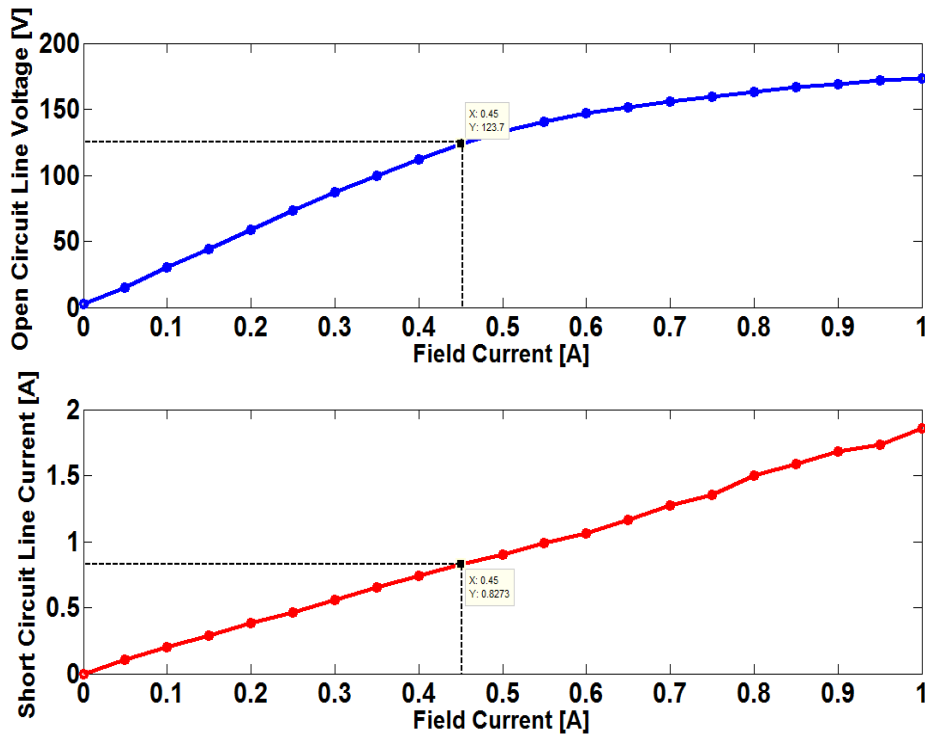<div align="right">**Equation C-5**</div>

Figure C.3: Synchronous machine open and short-circuit tests

The armature resistance, R_a, is estimated by measuring the DC resistance between phases *a* and *b* and dividing by two as indicated in Equation C-6. The AC resistance is assumed to be equal to the DC resistance.

$$R_s^{ac} = R_s^{dc} = \frac{R_s^{measured}(=9.3\Omega)}{2} = 4.65\Omega$$

Equation C-6

C.2 Parameter Identification of DC Machine

C.2.1 Inertia and Damping Coefficient

The inertia and damping coefficients of the DC machine are estimated using the procedure described in Section C.1.1. The plot of Speed vs Time is shown in Figure C.4. The curve fitting procedure yields the estimated values $J_{Gen}=0.0073 \ kg \cdot m^2$ and $B_{Gen}=0.0015 \ N \cdot s/m$.
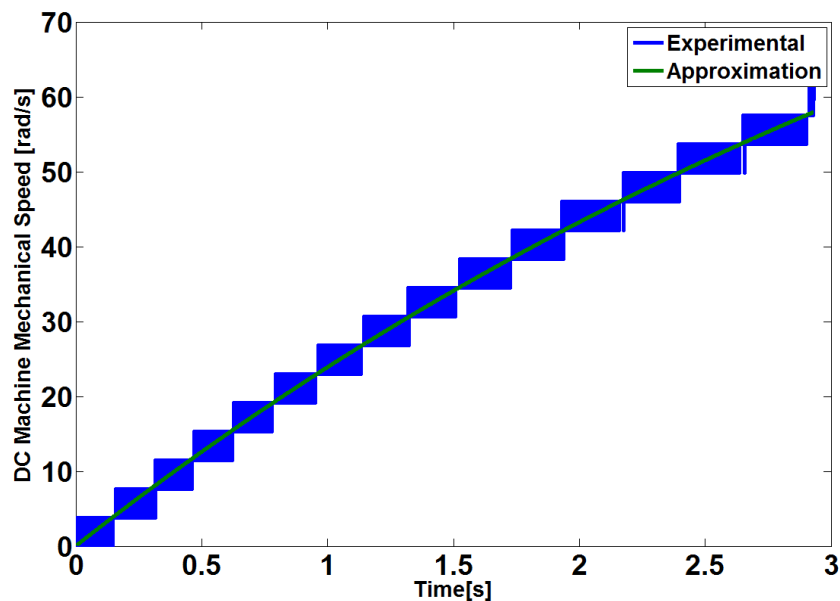

Figure C.4: DC machine Speed vs Time

158

C.2.2 Torque Constant

The torque constant of the DC machine, K_t, can be calculated from the datasheet rated values. In Equation C-7, the rated DC machine torque is calculated, and then in Equation C-8 K_t is derived using the rated value of the DC machine armature current.

$$T_e = \frac{P = 250W}{\omega_m = 188.5 rad/s} = 1.3263 N \cdot m \qquad \text{Equation C-7}$$

$$K_t = \frac{T_e}{I_a = 2A} = 0.6632 \qquad \text{Equation C-8}$$

These results are confirmed by taking data from the armature voltage and current at different speeds. In Figure C.5, the ratio E_a/I_a is plotted against ω_a/I_a during steady-state operation, in order to estimate K_t (the armature resistance is neglected).
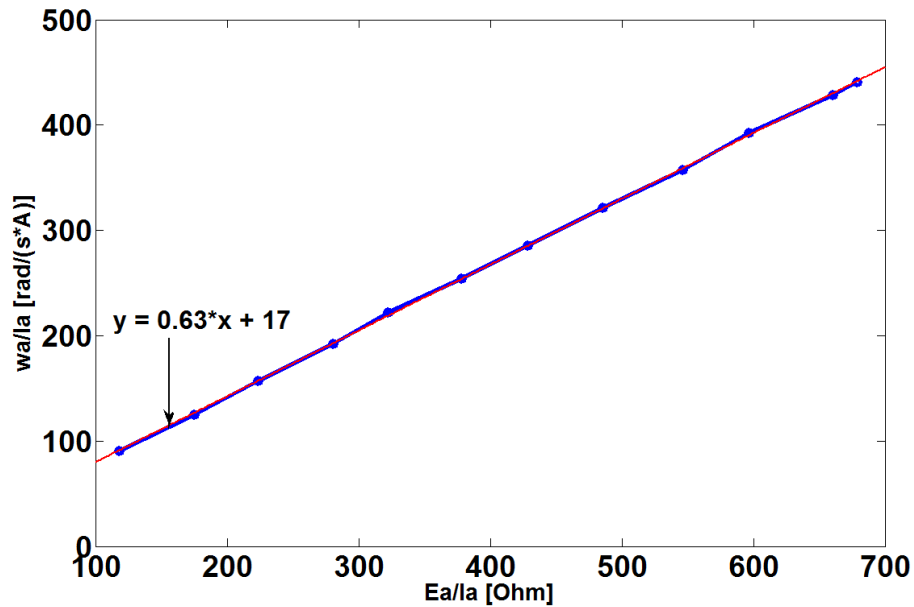

Figure C.5: DC machine E_a/I_a vs ω_a/I_a

C.3 Inertia and Damping Coefficient of Inertial Load

The inertia and damping coefficient of the shaft of the inertial load, and the inertia of the disks is estimated. The inertial load shaft is estimated using the procedure described in Section C.1.1 while attached to the DC machine. The inertia of the DC machine is subtracted from the total inertia of this system yielding the inertia of the inertial load shaft, $J_{ShaftIL}=0.0143\ kg{\cdot}m^2$. The damping coefficient of the inertial load shaft is estimated as $B_{ShaftIL}=0.0126\ N{\cdot}s/m$.

The inertia of each inertial disk is determined by using Equation C-9 which is the formula for calculating the inertia of a disk with hole in the center.

$$J_{disk} = \frac{1}{2} m_{disk}(R_{out}^2 + R_{in}^2)$$

Equation C-9

In this case, $m_{disk}=2.3768\ kg$, $R_{out}=0.119\ m$ and $R_{in}=0.0075\ m$, which yields $J_{disk}=0.0169\ kg{\cdot}m^2$.

Appendix D: SPECIFICATIONS OF HIL EXPERIMENTAL SETUP OF CHAPTER 6

Table D.1: Induction machine specifications

Base speed	880 rpm
Maximum speed	1800 rpm
Power	15 kW
Shaft torque	159 N·m
Inertia	$5.568 \cdot 10^{-1}$ kg·m^2
Rated voltage	460 V
Full load current	29 A
Power factor	0.8
Number of poles	8
Stator resistance	0.1819 Ω
Stator leakage inductance	3.421 mH
Magnetizing resistance	899 Ω
Magnetizing inductance	42 mH
Rotor resistance	0.2412 Ω
Rotor leakage inductance	3.575 mH

Table D.2: Specifications of drive operating in speed control mode

Transformer	45 kVA, 208 delta / 480Y, 5.18 % impedance
Power Electronics: Alstom MV3000 (Alspa)	480 V, 30 kW/37 kW, 52 A/65 A
Input filter	LCL 583 uH/8 uF/1749 uH, C is actually RC shunt branch connected in delta

Table D.3: Specifications of drive operating in torque control mode

Transformer	30 kVA, 208 delta / 480Y, 4.9 % impedance
Power Electronics: Alstom MV3000 (Alspa)	480 V, 30 kW/37 kW, 52 A/65 A
Input filter	LCL 583 uH/8 uF/1749 uH, C is actually RC shunt branch connected in delta